CANCER

# Targeting therapeutic nanoparticles to the glioblastoma resection margin by harnessing postoperative blood-brain barrier disruption

**Lorena F. Fernandes[1,2], Chariya Peeyatu[1,2], Lydia A. Thompson[1,2], Ben R. Dickie[2,3], Yu Siong Ho[1,2], Noelia Hernandez-Lobato[4,5], Neus Lozano[4], Kostas Kostarelos[1,2,4,6,7]*, Thomas Kisby[1,2]***



**Resection surgery is the first-line therapy for high-grade glioma performed in >70% of patients with glioblastoma, typically within days of suspected diagnosis. Current protocols for follow-on chemoradiotherapy have shown only modest efficacy in eliminating residual disease, leading to inevitable tumor recurrence. There remains a need for approaches to swiftly and effectively treat postoperative residual disease to prevent the rapid early progression of glioblastoma. Using syngeneic preclinical mouse models of glioblastoma resection, we identified spatially and temporally restricted windows of blood-brain barrier disruption localized to the resection margin during the immediate (0 hours) and early (48 to 72 hours) postoperative periods. Intravenous administration of fluorescently labeled, clinically used liposomal nanoparticles during these periods revealed selective accumulation at the postoperative resection margin, with minimal penetration into other regions of the brain with an intact blood-brain barrier. Immunohistological analysis confirmed nanoparticle extravasation in the margin parenchyma, largely interacting with microglial and macrophage populations closely associated with residual tumor cells. Exploiting this, we performed intravenous administration of doxorubicin-loaded liposomes coinciding with the peaks of postoperative blood-brain barrier disruption and demonstrated both enhanced chemotherapy delivery to the brain and, consequently, inhibition of tumor recurrence from a single administration across two glioblastoma models. Overall, this work identifies therapeutically exploitable windows of postoperative blood-brain barrier disruption and demonstrates that appropriately coordinated timing can enable clinically used liposomal nanomedicines to be repurposed for early postoperative therapy in aggressive brain tumors.**

## INTRODUCTION

Glioblastoma (GBM) is the most common, aggressive, and neurologically destructive brain cancer in adults (*1*). Maximal safe resection in the form of a gross total or supratotal resection is the first step in treatment; however, mainly because of their highly invasive phenotype, residual GBM cells will always remain after surgery (*2*, *3*). The current standard of care (SoC) aims to address this with a combination of radiotherapy and concurrent/adjuvant temozolomide (TMZ) chemotherapy (*4*). Despite this combinatorial approach, recurrence is largely inevitable, with current median survival remaining around 15 months after diagnosis and 5-year survival of less than 10% (*1*, *5*). In the current SoC, there is a period between resection surgery and the start of chemoradiotherapy of around 4 to 6 weeks where no antitumor therapy is given. During this period, which can potentially exceed the volumetric doubling time of the disease (*6*, *7*), the presence of early recurrent lesions in the form of rapid early progression (REP) has been identified in up to 50% of patients before the start of chemoradiation (*8*–*10*). Moreover, this REP has a significant negative impact on prognosis, highlighting the potential critical nature of this treatment gap in the outcomes of patients (*11*, *12*).

Because of the intracranial location of GBM, the blood-brain barrier (BBB) is considered a major limiting factor to the delivery and efficacy of systemically administered follow-on therapy. Although GBM tissue is largely characterized by a dysfunctional and leaky BBB, this is heterogeneous and is restricted to the bulk of the tumor, with peritumoral BBB remaining intact (*13*, *14*). The gadolinium (Gd) contrast–enhanced region in clinical magnetic resonance imaging (MRI), which is a classical imaging biomarker of BBB leakiness, is used to delineate the exact target for gross total resection surgery (*15*). The effect of surgery on the remaining BBB in regions that were originally Gd non–contrast-enhancing remains unclear. Clinical imaging guidelines and preclinical studies have indicated that resection induces dynamic, spatially heterogeneous alterations in BBB integrity; however, these are poorly defined and insufficiently characterized (*16*–*18*). By the time standard follow-on therapy is initiated (4 to 6 weeks after surgery), residual invasive tumor cells and cancer stem cells that escape resection are again protected by an intact BBB, which severely restricts the delivery of therapeutics to these populations. Consistent with this, postoperative tumor recurrence occurs in >80% of patients in the resection margin (1 to 2 cm from the cavity edge), highlighting this region as a critical and therapeutically underexploited target in GBM (*2*, *3*, *11*, *19*, *20*).

Various nanoparticle platforms have demonstrated the ability to enhance tumor drug delivery while improving the safety profile of cytotoxic chemotherapeutics (*21*, *22*). In the context of brain delivery, considerable effort has focused on engineering nanoparticles to actively traverse the intact BBB, including strategies that enhance

[1]Centre for Nanotechnology in Medicine, School of Biological Sciences, Faculty of Biology, Medicine, and Health, University of Manchester, Manchester M13 9PT, UK. [2]Geoffrey Jefferson Brain Research Centre, Manchester Academic Health Science Centre, Northern Care Alliance NHS Foundation Trust, University of Manchester, Manchester M13 9PT, UK. [3]Division of Informatics, Imaging, and Data Sciences, School of Health Sciences, University of Manchester, Manchester M13 9PT, UK. [4]Nanomedicine Lab, Catalan Institute of Nanoscience and Nanotechnology (ICN2), CSIC and BIST, Campus UAB, 08193 Barcelona, Spain. [5]Departament de Química, Facultat de Ciències, Universitat Autònoma de Barcelona, 08193 Barcelona, Spain. [6]Institute of Neuroscience, Universitat Autònoma de Barcelona, 08913 Barcelona, Spain. [7]Institució Catalana de Recerca i Estudis Avançats (ICREA), Pg. Lluís Companys 23, 08010 Barcelona, Spain.
*Corresponding author. Email: thomas.kisby@manchester.ac.uk (T.K.); kostas.kostarelos@manchester.ac.uk (K.K.)

interactions with endothelial transporters or exploit immune cell trafficking, with mixed success to date (*23*–*25*). Among clinically translated nanomedicines, liposomes, which are nanoscale vesicles composed of a phospholipid bilayer, have the longest history of regulatory approval, with multiple US Food and Drug Administration– and European Medicines Agency–approved formulations across diverse indications (*26*, *27*). The first clinically approved liposomal cancer therapeutic, liposomal doxorubicin (Doxil/Caelyx), remains widely used because of its favorable pharmacokinetics and improved cardiotoxicity compared with free doxorubicin. However, owing to their size (~80 to 120 nm) and surface properties, liposomal formulations such as Doxil do not readily cross an intact BBB, limiting their application in neuro-oncology. Liposomes have been shown to selectively accumulate in the brain after acute neurological injuries, including stroke (*28*, *29*) and traumatic brain injury (*30*, *31*), where neurovascular disruption and inflammation drive transient BBB dysfunction. In these settings, liposome accumulation is temporally dynamic, either transient or biphasic and spatially restricted to sites of injury. On the basis of these observations, we hypothesized that the surgical injury associated with bulk GBM resection similarly induces localized and time-dependent BBB disruption, enabling preferential translocation of circulating liposomes into the postoperative resection margin.

## RESULTS

### Selective accumulation of intravenously administered liposomes in the postoperative resection margin

Maximal safe resection surgery is the standard protocol applied to most (>70%) patients with suspected GBM (*2*, *32*). To better model this preclinically, we first established a murine model of GBM resection, whereby surgical removal of an intracranial cortical tumor was performed by craniotomy and tissue aspiration, mimicking the clinical procedure (fig. S1). Resection of an established GL261-luciferase tumor (7 days after inoculation) effectively eliminated the tumor bioluminescence signal detectable by in vivo optical imaging 2 and 7 days after resection (fig. S1A). Consistent with this, histological assessment demonstrated the absence of tumor bulk, with only sparse invasive residual disease remaining, consistent with the clinical scenario (fig. S1B). Longitudinal monitoring confirmed the eventual recurrence of GBM originating from the resection margin (fig. S1, C and D). This surgical approach provided a 2.3-fold increase in median survival (40 days) compared with that in unresected mice (17.5 days, $P = 0.007$), which is consistent with the relative fold-change survival benefit achieved from gross total resection in patients, providing an appropriate platform for investigation of postoperative events (*32*).

To determine whether surgical resection permits nanoparticle entry into the brain, we examined the postoperative distribution of polyethylene glycol–modified (PEGylated) liposomes using empty, with no encapsulated doxorubicin, DiI-labeled vesicles identical to the Doxil/Caelyx formulation {hydrogenated soy phosphatidylcholine (HSPC): cholesterol (Chol): 1,2-distearoyl-sn-glycero-3-phosphoethanolamine-N-[methoxy(polyethylene glycol)-2000] (DSPE-PEG2000)} (characterized in fig. S2). A single intravenous injection of empty DiI-liposomes was administered to the surgical resection mouse model either 15 min before surgical resection (−15 min) or at defined intervals after surgery (+15 min, 3 hours, 24 hours, 48 hours, 72 hours, and 7 days) (Fig. 1A). Postoperative injections were performed only after confirmation of complete hemostasis at the surgical site and wound closure. Animals were euthanized 24 hours after the administration of DiI-liposomes and perfused to remove any nanoparticles remaining in the circulation before DiI fluorescence in the brain and other organs was measured ex vivo. Selective accumulation of DiI-liposomes was observed at the resection margin in the operated hemisphere, with minimal signal detected in the contralateral, nonmanipulated hemisphere (Fig. 1B and fig. S3). Quantification of DiI fluorescence intensity in the brain indicated two phases of significant liposome accumulation, with an early peak when liposomes were administered around the time of resection surgery (−15 min, $P = 0.003$, or +15 min, $P = 0.005$) followed by an initial decrease (3 and 24 hours) and a delayed peak when liposomes were administered 48 to 72 hours after surgery ($P < 0.0001$) (Fig. 1C). This mirrors biphasic BBB permeability that has previously been described in other neurological injuries such as ischemic stroke, suggesting that tumor resection induces a comparable, injury-associated BBB response (*28*).

Histological analysis confirmed selective liposome accumulation at the resection margin, with the most uniform distribution observed at the two peak time points, 15 min and 48 to 72 hours after resection (Fig. 1D and fig. S4). At early time points (15 min to 72 hours), DiI-liposomes were predominantly and relatively uniformly localized around the resection margin. By day 7 after resection, this margin-specific localization was lost, with liposomes accumulating mainly in residual or recurrent tumor areas without extending beyond the tumor borders, a pattern similar to that seen in unresected animals (fig. S5). Consistent with these observations, the mean area of liposome distribution was significantly ($P = 0.018$) reduced by 58% when injected on day 7 compared with the maximal spread observed at 48 hours after resection (fig. S6).

### Selective resection margin accumulation is model and tumor independent

We confirmed this phenomenon in an alternative, more infiltrative, stem cell–based glioma model, using orthotopic implantation of murine glioma neurospheres (mGNSs) derived from a genetically engineered mouse ($NRAS^{G12V}$;shTP53-GFP;shATRX;luciferase) (fig. S7) (*33*, *34*). Bioluminescence imaging and histology verified successful resection of the bulk tumor, although deeply invasive residual cells remained (fig. S7, A to C). Consistent with observations in the GL261 tumor resection model, intravenous administration of DiI-liposomes 15 min or 48 hours after resection led to selective accumulation around the resection margin (fig. S7, D and E).

To further assess whether this margin accumulation depended on residual tumor and the compromised blood-tumor barrier, we validated this response in animals undergoing a cortical resection of a comparable volume of cortical brain tissue in the absence of any prior tumor implantation (Fig. 1, E and F). Intravenous DiI-liposomes administered 48 hours after resection showed significantly ($P < 0.001$) increased brain penetration and altered biodistribution compared with unoperated controls and did not differ significantly ($P = 0.64$) from mice with resected GL261 tumors (Fig. 1, E and F, and fig. S8).

These results indicate that surgical injury, rather than leaky tumor vasculature, is the primary driver of liposome accumulation at the resection margin. In a separate study cohort, we also assessed the impact of the auxiliary peri- and postoperative regimen of a clinically aligned dose of dexamethasone corticosteroids to further mimic typical care for patients with GBM (*35*, *36*). This did not significantly affect liposome accumulation, highlighting compatibility with the existing surgical SoC (fig. S9).

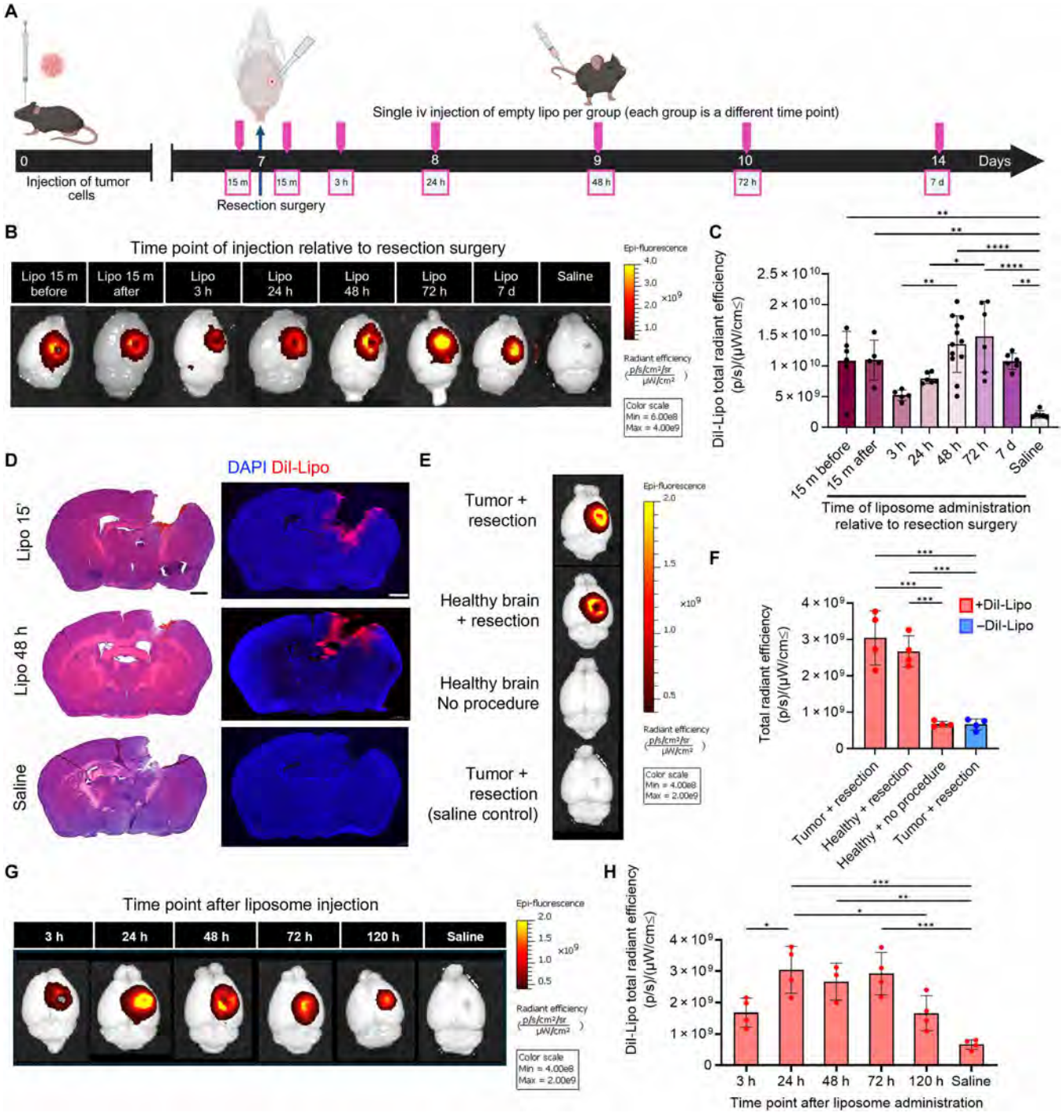


**Fig. 1. Biphasic and prolonged accumulation of intravenously administered liposomes in the brain after resection surgery.** (**A**) Schematic of the experimental design showing the timing of intravenous Dil-liposome administration before or after resection surgery. iv, intravenous. (**B**) Representative ex vivo fluorescence images of perfused brains acquired 24 hours after liposome injection. (**C**) Quantification of brain liposome fluorescence expressed as total radiant efficiency ($n = 6$ to 12 per group). Data are presented as means ± SD. *P* values were obtained using one-way ANOVA followed by Tukey's multiple comparisons test. (**D**) H&E staining and corresponding representative fluorescence microscopy images of brain sections collected 24 hours after intravenous Dil-liposome (Dil-Lipo) injection at the identified peak accumulation time points. Scale bars, 1000 μm. (**E**) Representative ex vivo fluorescence images of perfused brains acquired 24 hours after intravenous Dil-liposome injection (administered 48 hours after resection) in tumor-bearing and non–tumor-bearing naïve mice. (**F**) Quantification of brain liposome fluorescence expressed as total radiant efficiency ($n = 4$ per group). Data are presented as means ± SD. *P* values were obtained using one-way ANOVA followed by Tukey's multiple comparisons test. (**G**) Representative ex vivo fluorescence images of perfused brains collected 3, 24, 48, 72, or 120 hours after intravenous Dil-liposome injection (administered 48 hours after resection). (**H**) Quantification of brain liposome fluorescence expressed as total radiant efficiency ($n = 3$ or 4 per group). Data are presented as means ± SD. *P* values were obtained using one-way ANOVA followed by Tukey's multiple comparisons test; $^*P < 0.05$, $^{**}P < 0.01$, $^{***}P < 0.001$, and $^{****}P < 0.0001$. h, hours; m, minutes; d, days.

Last, we evaluated the tissue retention of DiI-liposomes after intravenous injection at 48 hours after resection. Liposomes accumulated over 24 hours and remained stably localized at the resection margin for at least 72 hours, with detectable levels persisting up to 120 hours (Fig. 1, G and H, and fig. S10). These findings reveal a prolonged window during which systemically administered liposomes selectively reside at the resection site, highlighting an exploitable period for targeted postoperative intervention in GBM.

### Spatial distribution and improved uptake of liposome nanoparticles into the peritumoral/margin areas

We analyzed the spatial distribution of DiI-liposomes in animals injected at the immediate (15 min) or early (48 hours) postresection windows of accumulation and compared this with the distribution in unresected controls (Fig. 2A). The resection cavity (RC) or tumor (T) was determined by 4′,6-diamidino-2-phenylindole (DAPI) staining, and the peritumoral/resection margin (P/M) region was designated as the 300 μm radiating from the cavity or tumor, scaling in humans to the region where >80% of GBM recurrence clinically occurs (Fig. 2B) (*3*, *37*). In unresected animals, DiI-liposomes primarily accumulated in the tumor core, with minimal signal in the peritumoral region, consistent with an intact BBB outside the tumor bulk (Fig. 2C) (*13*, *14*). In contrast, postresection administration resulted in robust DiI accumulation in the P/M region, demonstrating local BBB disruption at the resection margin. Quantification confirmed a significant increase ($P = 0.010$) in fluorescence intensity in the P/M region at 48 hours after resection compared with that in unresected controls (Fig. 2D). Furthermore, liposomes extended beyond the 300-μm margin into surrounding brain tissue, indicating the potential to reach more invasive residual tumor cells. These findings reveal that postoperative administration in defined windows can provide a meaningful shift in biodistribution that preferentially targets regions most relevant for tumor recurrence.

### Spatiotemporal dynamics of BBB disruption at the resection margin are detectable by clinically relevant neuroimaging

We next asked whether the patterns of BBB permeability observed with DiI-liposome optical imaging could be captured using dynamic contrast-enhanced MRI (DCE-MRI), the gold standard clinical method for assessing BBB integrity (*38*, *39*). Postoperative Gd contrast enhancement around the resection area has been reported in patients with GBM using standard anatomical (T2) MRI (*16*–*18*), but this has not been validated as BBB disruption with DCE-MRI. Here, mice were imaged 24 hours, 48 hours, and 8 days after resection of a GL261 tumor using both T2 and DCE-MRI (Fig. 3). Before surgery, DCE-MRI showed Gd contrast only in the tumor bulk, consistent with a compromised blood-tumor barrier but intact surrounding BBB (Fig. 3A), mirroring clinical observations in patients (*15*, *40*). After resection, signal enhancement was significantly increased ($P < 0.0001$) in the resection margin compared with the contralateral, nonsurgical hemisphere at 24 to 48 hours (Fig. 3, A and B). Enhancement compared with that in unresected controls was strongest immediately adjacent to the cavity at the earlier time points {0.158 μm, $P = 0.004$ at day 1, $P = 0.027$ at day 2, $P = 0.262$ [not significant (n.s.)] at day 8} and gradually decreased with distance (0.158 μm versus 0.482 μm, $P = 0.012$), extending several hundred micrometers into the surrounding tissue (Fig. 3C), closely mirroring the spatial pattern of liposome accumulation. By day 8, signal at the margin had largely returned to baseline, with no significant [0.158 μm, $P = 0.262$ (n.s.)] enhancement detectable (Fig. 3C). These findings provide preclinical validation of postoperative BBB dynamics and suggest that routinely available DCE-MRI could serve as a noninvasive predictor of nanoparticle access to the resection margin.

### Translocated liposomes interact primarily with margin-localized microglial/macrophage populations

To better characterize the interaction of DiI-liposomes with the local brain vasculature and BBB, we performed immunostaining of markers of blood vessels/endothelial cells (CD31) and transcytosis machinery [caveolin-1 (CAV1)] (Fig. 4A). We focused on the two postresection time points with maximal liposome accumulation (injected at 15 min and 48 hours). Analysis 24 hours after administration, after perfusion to remove circulating nanoparticles, revealed that ~40% of DiI signal colocalized with $CD31^+$ cells, whereas the majority was outside the vasculature, confirming extravasation into the brain parenchyma (Fig. 4, A and B). A substantial fraction of DiI in $CD31^+$ areas colocalized with CAV1, in line with previous reports implicating CAV1-dependent transcytosis in nanoparticle BBB translocation during states of brain tissue injury (Fig. 4, C and D) (*28*).

Having confirmed extravasation of DiI-liposomes, we next examined their interaction with cellular populations in the resection margin. Liposomes injected at the immediate (15 min) or early (48 hours) postresection time points showed minimal association with glial fibrillary acidic protein–positive ($GFAP^+$) astrocytes but were readily internalized by ionized calcium-binding adapter molecule 1–positive ($IBA1^+$) macrophages/microglia at both time points (fig. S11A). Internalization in macrophages/microglia was particularly pronounced ($P < 0.0001$) at the 48-hour injection time point, which may contribute to the enhanced retention of liposomes in the margin microenvironment during this period (fig. S11, A and B). To further explore interactions with residual tumor cells, we performed a similar analysis in the invasive mGNS model, in which glioma cells express green fluorescent protein (GFP; Fig. 4E). Minimal uptake of DiI-liposomes was observed in $GFP^+$ ($IBA1^-$) tumor cells at either injection time point, whereas $IBA1^+$ macrophages/microglia preferentially internalized liposomes (Fig. 4, E to G, and fig. S12). These findings align with previous reports showing that phagocytic cells are the primary mediators of nanoparticle internalization and tissue retention (*41*, *42*).

Quantitative validation using flow cytometry of mice injected intravenously with DiD-labeled liposomes at 15 min or 48 hours after resection confirmed these observations (Fig. 4H and fig. S13). $DiD^+$ cells were detectable in the resected hemisphere at both time points, with higher numbers at 48 hours (Fig. 4, H and I, and fig. S14). Analysis of $DiD^+$ populations revealed preferential association with $CD45^+$ leukocytes, particularly $CD45^+CD11b^+$ macrophages/microglia, both in percentage and absolute numbers (Fig. 4J and fig. S14). Although a significantly ($P < 0.001$) smaller fraction of $DiD^+$ cells were $CD45^-GFP^+$ tumor cells, a significant ($P < 0.001$) proportion of the total $CD45^-GFP^+$ population was $DiD^+$, especially at 48 hours, indicating limited but nonnegligible uptake by residual cancer cells (Fig. 4J and fig. S15, A to C).

### Selective liposome accumulation provides enhanced localized drug delivery to the postoperative resection margin

We next investigated whether the early postoperative translocation and accumulation of liposomes could improve therapeutic drug delivery. We used liposomes encapsulating doxorubicin, as in the clinically

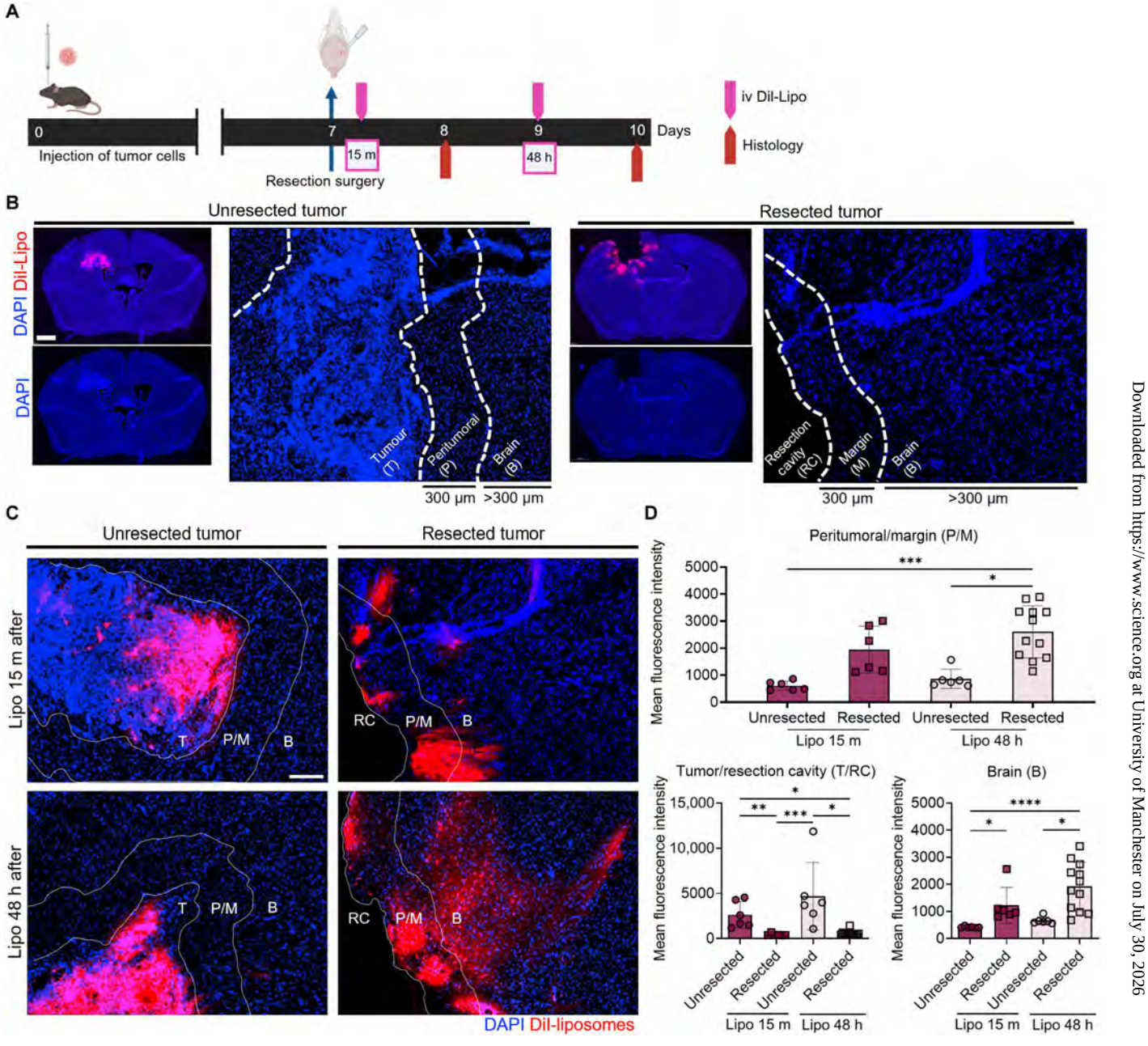


**Fig. 2. Spatial distribution of intravenously injected liposomes in the resection margin.** (**A**) Experimental schematic. Mice were injected intravenously (iv) with Dil-liposomes (Dil-Lipo) either 15 min or 48 hours after surgical resection of GL261 glioma or at equivalent time points in unresected GL261 tumor–bearing animals. Brains were perfused 24 hours after liposome injection. (**B**) Brain regions were delineated (shown with white dashed lines) across serial sections on the basis of DAPI intensity and morphology to define the tumor (T) region in unresected animals or the RC in resected animals. In both conditions, a 300-µm region extending radially from the tumor edge or cavity boundary was defined as the peritumoral (P) or resection margin (M), respectively. Regions beyond this distance were defined as normal brain (B). Scale bar, 1 mm. (**C**) Representative fluorescence images showing Dil-liposome distribution in the T/RC, P/M, and B regions 24 hours after intravenous injection at the indicated time points after resection (15 min or 48 hours) or equivalent time points in unresected animals. Scale bar, 200 µm. (**D**) Quantification of Dil-liposome fluorescence intensity (mean gray value) in the T/RC, P/M, and B regions ($n = 6$ to 12 mice per group). Data are presented as means ± SD, averaged from three fields per mouse. *P* values were obtained using Kruskal-Wallis test; $^{*}P < 0.05$, $^{**}P < 0.01$, $^{***}P < 0.001$, and $^{****}P < 0.0001$. m, minutes; h, hours.

approved Doxil/Caelyx formulation (fig. S16). Although doxorubicin is effective against GBM cell lines in vitro (*43*, *44*), its clinical efficacy is limited by poor BBB penetration and active efflux by endothelial transporters, preventing therapeutic concentrations in the brain (*45*–*47*). Doxorubicin-containing liposomes (DOX-Lipos) or an equivalent dose of free doxorubicin (5 mg/kg) were administered intravenously 48 hours after resection, with brains recovered 1 or 7 days later (Fig. 5A). Exploiting the autofluorescent properties of doxorubicin, confocal microscopy revealed distinct localization of doxorubicin in the resection margin in the DOX-Lipo–treated animals, which was largely undetectable in the free doxorubicin–treated group (Fig. 5B). Quantitative analysis confirmed significantly ($P = 0.022$) enhanced drug

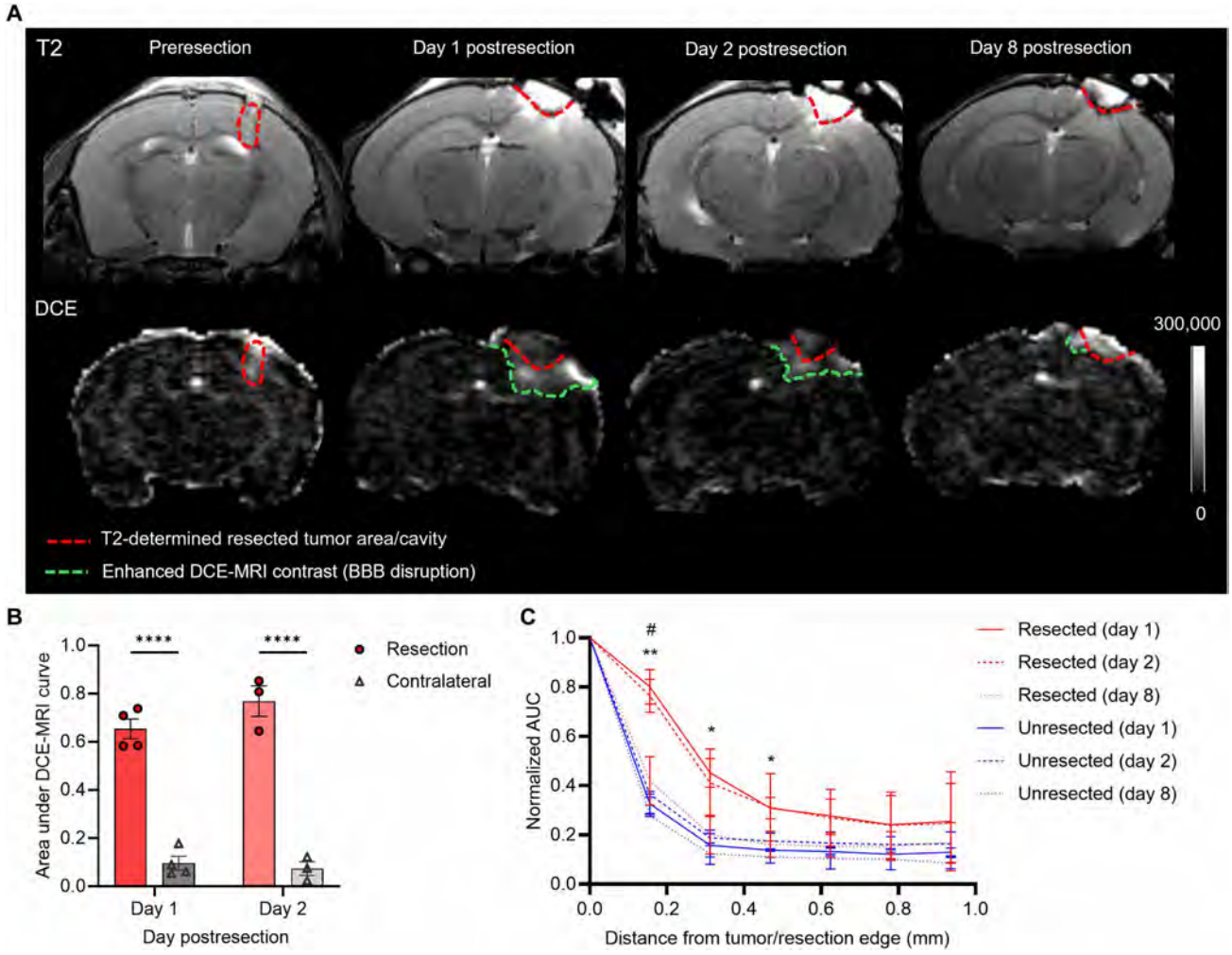


**Fig. 3. Direct in vivo DCE-MRI imaging of resection margin BBB integrity.** (**A**) Representative T2-weighted anatomical images and Gd DCE-MRI scans of mouse brains acquired before tumor resection (day −1) and at 24 hours, 48 hours, and 8 days after surgical resection of an intracranial GL261 tumor. The tumor or resection border is delineated by a red dashed line on the basis of T2-weighted imaging, whereas the green dashed line outlines regions of Gd contrast enhancement observed during the DCE sequence. (**B**) Quantification of contrast agent leakage, expressed as the area under the DCE-MRI enhancement curve (AUC) in the resection region and a size-matched region in the contralateral hemisphere. Data are presented as means ± SEM. Statistical analysis was performed using two-way ANOVA followed by Holm-Šidák multiple comparisons test. (**C**) Radial distributions of Gd leakage, shown as AUC values normalized to the total AUC in the tumor (preresection) or resection region (postresection) for each animal, plotted in 0.2-mm radial increments from the tumor edge or resection margin at each time point. Statistical analysis was performed with two-way ANOVA followed by Tukey's multiple comparisons test. Data are presented as means ± SEM; $*P < 0.05$, $**P < 0.01$, $****P < 0.0001$, and $\#P < 0.05$ (resected day 2 relative to unresected day 2 control).

delivery and retention in the resection margin when administered via liposomes.

To confirm the extravascular distribution of doxorubicin, we assessed colocalization with cell types in the resection margin. As with empty liposomes, DOX-Lipos showed minimal colocalization in $CD31^+$ endothelial cells and instead accumulated in the nuclei of $IBA1^+$ microglia/macrophages (Fig. 5C). Low levels of doxorubicin were also detected in residual $GFP^+$ cancer cells (fig. S17), but it was largely absent from $NeuN^+$ neurons and $GFAP^+$ astrocytes (fig. S18). We then evaluated the impact on residual tumor tissue histologically at 24 hours and 7 days after injection. DOX-Lipos administered 48 hours after GL261 resection significantly ($P = 0.027$) reduced the expansion of histologically detectable residual disease compared with free doxorubicin, based on hematoxylin and eosin (H&E)–identified tumor volume (Fig. 5, D and E). Given the predominant uptake by $IBA1^+$ cells, we also examined this population and observed a modest reduction in these cells (numbers and intensity) 24 hours after DOX-Lipo treatment in both GL261 and mGNS resections, suggesting that effects on this population may contribute to the local therapeutic response (figs. S19 and S20).

Last, to determine long-term therapeutic efficacy, GL261 tumor–bearing mice were treated with DOX-Lipos or free doxorubicin 48 hours after resection. Free doxorubicin failed to significantly [$P = 0.186$ (n.s.)] delay recurrence compared to vehicle controls, whereas DOX-Lipos completely and significantly ($P = 0.001$ compared with vehicle and $P = 0.01$ compared with free doxorubicin) suppressed recurrence for up to 100 days in all treated animals (Fig. 5, F to H, and fig. S21). These results demonstrate that selective accumulation of liposomes in the

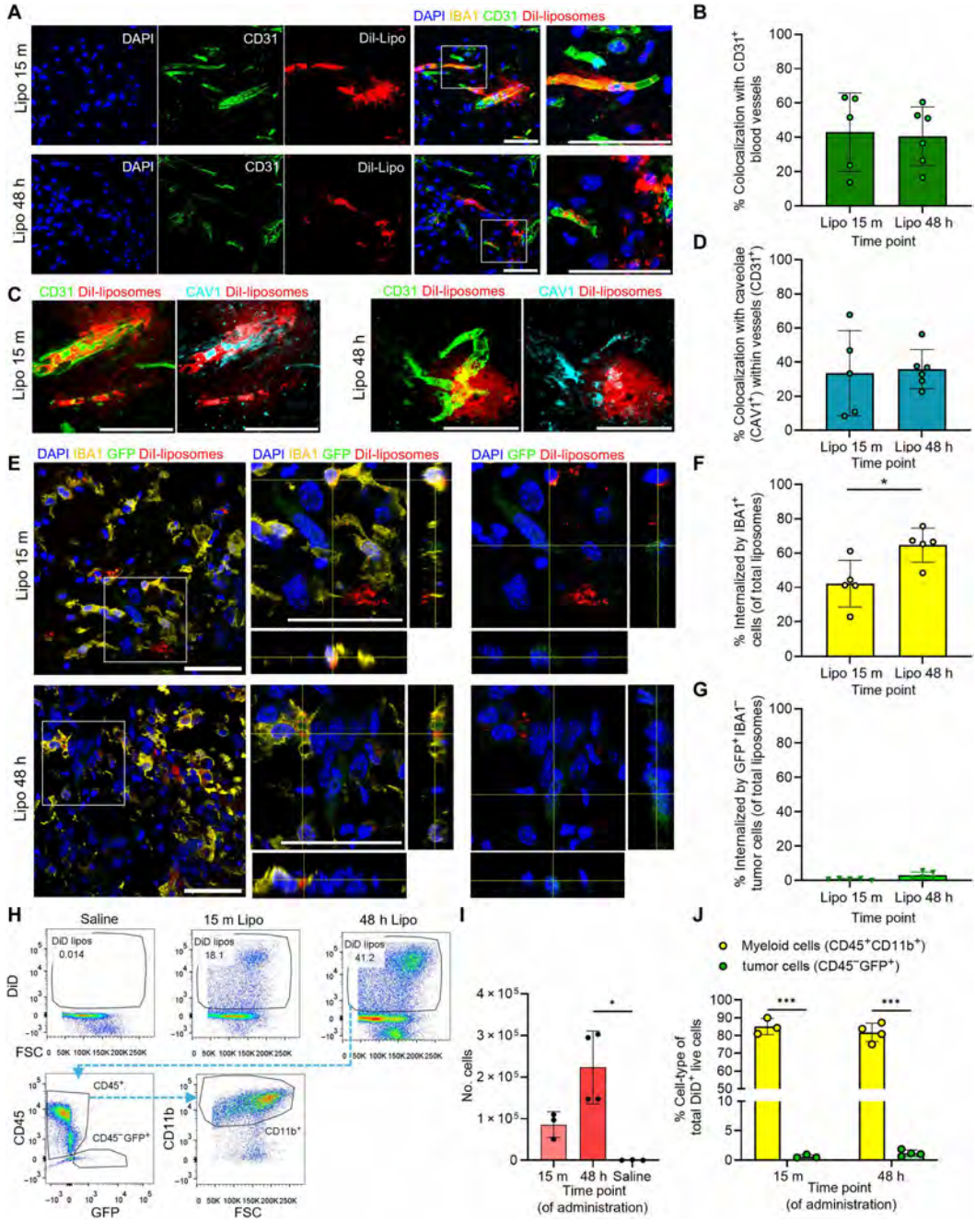


**Fig. 4. Extravasation and selective liposome internalization by resection margin macrophages/microglia.** (**A**) Representative confocal micrographs showing CD31-labeled endothelial cells and DiI-liposomes (DiI-Lipo) in mice injected intravenously 15 min or 48 hours after GL261 glioma resection. Brains were perfused and collected 24 hours after injection, revealing liposome extravasation beyond the vasculature. Scale bars, 50 μm. (**B**) Quantification of DiI-liposome signal area colocalized with CD31, expressed as a percentage of total DiI signal area (four fields of view per mouse; $n = 5$ or 6 mice). Data are presented as means ± SD. Statistical analysis was performed using Student's $t$ test. (**C**) Representative confocal micrographs showing CD31, CAV1, and DiI-liposomes in mice injected 15 min or 48 hours after resection and analyzed 24 hours later. Scale bars, 50 μm. (**D**) Quantification of CAV1-DiI colocalization, normalized to DiI signal in CD31-positive vessels (four fields of view per mouse; $n = 5$ or 6 mice). Data are presented as means ± SD. Student's $t$ test. (**E**) Representative confocal micrographs showing IBA1-positive microglia/macrophages, GFP-labeled tumor cells (mGNS), and DiI-liposomes in mice injected 15 min or 48 hours after tumor resection and analyzed 24 hours later. Scale bars, 50 μm. (**F**) Quantification of internalized DiI-liposomes in IBA1-positive cells, expressed as a percentage of total liposomes (four fields of view per mouse; $n = 5$ mice). Data are presented as means ± SD. $P$ values were determined using Student's $t$ test. (**G**) Quantification of internalized DiI-liposomes in GFP-positive, IBA1-negative tumor cells, expressed as a percentage of total liposomes (four fields of view per mouse; $n = 5$ mice). Data are presented as means ± SD. (**H**) Representative flow cytometry dot plots showing gating strategy for identification of DiD-positive live cells and corresponding DiD$^+$ cell types from the resected hemispheres of mice injected with DiD-labeled liposomes 15 min or 48 hours after tumor resection and analyzed 24 hours later. FSC, forward scatter. (**I**) Absolute number of DiD-positive cells isolated from the resected hemisphere at each time point compared with those of saline-injected controls ($n = 3$ or 4). Data are presented as means ± SD. $P$ values were determined by Kruskal-Wallis test. (**J**) Quantification of DiD-positive myeloid (CD45$^+$CD11b$^+$) or tumor (CD45$^-$GFP$^+$) cells expressed as a percentage of total DiD-positive live cells ($n = 3$ or 4). Data are presented as means ± SD. $P$ values were determined by two-way ANOVA followed by Tukey's multiple comparisons test; $^*P < 0.05$, $^{***}P < 0.001$, and not significant (n.s.). m, minutes; h, hours.

postoperative resection margin can be leveraged to achieve effective, localized chemotherapy and provides a postsurgical intervention strategy to suppress GBM recurrence. We also evaluated administration of DOX-Lipos in the immediate postoperative window (15 min after resection) and observed a comparable effect (fig. S22).

Immediate (15 min) or early (48 hours) postoperative administration of DOX-Lipos did not adversely affect animal health or postoperative recovery, as assessed by body weight and general behavior (fig. S23). To further evaluate the safety of this early postoperative strategy, we performed a longitudinal assessment of organ histopathology,

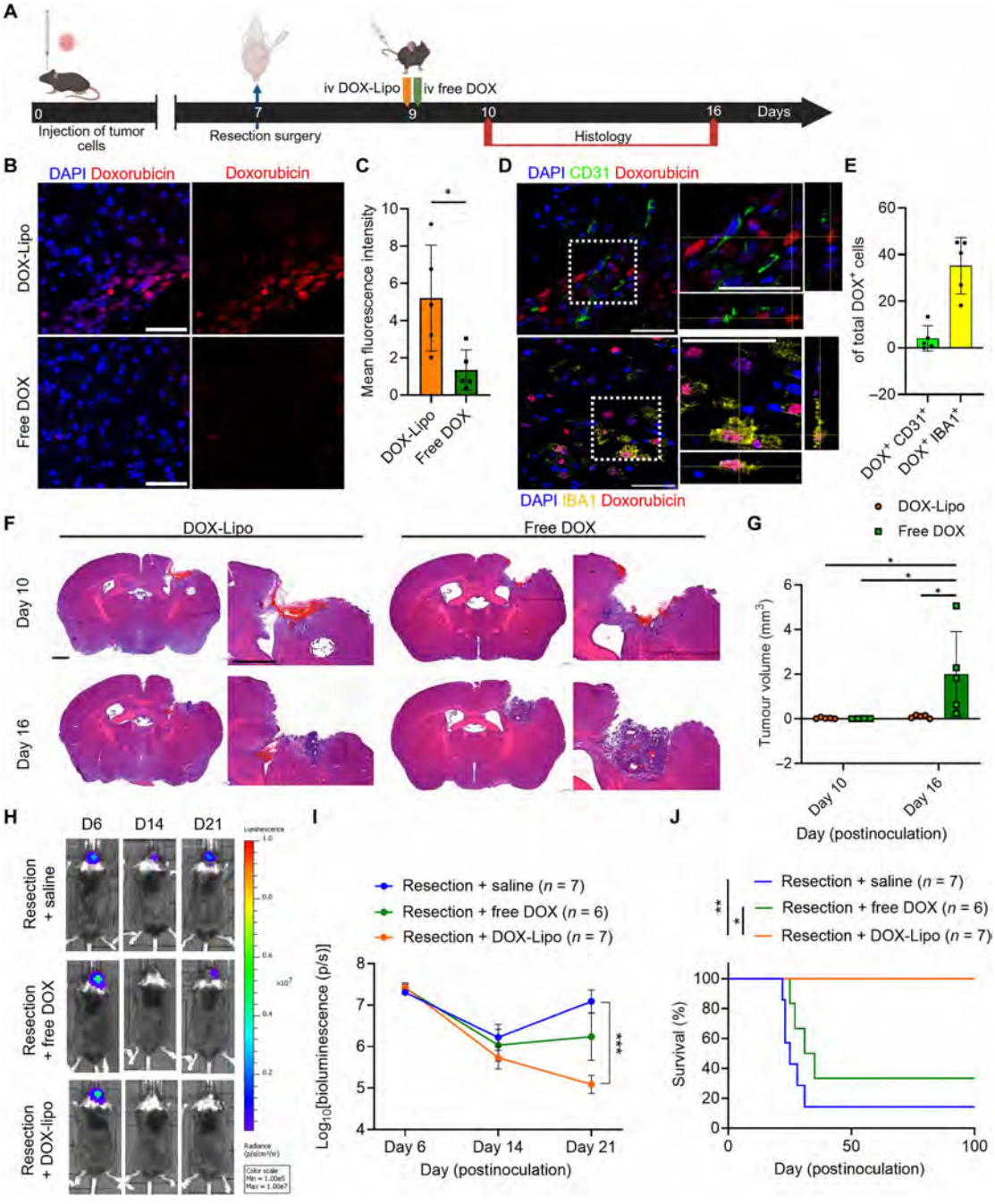


**Fig. 5. Enhanced resection margin–localized liposome-mediated chemotherapy delivery.** (**A**) Experimental schematic. Mice received either liposomal doxorubicin (DOX-Lipos; doxorubicin, 5 mg/kg) or free doxorubicin (free DOX; 5 mg/kg) via intravenous (iv) injection 48 hours after GL261 tumor resection. Brains were collected either 24 hours (day 10 after inoculation) or 7 days (day 16 after inoculation) after treatment. (**B**) Representative confocal images showing doxorubicin fluorescence at the resection margin 24 hours after administration of DOX-Lipos or free doxorubicin. Scale bar, 50 μm. (**C**) Quantification of doxorubicin fluorescence intensity (mean gray value) at the resection margin (three fields of view per animal; $n = 5$ mice). Data are presented as means ± SD. *P* values were determined using Student's *t* test. (**D**) Representative confocal images showing intracellular doxorubicin signal counterstained with CD31 (endothelial cells) and IBA1 (macrophages/microglia). Scale bars, 50 μm. (**E**) Quantification of intracellular doxorubicin signal in CD31-positive endothelial cells or IBA1-positive macrophages/microglia, expressed as a percentage of total doxorubicin signal (four fields of view per mouse; $n = 5$ mice). Data are presented as means ± SD. (**F**) Representative H&E-stained brain sections from each treatment group, showing the emergence of early recurrent lesions in free doxorubicin–treated animals by day 16 (7 days after treatment). Scale bars, 1 mm. (**G**) Quantification of residual or recurrent tumor volume in each treatment group ($n = 5$). Data are presented as means ± SD. *P* values were determined by two-way ANOVA followed by Tukey's multiple comparisons test. (**H**) Representative IVIS bioluminescence images acquired on days (D) 6, 14, and 21 after inoculation (corresponding to days −1, 7, and 14 postresection) ($n = 6$ or 7). (**I**) Quantification of tumor bioluminescence at each time point, expressed as $\log_{10}$-transformed total flux [photons per second (p/s)] ± SEM ($n = 6$ or 7). *P* values were obtained using two-way ANOVA followed by Tukey's multiple comparisons test. (**J**) Kaplan-Meier survival curves for mice treated with DOX-Lipos, free doxorubicin, or saline control 48 hours after GL261 glioma resection ($n = 6$ or 7). *P* values were determined using the log-rank (Mantel-Cox) test; $^*P < 0.05$, $^{**}P < 0.01$, and $^{***}P < 0.001$.

blood biochemistry, inflammatory biomarkers, and brain tissues in mice receiving the therapeutic dose of DOX-Lipos 48 hours after resection (Fig. 6A). Tumor-free mice were used to eliminate confounding effects of tumor growth. No significant differences were observed in postsurgical weight recovery between vehicle- and DOX-Lipo–treated groups (Fig. 6B). Blood biochemistry (albumin and alanine aminotransferase) and plasma inflammatory cytokines (tumor necrosis factor–α and interleukin-6) showed no significant changes, indicating the absence of systemic toxicity (Fig. 6C). Histopathological analysis of brain tissue revealed no evidence of bleeding, edema, necrosis, or fibrosis with DOX-Lipo accumulation at the resection margin (Fig. 6D). Off-target organs known to accumulate liposomes also showed no histological alterations, consistent with the established long-term clinical safety of this systemically used liposomal formulation (Fig. 6E). Collectively, these data demonstrate that the early postoperative window of BBB disruption provides an opportunity for safe and effective administration of therapeutic liposomes.

### Early administration of liposomes within the window of BBB permeability is critical to therapeutic outcome

To validate this in a highly invasive, stem cell–driven glioma model (mGNS; *NRAS$^{G12V}$:shTP53-GFP:shATRX:luciferase*) and to assess the impact of injection timing, we performed a single intravenous dose of DOX-Lipos either 48 hours or 8 days after tumor resection, representing administration in or outside the observed permeability window based on liposome histology and predicted by DCE-MRI (Fig. 7A). The delayed 8-day dose also reflects the typical timing of postoperative treatments in the SoC and most clinical trials of therapeutics, including liposomal drugs (*11*). Early administration of DOX-Lipos led to a profound delay in tumor recurrence in all treated animals (Fig. 7, B and C), translating into a significant ($P < 0.0001$) survival advantage, with 4 of 10 animals exhibiting complete responses with no detectable tumor at day 80 after inoculation (Fig. 7, D to F). In contrast, delayed administration beyond the window of BBB permeability or treatment in the absence of surgical resection provided minimal therapeutic benefit (Fig. 7E). Conventional chemotherapeutics, including free doxorubicin (5 mg/kg) or TMZ (25 mg/kg), were ineffective even when administered in the same windows, highlighting the critical importance of liposomal delivery and margin-localized drug accumulation for efficacy (fig. S24). Similar time-dependent effects were observed in the GL261 model (fig. S25). Together, these results underscore the therapeutic relevance of the early postoperative BBB permeability window and demonstrate that margin-targeted liposomal therapies administered in this period can achieve potent, durable antitumor effects, offering a translationally actionable strategy to suppress GBM recurrence.

## DISCUSSION

Surgical resection is a cornerstone of standard care; however, its effects on BBB permeability in the surrounding brain and the implications for postoperative drug delivery have not been systematically defined. Here, we demonstrate that tumor resection induces a spatially restricted and transient increase in BBB permeability in the peritumoral and resection margin regions. This surgery-induced permeability enables preferential and prolonged accumulation of systemically administered liposomal nanoparticles at the resection margin, a clinically critical site of residual disease. These dynamic changes have consequences for the effectiveness of postoperative chemotherapy, revealing the opportunity for early treatment initiation in specific defined temporal windows.

Doxorubicin was originally considered a promising chemotherapeutic agent for GBM on the basis of its potent cytotoxicity in vitro (*43*). However, free doxorubicin fails to achieve therapeutic concentrations in brain tumors in vivo because of poor BBB penetration and active endothelial efflux, resulting in minimal clinical efficacy (*45*, *48*). Liposomal doxorubicin formulations partially address this limitation, a phenomenon previously demonstrated preclinically and in patients (*49*, *50*). Consequently, multiple clinical studies have evaluated liposomal doxorubicin in newly diagnosed and recurrent GBM, with mixed outcomes ranging from disease stabilization to modest survival benefit (*47*, *50*–*57*). In these trials, liposomal doxorubicin was administered weeks after resection, typically concurrent with or after radiotherapy or in the absence of surgery, when the peritumoral BBB is largely intact. Our data suggest that this delayed treatment paradigm fails to exploit transient, surgery-induced windows of BBB permeability at the resection margin. By administering liposomal doxorubicin in such defined postoperative temporal windows, we demonstrate in this work robust suppression of recurrence and durable disease control, revealing that therapeutic efficacy is critically dependent on timing relative to BBB state, rather than drug choice alone.

Several strategies have previously been explored to overcome BBB constraints for postoperative GBM therapy, including transferrin receptor–mediated delivery using ligand-functionalized nanoparticles or exosome-coated nanomicelles, to promote translocation into the resection margin (*58*). Alternative strategies have sought to exploit postoperative inflammation by harnessing cellular trafficking mechanisms (*59*–*61*). Although effective in experimental models, these approaches are highly dependent on precise timing and complex biological interactions. For example, neutrophil-based systems require administration during the acute inflammatory phase immediately after surgery, whereas platelet-mimetic nanoparticles must be delivered preoperatively, because postoperative thrombus formation markedly restricts parenchymal access. Our study identified two distinct and reproducible postoperative windows of BBB permeability, an immediate window within 15 min and a delayed window at 48 to 72 hours after resection, that can be exploited using a clinically approved, systemically administered liposomal formulation that is otherwise non–BBB-permeant. By leveraging surgery-induced BBB permeability rather than engineered targeting or cellular hijacking, this approach significantly enhances therapeutic efficacy while maintaining compatibility with existing clinical workflows. The use of established liposomal platforms offers substantial translational advantages, including scalable manufacturing, regulatory familiarity, and a well-defined human safety profile, supporting rapid clinical implementation. Furthermore, given the greater (general) disruption to the BBB confirmed after surgery in this study using MRI, this suggests that other approaches could also be used to exploit this window, such as cell therapies [e.g., chimeric antigen receptor (CAR) T and CAR M cells], immunotherapies including checkpoint antibodies, or more advanced lipid nanoparticle delivery systems transporting mRNA or CRISPR therapeutics to the resection marginal zone tissue. Moreover, given the recent advances in identifying the existing neuron-glioma synaptic network in brain cancer as part of the tumorigenic supportive microenvironment (*62*, *63*), the marginal zone–targeted delivery of molecules with the biological capacity to disrupt such a network could offer translational opportunities of such principles and novel adjuvant therapeutics based on cancer neuroscience. These findings suggest

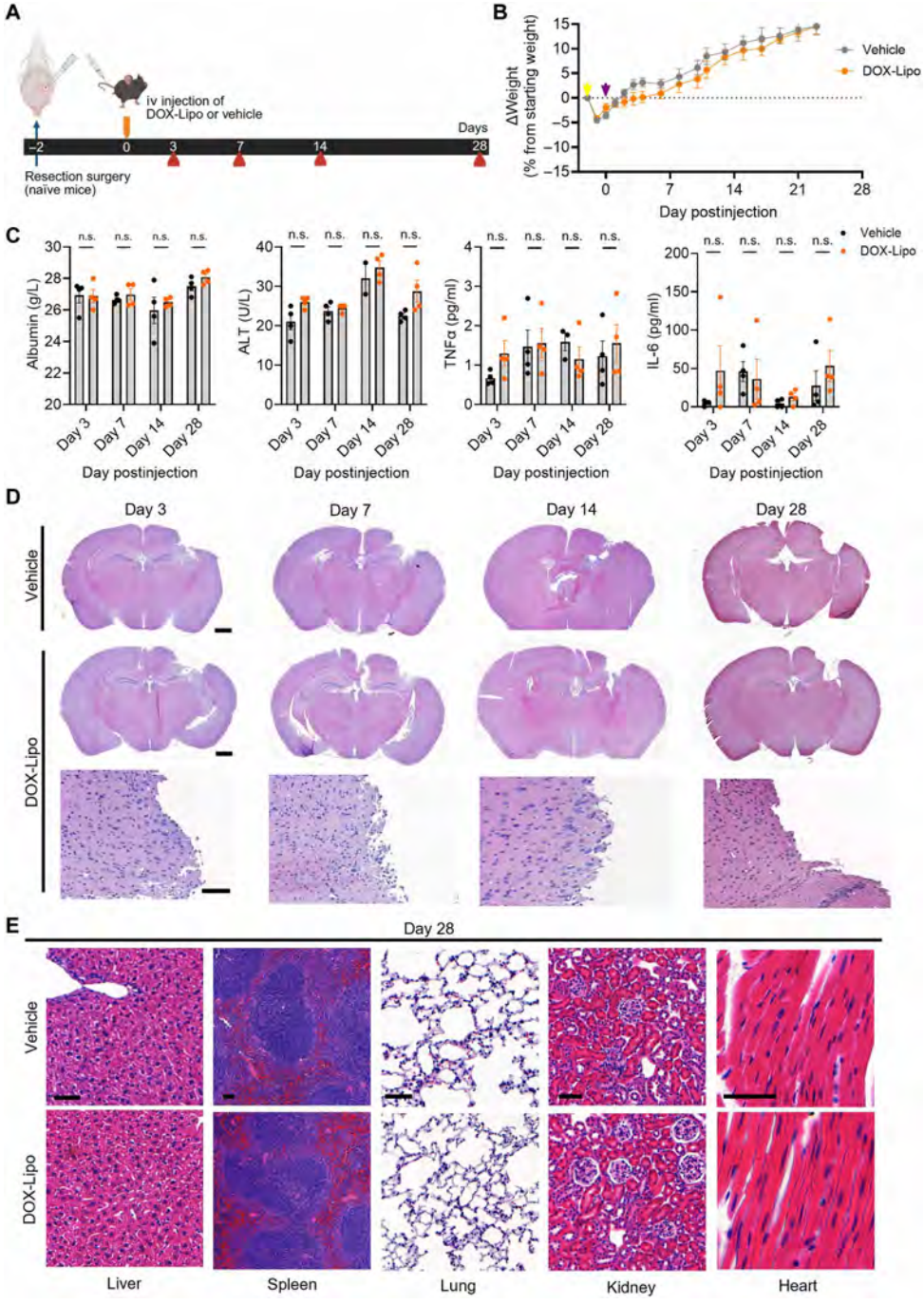


**Fig. 6. Early postoperative liposomal doxorubicin does not cause local or systemic toxicity.** (**A**) Experimental schematic. Naïve (non–tumor-bearing) mice underwent surgical resection of a defined volume of healthy cortical tissue comparable to a typical tumor resection. Mice received intravenous (iv) administration of liposomal doxorubicin (DOX-Lipos; doxorubicin, 5 mg/kg) or vehicle control 48 hours after surgery and were euthanized for blood collection and tissue histopathological analysis on days 3, 7, 14, and 28 after administration. (**B**) Body weight change (Δ), expressed as a percentage of preresection baseline weight ($n = 4$). The yellow arrow indicates the time of surgical resection, and the purple arrow indicates intravenous administration. Data are presented as means ± SEM. Statistical analysis was performed using two-way ANOVA followed by Tukey's multiple comparisons test. (**C**) Biochemical analysis of plasma albumin [grams per liter (g/L)]; alanine aminotransferase [ALT; units per liter (U/L)] and enzyme-linked immunosorbent assay analysis of plasma tumor necrosis factor–α [TNFα; picograms per milliliter (pg/ml)] and interleukin-6 (IL-6; pg/ml) cytokine levels measured on days 3, 7, 14, and 28 after administration of DOX-Lipos or vehicle. Data are presented as means ± SEM. Statistical analysis was performed using Mann-Whitney test. (**D**) Representative H&E-stained brain sections from mice administered vehicle or DOX-Lipos (5 mg/kg) 48 hours after cortical resection, with low-magnification overviews and high-magnification images of the resection margin. No histopathological abnormalities were observed at any time point between days 3 and 28 after administration in any animal ($n = 4$). Scale bars, 1 mm (overview) and 100 μm (high magnification). (**E**) Representative end-point H&E histopathology of livers, spleens, lungs, kidneys, and heart tissues from mice treated with vehicle or DOX-Lipos (5 mg/kg). Scale bars, 50 μm. No histopathological abnormalities or signs of organ toxicity were observed in any tissue analyzed (four independent fields of view per organ; $n = 4$ mice per group) [not significant (n.s.)].

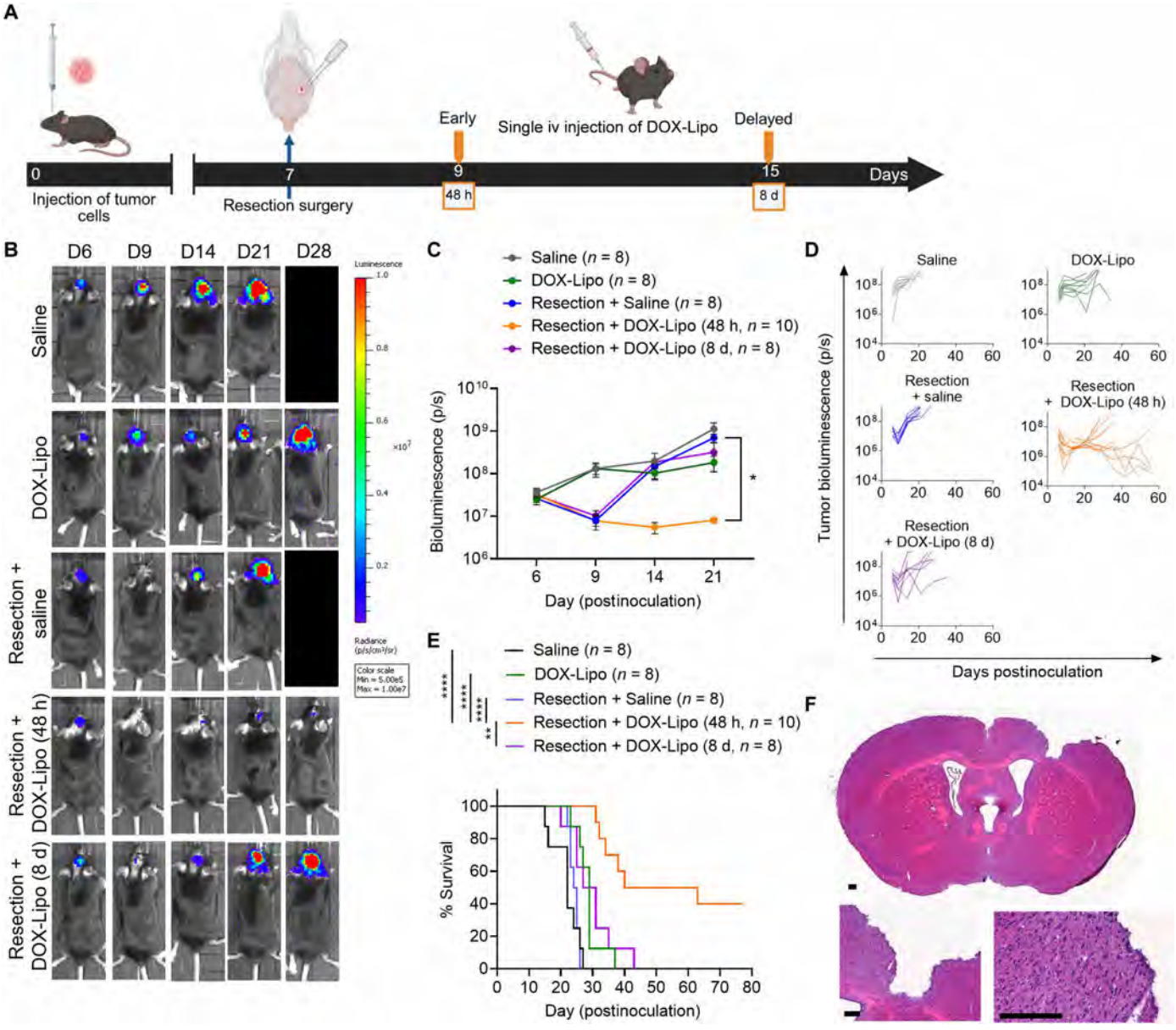


**Fig. 7. Early administration of liposomes in the window of BBB permeability is critical to therapeutic outcome.** (**A**) Experimental schematic. After resection of mGNS ($NRAS^{G12V}$;shTP53-GFP;shATRX;luciferase) tumors, mice received a single intravenous (iv) administration of liposomal doxorubicin (DOX-Lipos; doxorubicin, 5 mg/kg) either 48 hours or 8 days after surgery. Postoperative tumor regrowth was monitored longitudinally using in vivo bioluminescence imaging. (**B**) Representative IVIS bioluminescence images acquired on days (D) 6, 9, 14, 21, and 28 after inoculation, corresponding to days −1, 2, 7, 14, and 21 after resection. (**C**) Quantification of tumor bioluminescence expressed as total flux [photons per second (p/s)]. Data are presented as means ± SEM ($n = 8$ to 10). *P* values were obtained using two-way ANOVA followed by Tukey's multiple comparisons test. (**D**) Tumor bioluminescence [total flux, photons per second (p/s)] of individual mice in each treatment group ($n = 8$ to 10). (**E**) Kaplan-Meier survival curves for mGNS tumor–bearing mice treated with saline, DOX-Lipos (5 mg/kg) alone, resection and saline, or resection and DOX-Lipos administered either 48 hours or 8 days after resection ($n = 8$ to 10). *P* values were determined using the log-rank (Mantel-Cox) test. (**F**) Representative H&E-stained brain sections from surviving mice at study end point. No tumor mass or residual tumor cells were detected by histopathological analysis (12 independent sections from $n = 4$ mice). Scale bars, 200 μm. $^{*}P < 0.05$, $^{**}P < 0.01$, and $^{****}P < 0.0001$. h, hours; d, days.

that exploiting predictable, surgery-induced BBB dynamics may represent a previously unexplored generalizable and clinically tractable strategy.

In clinical practice, postoperative BBB disruption has been inferred from nonspecific or reactive contrast enhancement on standard MRI, particularly when imaging is performed beyond 48 hours after surgery (*16*–*18*). However, the kinetics, spatial extent, and functional significance of this enhancement have not been quantitatively validated as measures of BBB permeability using DCE-MRI. In a clinical trial setting, noninvasive biomarkers capable of assessing resection-margin BBB permeability will be essential to identify optimal time windows for liposomal drug administration. Our findings demonstrate

that routinely available DCE-MRI can detect and track the spatiotemporal dynamics of postoperative BBB permeability, supporting its potential utility as a predictive and stratification biomarker for nanoparticle delivery to the resection margin.

The conventional 4- to 6-week delay between GBM resection and initiation of chemoradiotherapy has largely been adopted to allow postoperative recovery before sustained, untargeted exposure to cytotoxic therapy and is routinely maintained in clinical trials of investigational agents. However, accumulating clinical evidence demonstrates that earlier intervention is both feasible and safe, with favorable outcomes reported for early (2 to 3 weeks) (*64*, *65*) and even "super-early" (<7 days) administration of TMZ (<7 days) (*66*). In parallel, immediate intra- or postoperative local therapies, including carmustine wafers (Gliadel) and brachytherapy approaches (Gammatile), are already clinically approved, underscoring the therapeutic value of targeting the postoperative period (*67*, *68*). This noninvasive liposome strategy can integrate with SoC, avoids repeated dosing that may compromise postoperative recovery, and demonstrates no overt toxicity in preclinical models. By providing systemic, margin-targeted delivery, this strategy could serve as a complementary or alternative approach to existing locoregional therapies.

More broadly, given that similar BBB permeability changes were observed after surgical resection in the absence of tumor, this approach may extend beyond GBM to other resectable brain tumors (e.g., brain metastases) and neurological diseases (e.g., epilepsy) using surgical resection approaches as part of the treatment protocols. Our findings also support a shift toward biologically informed, time-dependent postoperative therapy, establishing a framework for integrating systemically administered nanomedicines into neuro-oncological care. Generally, these findings should motivate focused clinical investigations to establish feasibility, safety, and optimal timing in patients to unlock multiple opportunities for systemically administered nanoparticle-based adjuvant therapeutics.

Several limitations should be considered. Although therapeutic benefit is demonstrated here, the underlying mechanism remains incompletely defined. Liposomal uptake occurs predominantly in macrophages and microglia, and the relative contributions of direct tumor cell killing, immune modulation, and bystander effects require further investigation. Although liposomal doxorubicin has an established clinical safety profile, the feasibility and safety of systemic administration in the immediate postoperative period requires careful evaluation, particularly in the context of acute surgical recovery and variability in clinical management. Further optimization of nanoparticle design may improve targeting efficiency and reduce off-target accumulation. Clinical heterogeneity also warrants consideration. The use of hemostatic agents, local drug depots (e.g., Gliadel), and cavity-filling materials may alter postoperative responses and influence nanoparticle delivery. These interventions could also be strategically leveraged to enhance or extend therapeutic efficacy. Last, although findings were validated here across multiple preclinical models, additional studies in more clinically representative settings, including patient-derived and large-animal models, and across variable surgical conditions (e.g., extent of resection, tumor location, and operative techniques) will be important to confirm robustness and support clinical translation.

In conclusion, we demonstrate that systemic (intravenous) administration of liposomes in defined temporal windows of postoperative BBB permeability results in selective accumulation at the resection margin, a critical and otherwise therapeutically inaccessible site in GBM. This surgery-induced, spatially restricted, and transient BBB permeability has important implications for the design of both preclinical and clinical trials of poor BBB-penetrant therapeutics and suggests that early postoperative administration should be more widely considered. By exploiting this window for the targeted delivery and accumulation of the clinically approved liposomal doxorubicin, we effectively suppressed tumor recurrence in an aggressive resection–recurrence model. Together, these findings indicate that repurposing existing nanoparticle-based therapeutics offers a readily translatable strategy with the potential to improve outcomes in GBM and other resectable brain tumors.

## MATERIALS AND METHODS

### Study design

This study was designed to investigate the impact of surgical resection of GBM on the local BBB that can be exploited to enhance delivery of systemically administered therapeutic agents to the resection margin. Through combining syngeneic murine GBM resection models with biodistribution analyses and in vivo/ex vivo imaging, we focused on assessment of the brain penetrance and microenvironmental interactions of clinically used liposomal formulations. These were then used in therapeutic intervention studies to validate the impact of this postoperative spatiotemporal BBB disruption. Statisticians (Inferstats, UK) were consulted during the design and ethical approval of the Home Office project license (PP3096857) governing these studies, which included power calculations ($\alpha = 0.05$, 0.8 power) of relevant experimental outcomes. Exact *n* values for each experiment, which reflect biological replicates (individual animals), are provided in the figure legends. Where applicable, repeated experiments on separate cohorts were also performed, which are included in the stated *n*. Inclusion criteria for animal studies included successful tumor establishment before resection and measurable decrease in the tumor (bioluminescence signal) after resection. Animals that failed either of these were excluded at the time of randomization. In all experiments, animals were randomly assigned to treatment groups after baseline bioluminescence imaging to ensure comparable residual tumor burden across groups. Data collection end points were predefined for specific experiments, including humane end points for survival studies (e.g., weight loss or neurological symptoms) and fixed time points for biodistribution and imaging analyses. Outliers were not excluded unless attributable to technical failure. Blinding was implemented for key outcome measures, including bioluminescence imaging acquisition, animal monitoring, humane end-point decisions, and downstream image analysis (confocal and MRI). Allocation was concealed until primary analysis was completed.

### Cell lines and culture conditions

GL261-luc cells were provided by B. Bigger (University of Manchester). GL261 cells were expanded as adherent cultures in RPMI (Gibco) supplemented with 10% fetal bovine serum (Gibco) and 1% penicillin and streptomycin (P/S; Gibco). The mGNS line ($NRAS^{G12V}$;shTP53-GFP;shATRX;luciferase) (*33*, *34*) was provided by M. Castro (University of Michigan). These cells were cultured in suspension as undifferentiated neurospheres in Dulbecco's modified Eagle's medium/F12 (Gibco) supplemented with 1× B-27 (Gibco), 1× N2 (Gibco), 1% P/S, murine epidermal growth factor (mEGF) (20 ng/ml; PeproTech), and murine fibroblast growth factor (mFGF) (20 ng/ml; PeproTech). Cells were maintained at 37°C and 5% $CO_2$ in a humidified environment and were regularly tested and confirmed free from mycoplasma. For inoculation,

cells were detached/dissociated using Accutase (Thermo Fisher Scientific) and washed two times in phosphate-buffered saline (PBS) to remove medium components.

### Animals

All animal experiments were performed at the University of Manchester (UK), in accordance with the Animals (Scientific Procedures) Act 1986 (UK), approved by the University of Manchester Ethical Review Committee and under a UK Home Office Project License P089E2E0A/PP3096857. Animals were housed in groups in ventilated cages with ad libitum access to food and water; 10-week-old female C57BL/6 mice were purchased from Charles River, UK and were allowed to acclimatize to the facility for at least 1 week before any procedure.

### Intracranial inoculation of glioma cells

Mice were inoculated with syngeneic GBM cells as previously described (*69*). Adult female C57BL/6 mice (10 to 11 weeks old) were anesthetized using isoflurane (2.5% induction and 1 to 2% maintenance in medical oxygen, at a rate of 1.5 liters/min) and placed on a stereotactic frame. Before incision, animals received buprenorphine (0.1 mg/kg; Buprenex, Reckitt Benckiser). A midline incision was performed to expose the cranium, and a 0.7-mm borehole was drilled (Fine Science Tools, Canada) above the right striatum at 0.7 mm anterior and 2.4 mm lateral from bregma. A 10-μl Hamilton syringe (SYR10, Hamilton) fitted with a 26-gauge blunt needle (Hamilton) was lowered to 1.5 mm below the cortical surface and slowly withdrawn 0.5 mm such that the injection took place at a 1.0-mm depth; $5 \times 10^4$ GL261-luc or mGNS cells in 1 μl of PBS were injected slowly over 5 min at a rate of 0.2 μl/min. After injection, the needle was kept in place for 3 min to minimize reflux and was slowly withdrawn over 1 min to minimize any injury. The skin incision was closed with 6-0 coated Vicryl sutures (Ethicon), and animals were allowed to recover in a heated environment.

### Resection surgery

Tumor-bearing or non–tumor-bearing control mice were anesthetized using isoflurane (2.5% induction and 1 to 2% maintenance in medical oxygen, at a rate of 1.5 liters/min) and placed on a stereotactic frame. Before incision, animals received buprenorphine (0.1 mg/kg) and dexamethasone (0.1 mg/kg). A midline incision was performed to expose the cranium near the previous borehole made. A craniotomy was performed using a dental drill (NSK-Nakanishi) to expose the brain at the tumor site. The dura was incised, and the tumor was resected via aspiration using a vacuum pump (Integra VACUSIP, VWR), and resection of all visible tumor mass was performed in all experimental groups. For non–tumor-bearing control groups, a comparable volume of healthy brain was removed. Hemostasis was achieved using a combination of temporary application of hemostatic sponge (Hygitech) followed by repeat flushing with saline. On confirmation of effective and complete hemostasis, the craniotomy skull cap was placed back above the brain tissue and sealed with Kwik-Sil (World Precision Instruments). Last, mice were sutured, provided with 0.9% saline, and allowed to recover in a heat box with mash food and continuous monitoring.

### In vivo bioluminescence imaging

Tumor-bearing or surgically resected mice received an intraperitoneal injection of D-luciferin (150 mg/kg; 15 mg/ml in PBS; Promega) followed by anesthesia with 1.5% isoflurane. Bioluminescence signals were acquired 8 min after injection using an in vivo imaging system (IVIS; IVIS Lumina II, PerkinElmer), with sequential imaging performed every 2 min over a 30-min period (15 acquisitions). Images were analyzed using Living Image software (version 4.7; PerkinElmer). Tumor bioluminescence was quantified as total photon flux (photons per second) and log transformed for subsequent statistical analysis.

### Intravenous liposome biodistribution

Mice were intravenously administered fluorescently labeled liposomes (DiI or DiD labeled, as specified for individual experiments) at 12.5 mM lipid concentration suspended in Hepes buffer. Liposomes were injected at defined time points relative to surgical resection or sham surgery (no procedure), including preresection (−15 min) or postresection time points (15 min, 3 hours, 24 hours, 48 hours, 72 hours, or 7 days), depending on the experimental design. Animals were euthanized at specified intervals after liposome administration (ranging from 3 to 120 hours after injection), as indicated in the corresponding figure legends. Mice were anaesthetized with 2.5% isoflurane and perfused via cardiac perfusion with 2 mM EDTA in PBS to remove circulating blood and unbound liposomes. Brains and peripheral organs (hearts, lungs, livers, kidneys, and spleens) were harvested and imaged ex vivo using an IVIS Lumina II (PerkinElmer) with 549-nm excitation and 565-nm emission for DiI or 640-nm excitation and 695-nm emission for DiD fluorophores. Fluorescence images were analyzed using Living Image software (version 4.7; PerkinElmer). After IVIS imaging, brains were either fixed in 4% paraformaldehyde (PFA) for histological and immunofluorescence analyses or processed fresh for flow cytometric analysis, depending on the experimental end point. Specific tissue processing workflows are detailed in Supplementary Materials and Methods.

### Magnetic resonance imaging

Tumor-bearing mice underwent MRI on a 7.0-T Agilent magnet interfaced to Bruker Avance III console. Mice were scanned at baseline, 6 days after tumor inoculation. On day 7, $n = 4$ tumor-bearing mice were submitted to a resection surgery and assessed with MRI 24 hours, 48 hours, and 8 days after surgery. $n = 2$ mice from the initial group did not undergo resection and were scanned with MRI at the same time points as resected mice to assess BBB permeability in nonresected mice. Each MRI session consisted of T2-TurboRARE MRI and DCE-MRI. Full MRI parameters and analysis are included in Supplementary Materials and Methods.

### Therapeutic treatment design

DOX-Lipos (doxorubicin, 5 mg/kg), free doxorubicin (5 mg/kg), free TMZ (25 mg/kg), or vehicle control was administered intravenously as a single dose at 15 min, 48 hours, 8 days, or 10 days after tumor resection or unresected control, as specified in the figure legends. Treatments were evaluated in GL261- or mGNS-inoculated mice. Animals were monitored daily for body weight, general health, and neurological symptoms. Postoperative tumor regrowth was assessed longitudinally by in vivo bioluminescence imaging. Animals were euthanized upon reaching predefined humane end points, including >15% weight loss or the onset of neurological deficits, and brains were collected for histological analysis. Initial postoperative bioluminescence measurements were used to randomize animals such that each treatment group had comparable mean residual tumor burdens at baseline. Bioluminescence acquisition, animal monitoring, and humane end-point decisions were performed in a blinded manner.

### Safety study

To assess the safety of doxorubicin-loaded liposomes in the early postoperative period, non–tumor-bearing naïve mice underwent surgical resection of a cortical region of comparable volume to that removed during tumor resection. Forty-eight hours after surgery, mice received an intravenous injection of liposomal doxorubicin (5 mg/kg, doxorubicin equivalent) or saline vehicle control. Animals were monitored daily for 28 days for changes in body weight, general behavior, and wound healing. At days 3, 7, 14, and 28 after treatment, mice were euthanized by cardiac puncture to collect blood (details of blood analysis included in Supplementary Materials and Methods), followed by transcardial perfusion with PBS containing 2 mM EDTA and subsequent fixation with 4% PFA. Organs (brains, hearts, lungs, spleens, kidneys, livers, and cervical lymph nodes) were dissected and fixed overnight in 4% PFA, then processed, and embedded in paraffin wax. Formalin-fixed paraffin-embedded tissue sections were cut at a thickness of 5 μm using a microtome. Sections were stained with H&E using a Leica Autostainer XL ST5010 (Leica), scanned with a 3DHISTECH Panoramic 250 slide scanner, and visualized using 3DHISTECH Case Viewer software (version 2.6). Four independent sections from anatomically distinct regions of each organ were subjected to detailed histopathological assessment, with findings compared with saline-treated controls, and any abnormalities were recorded.

### Statistical analysis

All statistical analyses were performed using GraphPad Prism 10. When the sample size permitted, normality was assessed using the Shapiro-Wilk test. For tumor growth data (bioluminescence imaging), this analysis was performed on log-transformed luminescence values. For datasets that deviated from normality, nonparametric tests were applied. Comparisons between two groups were conducted using unpaired two-tailed Student's *t* tests or Mann-Whitney *U* test as appropriate. Comparisons among three or more groups were performed using ordinary one-way analysis of variance (ANOVA) followed by Tukey's multiple comparisons test, two-way ANOVA followed by Tukey's or Šidák's multiple comparisons test, or Kruskal-Wallis test, as appropriate. Survival data were analyzed using the log-rank (Mantel-Cox) test. $P < 0.05$ was considered statistically significant. Exact *P* values and the statistical tests applied are specified in the corresponding figure legends. Data are presented as means ± SD or means ± SEM, as indicated in each figure legend. Reported *n* values are individual mice, which are presented as individual data points in the presented data and explicitly stated in the relevant figure legends. All individual-level data for $n < 20$ are presented in data file S1.

## Supplementary Materials

**The PDF file includes:**
Supplementary Materials and Methods
Figs. S1 to S25
References (*70*, *71*)

**Other Supplementary Material for this manuscript includes the following:**
Data file S1
MDAR Reproducibility Checklist

## REFERENCES AND NOTES


1. K. D. Miller, Q. T. Ostrom, C. Kruchko, N. Patil, T. Tihan, G. Cioffi, H. E. Fuchs, K. A. Waite, A. Jemal, R. L. Siegel, J. S. Barnholtz-Sloan, Brain and other central nervous system tumor statistics, 2021. *CA Cancer J. Clin.* **71**, 381–406 (2021).
2. C. Jackson, J. Choi, A. M. Khalafallah, C. Price, C. Bettegowda, M. Lim, G. Gallia, J. Weingart, H. Brem, D. Mukherjee, A systematic review and meta-analysis of supratotal versus gross total resection for glioblastoma. *J. Neurooncol* **148**, 419–431 (2020).
3. J. Yoo, S.-J. Yoon, K. H. Kim, I.-H. Jung, S. H. Lim, W. Kim, H. I. Yoon, S. H. Kim, K. S. Sung, T. H. Roh, J. H. Moon, H. H. Park, E. H. Kim, C. O. Suh, S. G. Kang, J. H. Chang, Patterns of recurrence according to the extent of resection in patients with IDH–wild-type glioblastoma: A retrospective study. *J. Neurosurg.* **137**, 533–543 (2021).
4. R. Stupp, W. P. Mason, M. J. Van Den Bent, M. Weller, B. Fisher, M. J. Taphoorn, K. Belanger, A. A. Brandes, C. Marosi, U. Bogdahn, J. Curschmann, R. C. Janzer, S. K. Ludwin, T. Gorlia, A. Allgeier, D. Lacombe, J. G. Cairncross, E. Eisenhauer, R. O. Mirimanoff, European Organisation for Research and Treatment of Cancer Brain Tumor and Radiotherapy Groups, National Cancer Institute of Canada Clinical Trials Group, Radiotherapy plus concomitant and adjuvant temozolomide for glioblastoma. *N. Engl. J. Med.* **352**, 987–996 (2005).
5. K. Aldape, K. M. Brindle, L. Chesler, R. Chopra, A. Gajjar, M. R. Gilbert, N. Gottardo, D. H. Gutmann, D. Hargrave, E. C. Holland, D. T. W. Jones, J. A. Joyce, P. Kearns, M. W. Kieran, I. K. Mellinghoff, M. Merchant, S. M. Pfister, S. M. Pollard, V. Ramaswamy, J. N. Rich, G. W. Robinson, D. H. Rowitch, J. H. Sampson, M. D. Taylor, P. Workman, R. J. Gilbertson, Challenges to curing primary brain tumours. *Nat. Rev. Clin. Oncol.* **16**, 509–520 (2019).
6. D. M. Müller, M. E. De Swart, H. Ardon, F. Barkhof, L. Bello, M. S. Berger, W. Bouwknegt, W. A. Van den Brink, M. Conti Nibali, R. S. Eijgelaar, J. Furtner, S. J. Han, S. Hervey-Jumper, A. J. S. Idema, B. Kiesel, A. Kloet, E. Mandonnet, P. A. J. T. Robe, M. Rossi, T. Sciortino, W. P. Vandertop, M. Visser, M. Wagemakers, G. Widhalm, M. G. Witte, P. C. De Witt Hamer, Timing of glioblastoma surgery and patient outcomes: A multicenter cohort study. *Neurooncol. Adv.* **3**, vdab053 (2021).
7. A. L. Stensjøen, O. Solheim, K. A. Kvistad, A. K. Håberg, Ø. Salvesen, E. M. Berntsen, Growth dynamics of untreated glioblastomas in vivo. *Neuro Oncol.* **17**, 1402–1411 (2015).
8. M. Waqar, F. Roncaroli, E. J. Lehrer, J. D. Palmer, J. Villanueva-Meyer, S. Braunstein, E. Hall, M. Aznar, P. C. De Witt Hamer, P. I. D'Urso, D. Trifiletti, A. Quiñones-Hinojosa, P. Wesseling, G. R. Borst, Rapid early progression (REP) of glioblastoma is an independent negative prognostic factor: Results from a systematic review and meta-analysis. *Neurooncol. Adv.* **4**, vdac075 (2022).
9. A. Merkel, D. Soeldner, C. Wendl, D. Urkan, J. B. Kuramatsu, C. Seliger, M. Proescholdt, I. Y. Eyupoglu, P. Hau, M. Uhl, Early postoperative tumor progression predicts clinical outcome in glioblastoma—Implication for clinical trials. *J. Neurooncol* **132**, 249–254 (2017).
10. J. E. Villanueva-Meyer, S. J. Han, S. Cha, N. A. Butowski, Early tumor growth between initial resection and radiotherapy of glioblastoma: Incidence and impact on clinical outcomes. *J. Neurooncol* **134**, 213–219 (2017).
11. T. Kisby, G. Borst, D. Coope, K. Kostarelos, Targeting the glioblastoma resection margin with locoregional nanotechnologies. *Nat. Rev. Clin. Oncol.* **22**, 517–537 (2025).
12. M. Waqar, D. M. Trifiletti, C. McBain, J. O'connor, D. J. Coope, L. Akkari, A. Quinones-Hinojosa, G. R. Borst, Early therapeutic interventions for newly diagnosed glioblastoma: Rationale and review of the literature. *Curr. Oncol. Rep.* **24**, 311–324 (2022).
13. J. N. Sarkaria, L. S. Hu, I. F. Parney, D. H. Pafundi, D. H. Brinkmann, N. N. Laack, C. Giannini, T. C. Burns, S. H. Kizilbash, J. K. Laramy, K. R. Swanson, T. J. Kaufmann, P. D. Brown, N. Y. R. Agar, E. Galanis, J. C. Buckner, W. F. Elmquist, Is the blood–brain barrier really disrupted in all glioblastomas? A critical assessment of existing clinical data. *Neuro Oncol.* **20**, 184–191 (2018).
14. E. K. Nduom, C. Yang, M. J. Merrill, Z. Zhuang, R. R. Lonser, Characterization of the blood-brain barrier of metastatic and primary malignant neoplasms. *J. Neurosurg.* **119**, 427–433 (2013).
15. M. Niyazi, N. Andratschke, M. Bendszus, A. J. Chalmers, S. C. Erridge, N. Galldiks, F. J. Lagerwaard, P. Navarria, P. M. A. Rosenschöld, U. Ricardi, M. J. van den Bent, M. Weller, C. Belka, G. Minniti, ESTRO-EANO guideline on target delineation and radiotherapy details for glioblastoma. *Radiother. Oncol.* **184**, 109663 (2023).
16. C. Bastiancich, E. Snacel-Fazy, S. Fernandez, S. Robert, R. Stacchini, L. Plantureux, S. Boissonneau, B. Testud, B. Guillet, F. Debarbieux, H. Luche, D. Figarella-Branger, M. A. Estève, E. Tabouret, A. Tchoghandjian, Tailoring glioblastoma treatment based on longitudinal analysis of post-surgical tumor microenvironment. *J. Exp. Clin. Cancer Res.* **43**, 311 (2024).
17. S. Bette, J. Gempt, T. Huber, T. Boeckh-Behrens, F. Ringel, B. Meyer, C. Zimmer, J. S. Kirschke, Patterns and time dependence of unspecific enhancement in postoperative magnetic resonance imaging after glioblastoma resection. *World Neurosurg.* **90**, 440–447 (2016).
18. S. Lescher, S. Schniewindt, A. Jurcoane, C. Senft, E. Hattingen, Time window for postoperative reactive enhancement after resection of brain tumors: Less than 72 hours. *Neurosurg. Focus* **37**, E3 (2014).
19. M. Rapp, J. Baernreuther, B. Turowski, H.-J. Steiger, M. Sabel, M. A. Kamp, Recurrence pattern analysis of primary glioblastoma. *World Neurosurg.* **103**, 733–740 (2017).
20. A. M. Molinaro, S. Hervey-Jumper, R. A. Morshed, J. Young, S. J. Han, P. Chunduru, Y. Zhang, J. J. Phillips, A. Shai, M. Lafontaine, J. Crane, A. Chandra, P. Flanigan, A. Jahangiri, G. Cioffi,

Q. Ostrom, J. E. Anderson, C. Badve, J. Barnholtz-Sloan, A. E. Sloan, B. J. Erickson, P. A. Decker, M. L. Kosel, D. LaChance, J. Eckel-Passow, R. Jenkins, J. Villanueva-Meyer, T. Rice, M. Wrensch, J. K. Wiencke, N. A. Oberheim Bush, J. Taylor, N. Butowski, M. Prados, J. Clarke, S. Chang, E. Chang, M. Aghi, P. Theodosopoulos, M. McDermott, M. S. Berger, Association of maximal extent of resection of contrast-enhanced and non–contrast-enhanced tumor with survival within molecular subgroups of patients with newly diagnosed glioblastoma. *JAMA Oncol.* **6**, 495–503 (2020).
21. J. Shi, P. W. Kantoff, R. Wooster, O. C. Farokhzad, Cancer nanomedicine: Progress, challenges and opportunities. *Nat. Rev. Cancer* **17**, 20–37 (2017).
22. I. de Lázaro, D. J. Mooney, Obstacles and opportunities in a forward vision for cancer nanomedicine. *Nat. Mater.* **20**, 1469–1479 (2021).
23. D. E. Tylawsky, H. Kiguchi, J. Vaynshteyn, J. Gerwin, J. Shah, T. Islam, J. A. Boyer, D. R. Boué, M. Snuderl, M. B. Greenblatt, Y. Shamay, G. P. Raju, D. A. Heller, P-selectin-targeted nanocarriers induce active crossing of the blood–brain barrier via caveolin-1-dependent transcytosis. *Nat. Mater.* **22**, 391–399 (2023).
24. F. C. Lam, S. W. Morton, J. Wyckoff, T.-L. Vu Han, M. K. Hwang, A. Maffa, E. Balkanska-Sinclair, M. B. Yaffe, S. R. Floyd, P. T. Hammond, Enhanced efficacy of combined temozolomide and bromodomain inhibitor therapy for gliomas using targeted nanoparticles. *Nat. Commun.* **9**, 1991 (2018).
25. M. Charabati, J.-M. Rabanel, C. Ramassamy, A. Prat, Overcoming the brain barriers: From immune cells to nanoparticles. *Trends Pharmacol. Sci.* **41**, 42–54 (2020).
26. T. Kisby, A. Yilmazer, K. Kostarelos, Reasons for success and lessons learnt from nanoscale vaccines against COVID-19. *Nat. Nanotechnol.* **16**, 843–850 (2021).
27. A. A. Gabizon, S. Gabizon-Peretz, S. Modaresahmadi, N. M. La-Beck, Thirty years from FDA approval of pegylated liposomal doxorubicin (Doxil/Caelyx): An updated analysis and future perspective. *BMJ Oncol.* **4**, e000573 (2025).
28. Z. S. Al-Ahmady, D. Jasim, S. S. Ahmad, R. Wong, M. Haley, G. Coutts, I. Schiessl, S. M. Allan, K. Kostarelos, Selective liposomal transport through blood brain barrier disruption in ischemic stroke reveals two distinct therapeutic opportunities. *ACS Nano* **13**, 12470–12486 (2019).
29. Z. S. Al-Ahmady, B. R. Dickie, I. Aldred, D. A. Jasim, J. Barrington, M. Haley, E. Lemarchand, G. Coutts, S. Kaur, J. Bates, S. Curran, R. Goddard, M. Walker, A. Parry-Jones, K. Kostarelos, S. M. Allan, Selective brain entry of lipid nanoparticles in haemorrhagic stroke is linked to biphasic blood-brain barrier disruption. *Theranostics* **12**, 4477–4497 (2022).
30. A. Zinger, S. Soriano, G. Baudo, E. De Rosa, F. Taraballi, S. Villapol, Biomimetic nanoparticles as a theranostic tool for traumatic brain injury. *Adv. Funct. Mater.* **31**, 2100722 (2021).
31. B. J. Boyd, A. Galle, M. Daglas, J. V. Rosenfeld, R. Medcalf, Traumatic brain injury opens blood–brain barrier to stealth liposomes via an enhanced permeability and retention (EPR)-like effect. *J. Drug Target.* **23**, 847–853 (2015).
32. Y. M. Li, D. Suki, K. Hess, R. Sawaya, The influence of maximum safe resection of glioblastoma on survival in 1229 patients: Can we do better than gross-total resection? *J. Neurosurg.* **124**, 977–988 (2016).
33. P. Kadiyala, S. V. Carney, J. C. Gauss, M. B. Garcia-Fabiani, S. Haase, M. S. Alghamri, F. J. Núñez, Y. Liu, M. Yu, A. Taher, F. M. Nunez, D. Li, M. B. Edwards, C. G. Kleer, H. Appelman, Y. Sun, L. Zhao, J. J. Moon, A. Schwendeman, P. R. Lowenstein, M. G. Castro, Inhibition of 2-hydroxyglutarate elicits metabolic reprogramming and mutant IDH1 glioma immunity in mice. *J. Clin. Investig.* **131**, e139542 (2021).
34. F. J. Núñez, F. M. Mendez, P. Kadiyala, M. S. Alghamri, M. G. Savelieff, M. B. Garcia-Fabiani, S. Haase, C. Koschmann, A.-A. Calinescu, N. Kamran, M. Saxena, R. Patel, S. Carney, M. Z. Guo, M. Edwards, M. Ljungman, T. Qin, M. A. Sartor, R. Tagett, S. Venneti, J. Brosnan-Cashman, A. Meeker, V. Gorbunova, L. Zhao, D. M. Kremer, L. Zhang, C. A. Lyssiotis, L. Jones, C. J. Herting, J. L. Ross, D. Hambardzumyan, S. Hervey-Jumper, M. E. Figueroa, P. R. Lowenstein, M. G. Castro, IDH1-R132H acts as a tumor suppressor in glioma via epigenetic up-regulation of the DNA damage response. *Sci. Transl. Med.* **11**, eaaq1427 (2019).
35. S. Reagan-Shaw, M. Nihal, N. Ahmad, Dose translation from animal to human studies revisited. *FASEB J.* **22**, 659–661 (2008).
36. D. Schiff, E. Q. Lee, L. Nayak, A. D. Norden, D. A. Reardon, P. Y. Wen, Medical management of brain tumors and the sequelae of treatment. *Neuro Oncol.* **17**, 488–504 (2015).
37. Z. Tu, H. Xiong, Y. Qiu, G. Li, L. Wang, S. Peng, Limited recurrence distance of glioblastoma under modern radiotherapy era. *BMC Cancer* **21**, 720 (2021).
38. A. K. Heye, R. D. Culling, M. Del C. Valdés Hernández, M. J. Thrippleton, J. M. Wardlaw, Assessment of blood–brain barrier disruption using dynamic contrast-enhanced MRI. A systematic review. *Neuroimage Clin.* **6**, 262–274 (2014).
39. W. J. Harris, M.-C. Asselin, R. Hinz, L. M. Parkes, S. Allan, I. Schiessl, H. Boutin, B. R. Dickie, In vivo methods for imaging blood–brain barrier function and dysfunction. *Eur. J. Nucl. Med. Mol. Imaging* **50**, 1051–1083 (2023).
40. Y. Li, J. M. Lupo, M.-Y. Polley, J. C. Crane, W. Bian, S. Cha, S. Chang, S. J. Nelson, Serial analysis of imaging parameters in patients with newly diagnosed glioblastoma multiforme. *Neuro Oncol.* **13**, 546–557 (2011).
41. Z. P. Lin, L. N. M. Nguyen, B. Ouyang, P. M. Millan, J. Ngai, B. R. Kingston, S. M. Mladjenovic, W. C. W. Chan, Macrophages actively transport nanoparticles in tumors after extravasation. *ACS Nano* **16**, 6080–6092 (2022).
42. J.-N. May, J. I. Moss, F. Mueller, S. K. Golombek, I. Biancacci, L. Rizzo, A. S. Elshafei, F. Gremse, R. Pola, M. Pechar, T. Etrych, S. Becker, C. Trautwein, R. D. Bülow, P. Boor, R. Knuechel, S. von Stillfried, G. Storm, S. Puri, S. T. Barry, V. Schulz, F. Kiessling, M. B. Ashford, T. Lammers, Histopathological biomarkers for predicting the tumour accumulation of nanomedicines. *Nat. Biomed. Eng.* **8**, 1366–1378 (2024).
43. A. Stan, S. Casares, D. Radu, G. Walter, T. Brumeanu, Doxorubicin-induced cell death in highly invasive human gliomas. *Anticancer Res* **19**, 941–950 (1999).
44. J. E. Wolff, T. Trilling, G. Mölenkamp, R. M. Egeler, H. Jürgens, Chemosensitivity of glioma cells in vitro: A meta analysis. *J. Cancer Res. Clin. Oncol.* **125**, 481–486 (1999).
45. T. Ohnishi, I. Tamai, K. Sakanaka, A. Sakata, T. Yamashima, J. Yamashita, A. Tsuji, In vivo and in vitro evidence for ATP-dependency of P-glycoprotein-mediated efflux of doxorubicin at the blood-brain barrier. *Biochem. Pharmacol.* **49**, 1541–1544 (1995).
46. I. Sardi, G. la Marca, S. Cardellicchio, L. Giunti, S. Malvagia, L. Genitori, M. Massimino, M. de Martino, M. G. Giovannini, Pharmacological modulation of blood-brain barrier increases permeability of doxorubicin into the rat brain. *Am. J. Cancer Res.* **3**, 424–432 (2013).
47. P. Hau, K. Fabel, U. Baumgart, P. Rümmele, O. Grauer, A. Bock, C. Dietmaier, W. Dietmaier, J. Dietrich, C. Dudel, F. Hübner, T. Jauch, E. Drechsel, I. Kleiter, C. Wismeth, A. Zellner, A. Brawanski, A. Steinbrecher, J. Marienhagen, U. Bogdahn, Pegylated liposomal doxorubicin-efficacy in patients with recurrent high-grade glioma. *Cancer* **100**, 1199–1207 (2004).
48. H. Von Holst, E. Knochenhauer, H. Blomgren, V. Collins, L. Ehn, M. Lindquist, G. Noren, C. Peterson, Uptake of adriamycin in tumour and surrounding brain tissue in patients with malignant gliomas. *Acta Neurochir.* **104**, 13–16 (1990).
49. T. Siegal, A. Horowitz, A. Gabizon, Doxorubicin encapsulated in sterically stabilized liposomes for the treatment of a brain tumor model: Biodistribution and therapeutic efficacy. *J. Neurosurg.* **83**, 1029–1037 (1995).
50. M. Koukourakis, S. Koukouraki, I. Fezoulidis, N. Kelekis, G. Kyrias, S. Archimandritis, N. Karkavitsas, High intratumoural accumulation of stealth liposomal doxorubicin (Caelyx) in glioblastomas and in metastatic brain tumours. *Br. J. Cancer* **83**, 1281–1286 (2000).
51. U. Bogdahn, T. Jauch, C. Beier, D. Beier, S. Gänβbauer, M. Glas, H. Koch, C. Wismeth, A. Steinbrecher, P. Hau, Combined regimen of temozolomide and liposomal pegylated doxorubicin in glioblastoma—Toxicity and efficacy. *J. Clin. Oncol.* **24**, 11501–11501 (2006).
52. C. P. Beier, C. Schmid, T. Gorlia, C. Kleinletzenberger, D. Beier, O. Grauer, A. Steinbrecher, B. Hirschmann, A. Brawanski, C. Dietmaier, T. Jauch-Worley, O. Kölbl, T. Pietsch, M. Proescholdt, P. Rümmele, A. Muigg, G. Stockhammer, M. Hegi, U. Bogdahn, P. Hau, RNOP-09: Pegylated liposomal doxorubicine and prolonged temozolomide in addition to radiotherapy in newly diagnosed glioblastoma-a phase II study. *BMC Cancer* **9**, 308 (2009).
53. S. L. Chua, M. A. Rosenthal, S. S. Wong, D. M. Ashley, A.-m. Woods, A. Dowling, L. M. Cher, Phase 2 study of temozolomide and Caelyx in patients with recurrent glioblastoma multiforme. *Neuro Oncol.* **6**, 38–43 (2004).
54. S. Ananda, A. K. Nowak, L. Cher, A. Dowling, C. Brown, J. Simes, M. A. Rosenthal, Cooperative Trials Group for Neuro-Oncology (COGNO), Phase 2 trial of temozolomide and pegylated liposomal doxorubicin in the treatment of patients with glioblastoma multiforme following concurrent radiotherapy and chemotherapy. *J. Clin. Neurosci.* **18**, 1444–1448 (2011).
55. P. J. Gaillard, B. M. Kerklaan, P. Aftimos, S. Altintas, A. Jager, W. Gladdines, F. Lonnqvist, P. Soetekouw, H. Verheul, A. Awada, J. Schellens, D. Brandsma, Abstract CT216: Phase I dose escalating study of 2B3-101, glutathione PEGylated liposomal doxorubicin, in patients with solid tumors and brain metastases or recurrent malignant glioma. *Cancer Res.* **74**, CT216 (2014).
56. K. Fabel, J. Dietrich, P. Hau, C. Wismeth, B. Winner, S. Przywara, A. Steinbrecher, W. Ullrich, U. Bogdahn, Long-term stabilization in patients with malignant glioma after treatment with liposomal doxorubicin. *Cancer* **92**, 1936–1942 (2001).
57. P. Chastagner, B. Devictor, B. Geoerger, I. Aerts, P. Leblond, D. Frappaz, J.-C. Gentet, S. Bracard, N. André, Phase I study of non-pegylated liposomal doxorubicin in children with recurrent/refractory high-grade glioma. *Cancer Chemother. Pharmacol.* **76**, 425–432 (2015).
58. J. Cui, X. Wang, J. Li, A. Zhu, Y. Du, W. Zeng, Y. Guo, L. Di, R. Wang, Immune exosomes loading self-assembled nanomicelles traverse the blood–brain barrier for chemo-immunotherapy against glioblastoma. *ACS Nano* **17**, 1464–1484 (2023).
59. J. Xue, Z. Zhao, L. Zhang, L. Xue, S. Shen, Y. Wen, Z. Wei, L. Wang, L. Kong, H. Sun, Q. Ping, R. Mo, C. Zhang, Neutrophil-mediated anticancer drug delivery for suppression of postoperative malignant glioma recurrence. *Nat. Nanotechnol.* **12**, 692–700 (2017).
60. H. Chen, J. Ji, L. Zhang, T. Chen, Y. Zhang, F. Zhang, J. Wang, Y. Ke, Inflammatory responsive neutrophil-like membrane-based drug delivery system for post-surgical glioblastoma therapy. *J. Control. Release* **362**, 479–488 (2023).

61. J. Ji, W. Lian, Y. Zhang, D. Lin, J. Wang, Y. Mo, X. Xu, C. Hou, C. Ma, Y. Zheng, J. Chen, J. Zhong, F. Zhang, Y. Ke, H. Chen, Preoperative administration of a biomimetic platelet nanodrug enhances postoperative drug delivery by bypassing thrombus. *Int. J. Pharm.* **636**, 122851 (2023).
62. F. Winkler, H. S. Venkatesh, M. Amit, T. Batchelor, I. E. Demir, B. Deneen, D. H. Gutmann, S. Hervey-Jumper, T. Kuner, D. Mabbott, M. Platten, A. Rolls, E. K. Sloan, T. C. Wang, W. Wick, V. Venkataramani, M. Monje, Cancer neuroscience: State of the field, emerging directions. *Cell* **186**, 1689–1707 (2023).
63. V. Venkataramani, D. I. Tanev, C. Strahle, A. Studier-Fischer, L. Fankhauser, T. Kessler, C. Körber, M. Kardorff, M. Ratliff, R. Xie, H. Horstmann, M. Messer, S. P. Paik, J. Knabbe, F. Sahm, F. T. Kurz, A. A. Acikgöz, F. Herrmannsdörfer, A. Agarwal, D. E. Bergles, A. Chalmers, H. Miletic, S. Turcan, C. Mawrin, D. Hänggi, H. Liu, W. Wick, F. Winkler, T. Kuner, Glutamatergic synaptic input to glioma cells drives brain tumour progression. *Nature* **573**, 532–538 (2019).
64. G. Shenouda, L. Souhami, K. Petrecca, S. Owen, V. Panet-Raymond, M.-C. Guiot, A. G. Corredor, B. Abdulkarim, A phase 2 trial of neoadjuvant temozolomide followed by hypofractionated accelerated radiation therapy with concurrent and adjuvant temozolomide for patients with glioblastoma. *Int. J. Radiat. Oncol. Biol. Phys.* **97**, 487–494 (2017).
65. Y. Mao, Y. Yao, L.-W. Zhang, Y.-C. Lu, Z.-P. Chen, J.-M. Zhang, S.-T. Qi, C. You, R.-Z. Wang, S.-Y. Yang, X. Zhang, J. S. Wang, J. X. Chen, Q. Y. Yang, H. Shen, Z. Y. Li, X. Wang, W. B. Ma, X. J. Yang, H. N. Zhen, L. F. Zhou, Does early postsurgical temozolomide plus concomitant radiochemotherapy regimen have any benefit in newly-diagnosed glioblastoma patients? A multi-center, randomized, parallel, open-label, phase II clinical trial. *Chin Med J.* **128**, 2751–2758 (2015).
66. H. Jiang, W. Zeng, X. Ren, Y. Cui, M. Li, K. Yang, M. Elbaroody, S. Lin, Super-early initiation of temozolomide prolongs the survival of glioblastoma patients without gross-total resection: A retrospective cohort study. *J. Neurooncol* **144**, 127–135 (2019).
67. J. Perry, A. Chambers, K. Spithoff, N. Laperriere, Gliadel wafers in the treatment of malignant glioma: A systematic review. *Curr. Oncol.* **14**, 189–194 (2007).
68. D. J. Gessler, E. C. Neil, R. Shah, J. Levine, J. Shanks, C. Wilke, M. Reynolds, S. Zhang, C. Özütemiz, M. Gencturk, M. Folkertsma, W. R. Bell, L. Chen, C. Ferreira, K. Dusenbery, C. C. Chen, GammaTile brachytherapy in the treatment of recurrent glioblastomas. *Neurooncol. Adv.* **4**, vdab185 (2022).
69. P. S. Sharp, M. Stylianou, L. M. Arellano, J. C. Neves, A. M. Gravagnuolo, A. Dodd, K. Barr, N. Lozano, T. Kisby, K. Kostarelos, Graphene oxide nanoscale platform enhances the anti-cancer properties of bortezomib in glioblastoma models. *Adv. Healthc. Mater.* **12**, e2201968 (2022).
70. B. R. Dickie, Z. Ahmed, J. Arvidsson, L. C. Bell, D. L. Buckley, C. Debus, A. Fedorov, R. Floca, I. Gutmann, R. A. van der Heijden, P. J. van Houdt, S. Sourbron, M. J. Thrippleton, C. Quarles, I. N. Kompan, on behalf of The Perfusion Study Group of the ISMRM, A community-endorsed open-source lexicon for contrast agent–based perfusion MRI: A consensus guidelines report from the ISMRM Open Science Initiative for Perfusion Imaging (OSIPI). *Magn. Reson. Med.* **91**, 1761–1773 (2024).
71. M. Stylianou, T. Kisby, D. Despotopoulou, H. Parker, A. Thawley, K. Arashvand, N. Lozano, A. S. MacDonald, K. Kostarelos, Engineering the glioblastoma microenvironment using TLR7/8 agonist-complexed graphene oxide nanosheets. *Cell Rep. Phys. Sci.* **6**, 102342 (2025).


**Acknowledgments:** We thank M. Xu, A. Thawley, and K. Arashvand for assistance with in vivo experiments, animal monitoring, tissue processing, and histological preparations. We also acknowledge the Histology Core Facility, Bioimaging Core Facility, Flow Cytometry Core, Electron Microscopy Facility, and the Biological Services Facility at the University of Manchester for technical support and access to equipment. N.L. thanks the ICN2 Nanobioelectronics and Biosensors Group (led by A. Merkoçi) for access to equipment. N.H. thanks M. del Cabo from the Microscopy and X-Ray Diffraction Service at UAB for assistance with sample preparation and microscope data acquisition. **Funding:** This study was supported by the University of Manchester/Medical Research Council (MRC) Confidence in Concept Round 8 (CiC8; to T.K.), an Engineering and Physical Sciences Research Council (EPSRC) 2D-Health Programme grant (EP/P00119X/1, to K.K.), an EPSRC International Centre-to-Centre grant (EP/S030719/1, to K.K. and T.K.), and a Rosetrees Intermediate Project Award (PGS23/100184, to K.K. and T.K.). ICN2 is funded by the CERCA Programme/Generalitat de Catalunya and supported by the Severo Ochoa Centres of Excellence Programme (grant CEX2021-001214-S, funded by MCIU/AEI/10.13039/501100011033). We also acknowledge M. Castro (University of Michigan) for provision of the mGNS cell line, which was derived with support from NIH/National Institute of Neurological Disorders and Stroke (1RO1NS122165-O1 to M. Castro). Funders had no role in study design, data collection, data interpretation, or the decision to submit the work for publication. **Author contributions:** L.F.F. and T.K. performed most of in vivo experiments, including tumor resections and in vivo imaging, developed methodology, conducted data analysis, prepared figures, and wrote the manuscript. C.P. performed tissue staining and imaging, analyzed data, and contributed to figure preparation. L.A.T. performed in vivo experiments, developed flow cytometry methodology, and assisted with data analysis and imaging. B.R.D. contributed to MRI methodology development, experimental design, and data analysis and provided input on data interpretation and figure preparation. Y.S.H. assisted with ex vivo imaging and tissue processing. L.F.F., L.A.T., and N.L. contributed to liposome nanoparticle preparation and characterization. N.H. performed cryo–electron microscopy sample preparation and imaging of liposomes. L.F.F., K.K., and T.K. conceptualized and designed the study. K.K. and T.K. coordinated the study and secured funding. L.F.F., B.R.D., N.L., K.K., and T.K. contributed to manuscript writing. **Competing interests:** The authors declare that they have no competing interests. **Data, code, and materials availability:** All data associated with this study are present in the paper or the Supplementary Materials. All materials used or generated in this study are commercially available or will be supplied upon reasonable request.

Submitted 10 January 2025
Resubmitted 6 February 2026
Accepted 8 June 2026
Published 29 July 2026
10.1126/scitranslmed.adv8761

Science Translational Medicine

# Targeting therapeutic nanoparticles to the glioblastoma resection margin by harnessing postoperative blood-brain barrier disruption

Lorena F. Fernandes, Chariya Peeyatu, Lydia A. Thompson, Ben R. Dickie, Yu Siong Ho, Noelia Hernandez-Lobato, Neus Lozano, Kostas Kostarelos, and Thomas Kisby

*Sci. Transl. Med.* **18** (860), eadv8761. DOI: 10.1126/scitranslmed.adv8761

**Editor's summary**

Standard of care for glioblastoma (GBM) includes maximal safe resection followed by radiotherapy and temozolomide; however, recurrence often occurs, and further treatment is often hindered by the blood-brain barrier (BBB). Here, Fernandes *et al.* evaluated the effect of resection on the BBB and the potential to combine this with nanoparticle therapy. Using mouse models, they show that intravenously delivered liposomes selectively accumulate in the postoperative resection margin and that early postoperative administration of liposomal doxorubicin suppresses tumor recurrence and prolongs mouse survival. This postoperative window of opportunity for blood-brain tumor permeability could change treatment efficacy and warrants consideration in the context of current standard of care. —Dorothy Hallberg







*Science Translational Medicine* (ISSN 1946-6242) is published by the American Association for the Advancement of Science. 1200 New York Avenue NW, Washington, DC 20005. The title *Science Translational Medicine* is a registered trademark of AAAS.

Science Translational Medicine
AAAS

# Supplementary Materials for

## Targeting therapeutic nanoparticles to the glioblastoma resection margin by harnessing postoperative blood-brain barrier disruption

Lorena F. Fernandes *et al.*

Corresponding author: Thomas Kisby, thomas.kisby@manchester.ac.uk;
Kostas Kostarelos, kostas.kostarelos@manchester.ac.uk

*Sci. Transl. Med.* **18**, eadv8761 (2026)
DOI: 10.1126/scitranslmed.adv8761

**The PDF file includes:**



**Other Supplementary Material for this manuscript includes the following:**

# Supplementary Materials and Methods

**Empty liposome (DiI-Lipo/DiD-Lipo) synthesis.** Liposome vesicles were synthesised from the lipids Hydrogenated soy phosphatidylcholine (HSPC; Lipoid), Cholesterol (Fisher Scientific), and 2-distearoyl-sn-glycero-3-phosphoethanolamine-N-[methoxy(polyethylene glycol)-2000] (DSPE-PEG2000; Lipoid) at a HSPC:Chol:DSPE-PEG2000 ratio of 56.3:38.2:5.5 mol %. Empty liposomes were prepared by the thin film hydration method followed by vesicle size calibration as previously described(*31*). Briefly, lipids were dissolved and mixed in a round-bottom flask in a chloroform/methanol mixture (4:1) with the inclusion of the fluorescent probe 1,1'-Dioctadecyl-3,3,3',3'-Tetramethylindocarbocyanine Perchlorate (DiI; Invitrogen, 5 mol %) or 1,1'-Dioctadecyl-3,3,3',3'-Tetramethylindodicarbocyanine, 4-Chlorobenzenesulfonate Salt (DiD; Invitrogen, 1 mol %). The organic solvents were evaporated to produce a lipid film which was stored at 4 ºC overnight, protected from light. Hydration was performed with HBS (20 mM HEPES, 150 mM NaCl, pH 7.4) to a final lipid concentration of 12.5 mM. Extrusion through 800, 200, 100 nm polycarbonate extrusion filters (Whatman; VWR) was performed multiple times (5x:5x:20x) to produce unilamellar liposomes with reduced polydispersity. Free DiI or DiD was removed by passing liposomes through a Sepharose CL-4B column (Merck) equilibrated with HBS (pH 7.4) and the final solution (obtained from fractions 4-6) concentrated with a Vivaspin 6 Polyethersulfone 10000 Da MWCO centrifugal filter to a final concentration of 12.5 mM liposomes before being sterile filtered through a 0.2 µm membrane.

**Doxorubicin-containing liposomes (DOX-Lipo) synthesis.** Doxorubicin was encapsulated in the same liposomal formulation as above (without the fluorescent probe) by following the ammonium sulphate gradient method. The lipid film made of HSPC, Chol, and DSPE-PEG2000 at 56.3:38.2:5.5 molar ratio, was hydrated in 250 mM ammonium sulphate (Merck) at pH 8.5, at 65 ºC for 1h. After 1h stabilization at room temperature, the liposomes were extruded with a LIPEX® liposome extruder (Evonik) at 65 ºC, five times through 800, 400, 200 nm polycarbonate membranes and five more times through 400, 200, 100 nm membranes. Buffer exchange was performed by Sepharose CL-4B (BioRad) size exclusion chromatography using HBS and the fractions containing liposomes were further concentrated using Vivaspin 6 (Sartorius) at 8,000 g, 20 min at 4 ºC. 0.5 mg/ml of doxorubicin hydrochloride (Merck) was added into 12.5 mM liposomes (lipid:doxorubicin weight ratio 1:20) and incubated at 65 ºC for 1.5h. The doxorubicin-containing liposomes were purified using Sepharose CL-4B columns and further concentrated using Vivaspin columns to obtain 12.5 mM liposomes. The final solution was sterile filtered through a 0.2 µm membrane. Doxorubicin encapsulation efficiency resulting of 98% was obtained using 0.1% Triton X-100 to dissolve the liposomes and the doxorubicin fluorescence was quantified using the plate reader SpectraMax® iD3 at ICN2 Nanobioelectronics and Biosensors Group, excitation and emission wavelengths of 480 and 593 nm, respectively, and calculated as: EE% = (after purification+TX – after purification) / (before purification+TX – after purification)*100

**Liposome characterization.** Liposome systems fabricated were characterised using the following techniques:

**Dynamic light scattering and zeta potential measurements**. Liposome size (hydrodynamic diameter) and surface charge (zeta potential) were measured using a Zetasizer Nano ZS (Malvern, Instruments, UK). Samples were diluted 100x with distilled water and 3 independent measurements per sample were recorded, and the data expressed as average ± SD.

**Transmission electron microscopy (TEM).** Empty DiI-labelled liposomes were visualized with transmission electron microscopy (FEI Tecnai 12 BioTwin) at a 1 mM lipid concentration with a Carbon Film Mesh Copper Grid (CF400-Cu, Agar Scientific). Samples were stained with 1% aqueous uranyl acetate solution.

**Cryo-transmission electron microscopy (Cryo-TEM)**. Doxorubicin-containing liposomes were imaged with a Cryo-transmission electron microscopy (CryoTEM) at the Microscopy and X-ray diffraction service at UAB, using a JEOL-2011 transmission electron microscope adapted for cryogenic microscopy, working at a voltage of 200 kV and equipped with CMOS Gatan Rio 16 camera and EDS Oxford Instruments X-max detector.

**Dexamethasone treatments.** To model clinically relevant corticosteroid exposure in glioblastoma patients, dexamethasone was administered at a dose equivalent to 16 mg/day in humans (*32*). Using body surface area scaling (*31*), the corresponding mouse dose was calculated as 0.229 mg/kg × 12.3 ≈ 2.8 mg/kg. Mice received 2.5 mg/kg dexamethasone via intraperitoneal injection once daily from resection through to endpoint, reflecting standard human clinical administration for management of postoperative oedema.

**MRI Parameters**. Quantities, processes and model definitions used to report DCE-MRI acquisition and analysis are OSIPI CAPLEX compliant(*70*). T2-TurboRARE MRI (TR/TE = 3000/35 ms, FOV = 20 x 20 x 7.5 mm, matrix size = 256 x 256 x 20) was performed to define the anatomical position of the tumour or resection margin. Dynamic contrast-enhanced MRI using 3D spoiled gradient echo (TR/TE = 8.0/1.6 ms, flip angle = 12º, FOV = 20 x 20 x 7.5 mm, matrix size = 128 x 128 x 10, temporal resolution = 10.2s, duration = 20 min 28s) was used to measure BBB integrity, by monitoring the increase in DCE-MRI signal intensity caused by leakage of contrast agent from blood into brain tissue. Each mouse was anesthetised using 3% isoflurane in 100% $O_2$, cannulated using a 27G needle attached to a line containing Gd-DOTA contrast agent, and positioned on the MRI bed. Once stable, anaesthesia was reduced to 1.5-2%. Ear and bite bars were used to secure the head. A volume resonator was used for transmission and mouse brain surface coil for reception. After the 18$^{th}$ dynamic frame (3-minute baseline), 0.1 mmol/kg of Gd-DOTA was injected as a bolus using a contrast injector at 1 ml/min. Following completion of MRI, mice were recovered in a heated box and returned to housing.

**MRI Analysis.** Tumour and resection margin regions of interest (ROIs) were delineated manually on T2-TurboRARE images in MRIcron (version 1.0.2). These ROIs were imported into Matlab (Mathworks, version 2023a) where they were down-sampled to the grid size of the DCE-MRI data. Prior to applying to the DCE-MRI data, a map of DCE-MRI area under the curve (AUC) was generated from each dataset. First, DCE-MRI timeseries were coaligned to remove any motion between frames. Second, the DCE-MRI signal was converted to signal enhancement by subtracting the baseline signal. Third, the signal was summed across all timepoints to calculate the AUC. Once the AUC maps were calculated, the tumour or resection ROI was applied to extract the mean AUC. To calculate the AUC at different distances from the resection or tumour margin, the original ROI was dilated by 1 pixel in all direction, then subtracted from the original ROI leaving a layer of ROI pixels just outside the original ROI. Any part of this layer residing outside of the brain tissue was excluded. The mean AUC for this layer was then extracted, and the process repeated a further 5 times, providing a profile of AUC outwards 1mm from the resection or tumour edge.

**Tissue processing.** Mice were anesthetized with 2.5% isoflurane and euthanised by cardiac perfusion with PBS containing 2 mM EDTA to fully remove blood and circulating liposomes. Brains were carefully dissected and fixed overnight at 4 ºC, followed by cryoprotection in 30% (w/v) sucrose in PBS for at least 24 h. Tissue was then snap-frozen in pre-cooled isopentane (−40 °C), and coronal brain sections (20 µm thickness) were prepared using a cryostat (Leica CM1950, Leica Biosystems).

**Immunofluorescence staining and analysis.** For immunofluorescence analysis, 20-µm cryosections were air-dried and fixed in ice-cold acetone for 10 min. Sections were washed in PBS and blocked for 1 h in PBS containing 1% bovine serum albumin (BSA), 5% goat serum, and 0.2% Triton X-100 to reduce non-specific binding. Primary antibodies were diluted in blocking buffer and incubated with sections overnight at 4 ºC. The following primary antibodies were used: rabbit anti-IBA1 (1:500; Fujifilm Wako, 019-19741), chicken anti-GFAP (1:1000; Millipore, AB5541), rat anti-CD31 (1:100; BD Biosciences, 550274), mouse anti-Caveolin-1 (CAV1; 1:100; BD Biosciences, 610407), and rabbit anti-NeuN (1:100; Abcam, EPR12763). After washing in PBS, sections were incubated with species-appropriate secondary antibodies for 1 h at room temperature in the dark. Secondary antibodies included Alexa Fluor™ 647-conjugated goat anti-rabbit IgG (1:400; Invitrogen, A21244), Alexa Fluor™ 488-conjugated goat anti-chicken IgY (1:500; Invitrogen, A11039), Alexa Fluor™ 647-conjugated goat anti-rat IgG (1:200; Invitrogen, A21247), and Alexa Fluor™ 488-conjugated goat anti-mouse IgG (1:200; Invitrogen, A11001). Endogenous GFP fluorescence from mGNS tumour cells and doxorubicin autofluorescence were analysed in selected experiments. Nuclei were counterstained with DAPI (1:10,000; Merck). Sections were washed and mounted using ProLong™ Gold Antifade Mountant (Thermo Fisher Scientific) before coverslipping. Fluorescence images were acquired using a 3DHISTECH Panoramic 250 slide scanner, a Zeiss AxioImager Z1 epifluorescence microscope, or a Leica SP8 WLL inverted confocal microscope. Image processing and quantitative analyses were performed using ImageJ (FIJI).

For co-localisation analysis, maximum-intensity Z-projections were generated from confocal image stacks to reconstruct blood vessels in two dimensions following staining with CD31/CAV1. Dual-channel images were converted to RGB format, and co-localisation was quantified using a colour-thresholding approach. Overlapping signal areas were defined as co-localised regions and expressed as a percentage of total signal area.

For internalisation analysis, cell populations were manually quantified using the ImageJ Cell Counter plugin based on orthogonal inspection of individual Z-slices from confocal image stacks. Internalised DiI-labelled liposomes or doxorubicin were quantified per field of view. Cancer cells were defined as $GFP^+$ $IBA1^-$, macrophages/microglia as $IBA1^+$, neurons as $NeuN^+$, and astrocytes as $GFAP^+$. Data were expressed as the proportion of internalised DiI-liposomes or doxorubicin-positive nuclei within each cell population relative to the total number of detected DiI-liposomes or doxorubicin-positive nuclei across all cell populations.

**Flow cytometric analysis of liposome cellular interactions.** Flow cytometry was performed as previously described(*71*). Animals were perfused via cardiac perfusion with 20 mL of perfusion buffer (2 mM EDTA in PBS). Tumour-bearing hemispheres were dissected, diced with a sterile single-edged blade, and transferred into non-culture-treated 12-well plates (Corning). Each sample was incubated with 1 mL Accutase (Merck) at 37°C for 25 min. Digested tissue was passed through a 100-µm cell strainer using a 10 mL syringe plunger and flow buffer (PBS + 2 mM EDTA, 2% FBS). The flow-through was centrifuged at 300 × g for 7 min at 8 ºC. Cell pellets were resuspended in 35% Percoll (Merck), and 70% Percoll was carefully layered beneath using a 19-gauge needle. Finally, 1 mL of PBS was added on top to form three clearly defined layers. Gradients were centrifuged at 650 × g for 15 min at 20 ºC (acceleration 4, deceleration 1). The top cloudy (fat) layer was discarded, and the transparent, cell-containing layer was collected, with erythrocyte-containing pellet discarded. Cells were washed with flow buffer and centrifuged at 300 × g for 7 min at 8 ºC. Cell pellets were resuspended in flow buffer at 5 × 10^6 cells/mL and transferred to 96-well V-bottom plates (ThermoFisher). Plates were centrifuged at 300 × g for 5 min at 8 ºC, and the supernatant was discarded. Live/dead staining was performed by adding 10 µL of Zombie UV (1:2,000; BioLegend) to each well, followed by incubation in the dark at room temperature for 15 min. Fluorophore-conjugated antibodies (BD Horizon™ BUV805 Rat Anti-Mouse CD45, BD Biosciences; Brilliant Violet 605™ Anti-Mouse/Human CD11b, BioLegend) were diluted in flow buffer and added to the cells, which were incubated at 4°C in darkness for 30 min. Cells were washed twice by adding 50 µL flow buffer, centrifuging at 500 × g for 3 min at 8 ºC, and discarding the supernatant. Cells were fixed in 1% PFA for 10 min at room temperature, washed twice with flow buffer, and finally resuspended in 100 µL flow buffer. Fluorescence was detected using a BD LSRFortessa SORP and analysed with FlowJo (version 11). Fluorescence minus one (FMO) controls were applied for CD45, CD11b, GFP-labelled tumour cells (non-tumour bearing mice), and DiD-liposomes (vehicle control) to establish gating.

**Doxorubicin distribution.** GL261-luc or mGNS bearing mice were treated with doxorubicin-containing liposomes (5 mg/kg) or free doxorubicin (5 mg/kg) intravenously at a single dose 15’ or 48h after resection surgery. 24h or 7 days after liposome treatments mice were anesthetized with 2.5% isoflurane and culled by cardiac perfusion with 2mM EDTA in PBS. Following tissue sectioning, doxorubicin was visualized using its intrinsic fluorescence (excitation 470 nm; emission 595 nm), with a Leica SP8 inverted WLL confocal microscope. Fluorescent doxorubicin was measured by mean grey value on single doxorubicin channel from Z-stack 2D images. The threshold of greyscale image was applied to subtract non-specific background (same threshold for all analysed images).

**Histological evaluation of tumour growth.** Tumour growth was assessed by haematoxylin and eosin (H&E) staining of brain sections. Cryosections were air-dried for 15 min at room temperature and fixed in absolute ethanol for 2 min. Slides were washed once in PBS for 5 min and stained with haematoxylin for 1 min, followed by two washes in distilled water for 3 min each. Sections were then differentiated in 70% ethanol for 3 min and counterstained with eosin (1% eosin in 95% ethanol) for approximately 40 s. Slides were dehydrated through three washes in 100% ethanol (3 min each), cleared in two changes of xylene (2 min each), and mounted using DPX mounting medium. Slides were allowed to dry overnight at room temperature. Whole-slide images were acquired using a Panoramic 250 slide scanner (3DHISTECH) and analysed with 3DHISTECH Case Viewer software (version 2.6). Tumour diameter was measured in each section to identify the section containing the maximal tumour area. Tumour width (W) and height (H) were subsequently measured in this section, and tumour volume was estimated using the formula: $V = (W^2 \times H) / 2$.

**Blood analysis.** Blood samples were collected into K2EDTA tubes (BD Biosciences) and centrifuged at 1,300 × g for 12 min at 4 ºC to obtain cell-free plasma. Plasma albumin and alanine aminotransferase (ALT) levels were measured by the Royal Veterinary College (London, UK) using validated veterinary clinical assays. Cytokine analysis was performed using murine TNF-α and IL-6 ELISA-MAX™ kits (BioLegend) according to the manufacturer's instructions.

# Supplementary Figures

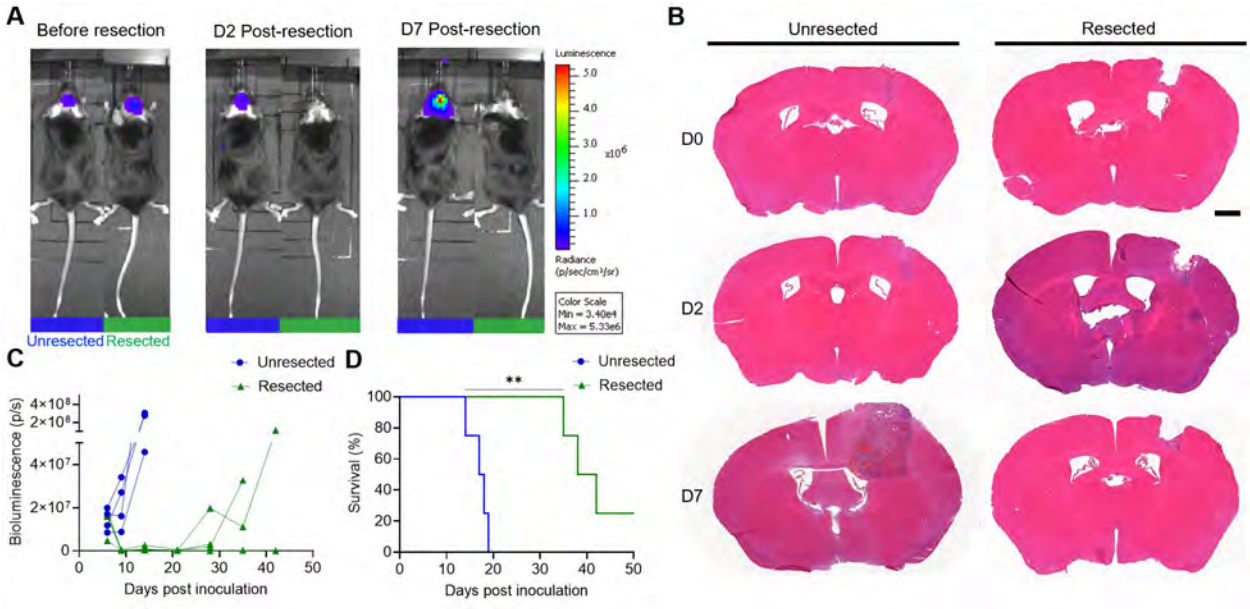


**Fig. S1. Establishment and characterization of a glioblastoma resection/recurrence model.**
(**A**) Longitudinal *in vivo* bioluminescence imaging of GL261 orthotopic tumours acquired 1 day before surgical resection (day 6 post-inoculation) and 2 or 7 days after resection (days 9 and 14 post-inoculation). Tumour resection was performed via craniotomy followed by vacuum aspiration. (**B**) Representative H&E-stained brain sections from unresected and resected animals collected on days 0, 2, and 7 post-resection (corresponding to days 7, 9, and 14 of tumour growth; n = 4). Scale bar = 1000 µm. (**C**) Quantification of tumour bioluminescence signal over time, expressed as total flux (photons/s) (n = 4). (**D**) Kaplan–Meier survival curves (humane endpoint) for mice with or without GL261 tumour resection (n = 4). P values were determined using the log-rank (Mantel–Cox) test (**p < 0.01).

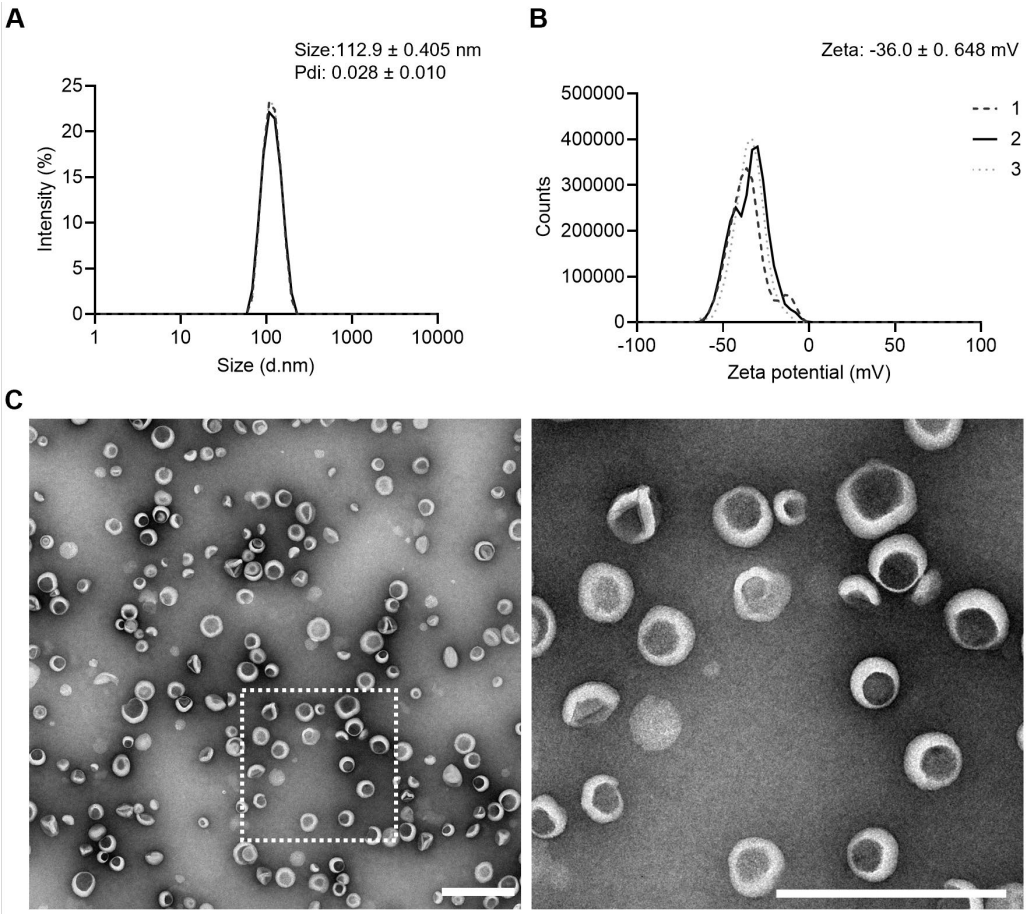


**Fig. S2. Characterization of empty DiI-labelled liposomes.** (**A**) Dynamic light scattering (DLS) analysis of liposome size distribution and (**B**) electrophoretic light scattering (ELS) measurements of zeta potential for empty DiI-labelled liposomes composed of HSPC:Chol:DSPE-PEG2000. Data are presented as mean ± SD from three independent measurements. (**C**) Representative transmission electron micrographs (TEM) of DiI-labelled liposomes. Scale bar = 500 nm.

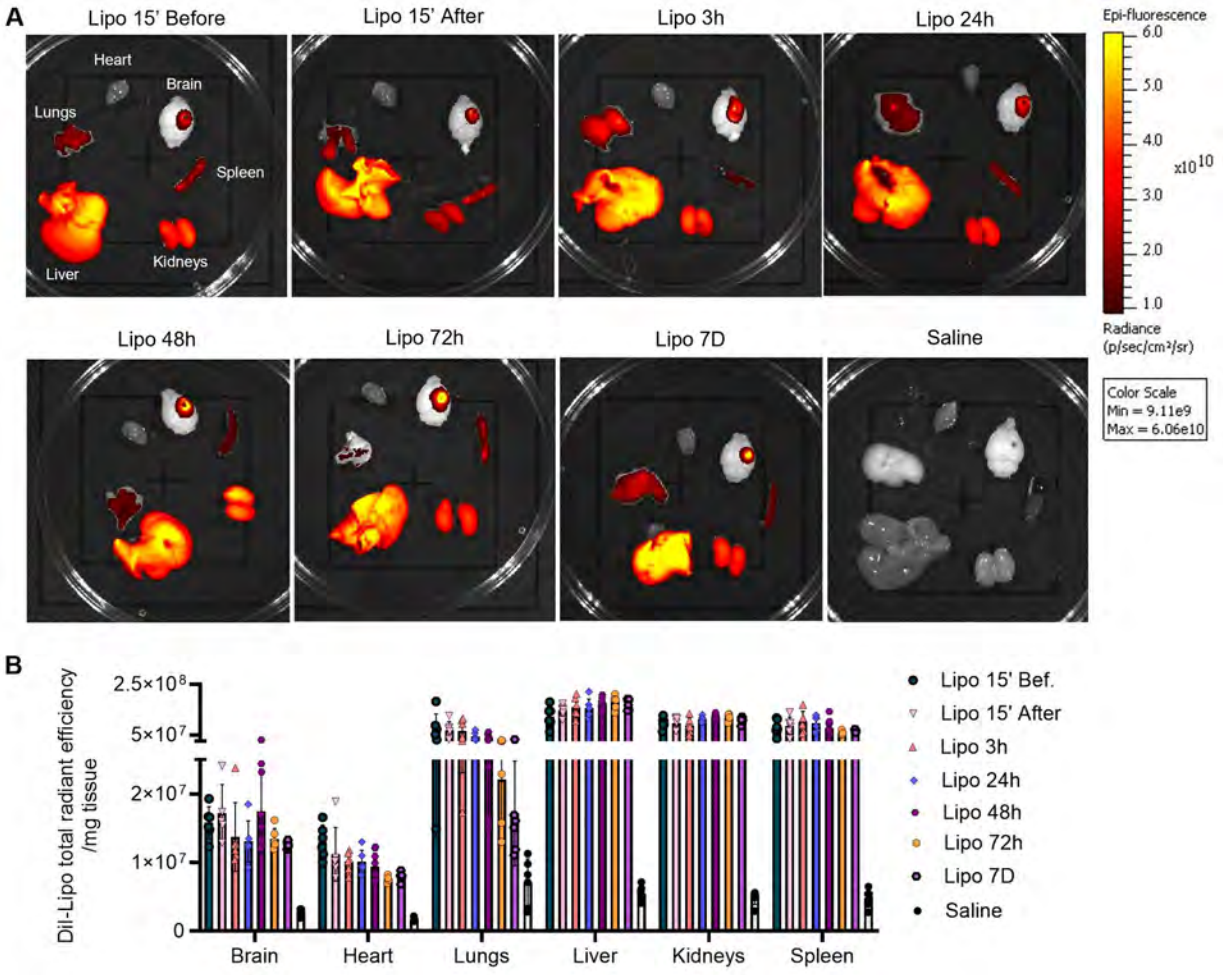


**Fig. S3. Biodistribution of intravenous empty DiI-liposomes injected at different timepoints after surgical resection**. (**A**) Representative *ex vivo* fluorescence images of perfused organs (liver, lungs, heart, brain, spleen, and kidneys) acquired 24 h after liposome injection at the indicated post-resection timepoints. (**B**) Quantification of liposome fluorescence in each organ, expressed as total radiant efficiency (n=6–12 per group). Data are presented as mean ± SD.

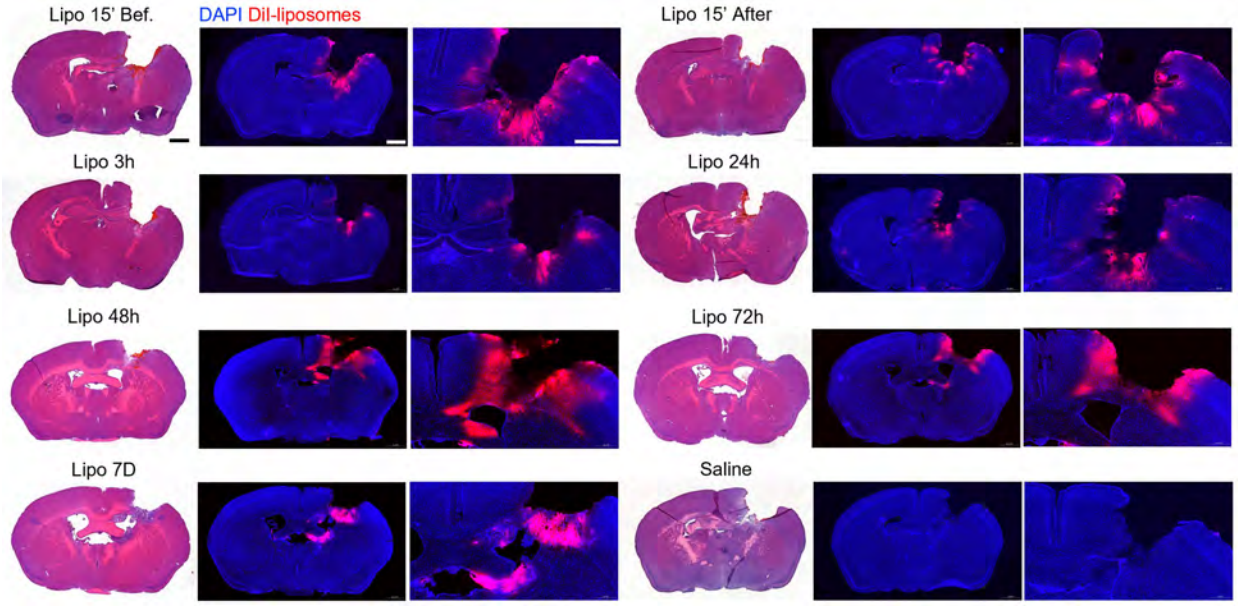


**Fig. S4. Selective accumulation of liposomes around the resection margin.** H&E staining and corresponding representative fluorescence microscopy images of brain sections collected 24 h after a single intravenous injection of DiI-labelled liposomes at the indicated post-resection timepoints. Scale bars = 1000 µm.

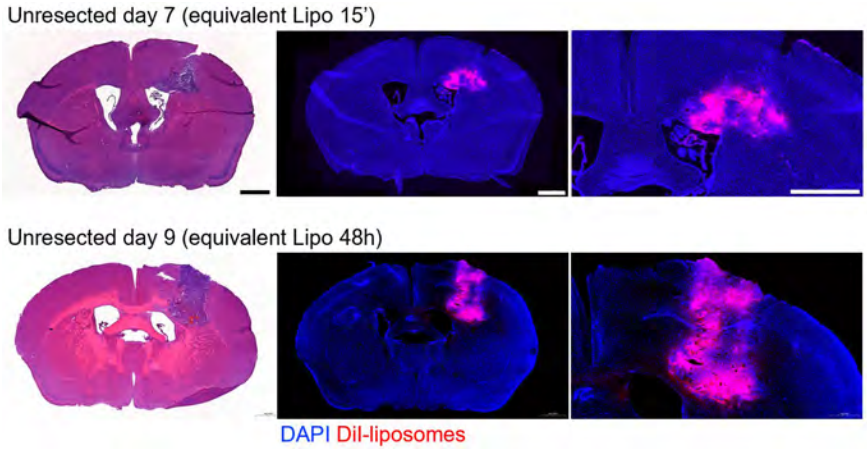


**Fig. S5. Tumour accumulation of empty DiI-liposomes in the brain of unresected groups.** Representative H&E-stained and fluorescence microscopy images showing the distribution of DiI-labelled liposomes in perfused brain sections from GL261 tumour-bearing mice following intravenous injection at the indicated timepoints. Brains were collected 24 h after injection. Scale bars = 1000 μm.

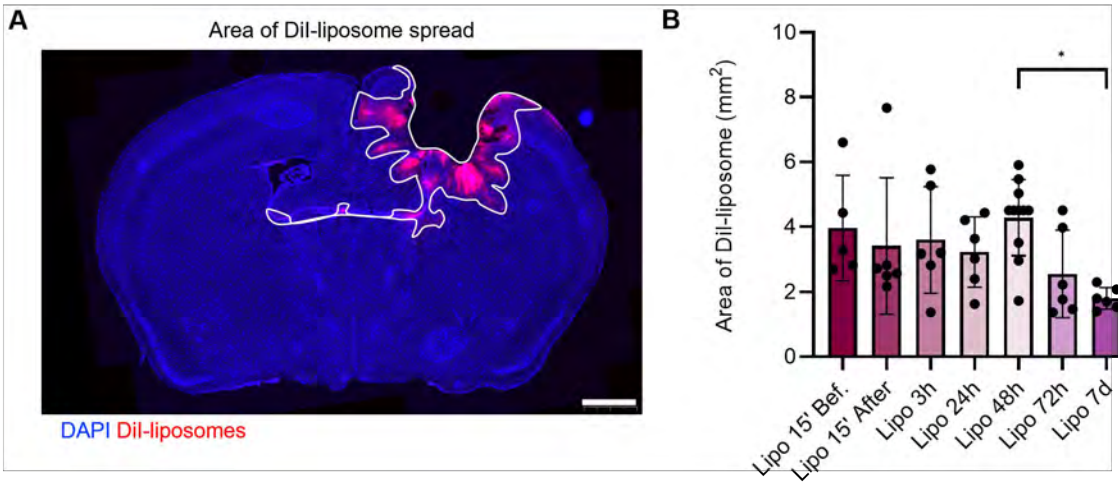


**Fig. S6. Quantification of the area of DiI-liposomes distribution around the resection margin.** (**A**) Schematic illustrating the analysis used to quantify the spatial distribution of DiI-labelled liposomes in brain sections. Mice received a single intravenous injection of DiI-liposomes either 15 min (15') before resection, 15', 3 h, 24 h, 48 h, 72 h, or 7 days after resection surgery. Brain sections were analysed 24 h after liposome injection for all groups. (**B**) Quantification of the area of DiI-liposome spread surrounding the resection margin (five replicate images per mouse; n = 6–12 mice per group). Data are presented as mean ± SD. *P* values were obtained using one-way ANOVA followed by Tukey's multiple comparison test (*$p < 0.05$).

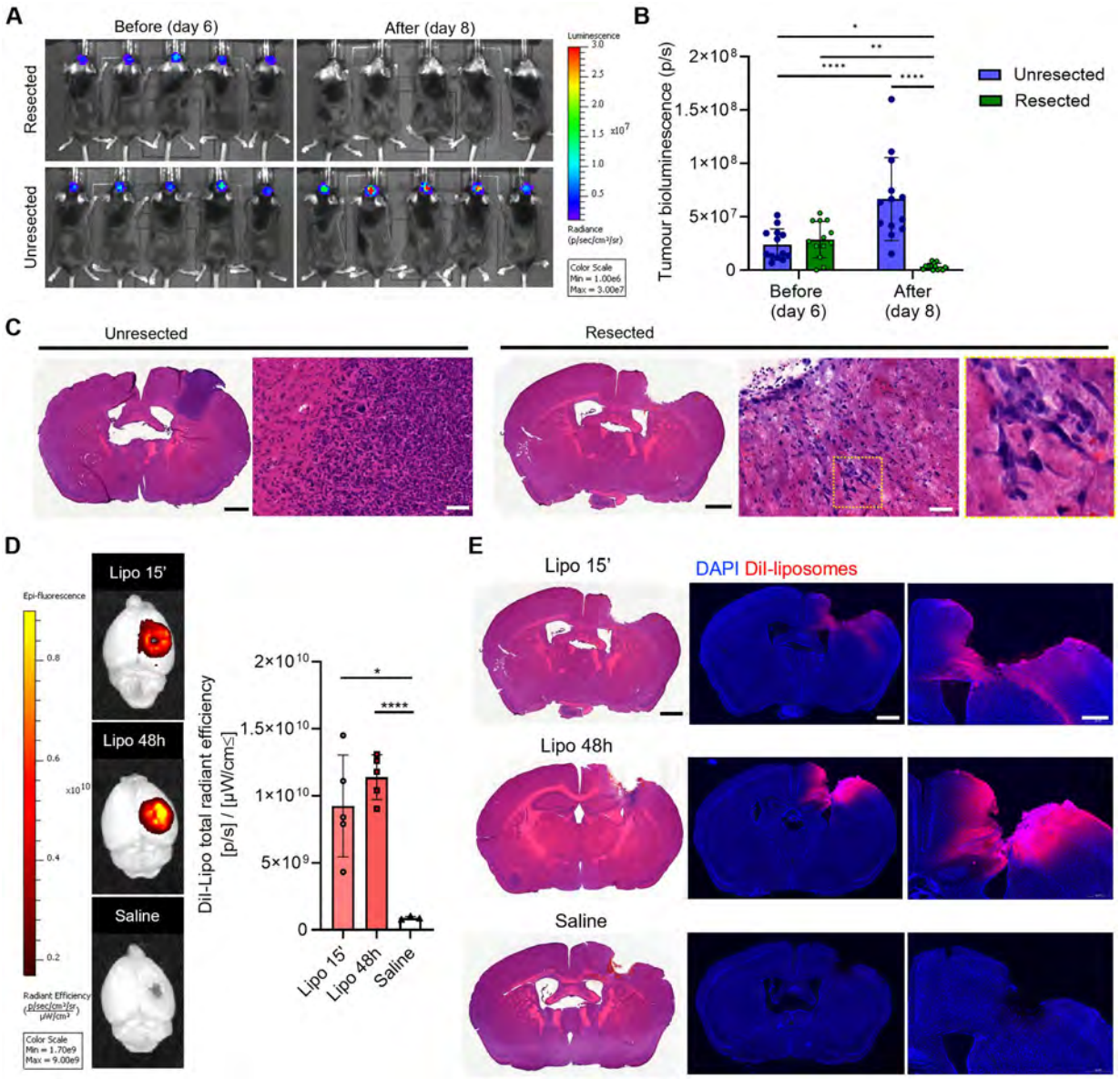


**Fig. S7. Validation of DiI-liposome accumulation in an invasive murine glioma neurosphere (mGNS) based glioma resection model.** (**A**) Longitudinal *in vivo* bioluminescence imaging of mGNS ($NRAS^{G12V}$;shTP53-GFP;shATRX;luciferase) tumours acquired 1 day before resection (day 6 post-inoculation) and 2 days after resection (day 9 post-inoculation). (**B**) Quantification of total tumour bioluminescence (photons/s) over time for unresected and resected groups (n = 13). Data are presented as mean ± SD. *P* values were obtained using two-way ANOVA followed by Tukey's multiple comparison test (*$p < 0.05$, **$p < 0.01$, ****$p < 0.0001$). (**C**) Representative H&E-stained brain sections from unresected and resected animals collected on day 1 post-resection (day 8 post-inoculation; n = 5), showing invasive, sparsely distributed residual tumour cells at the resection margin. Scale bars = 1000 µm (overview) and 50 µm (inset). (**D**) Representative *ex vivo* fluorescence images of perfused brains acquired 24 h after intravenous DiI-liposome injection, with corresponding quantification of brain liposome fluorescence expressed as total radiant efficiency (n = 3–5 per group). Data are presented as mean ± SD. *P* values were obtained using one-way ANOVA followed by Tukey's multiple comparison test (*$p < 0.05$, ****$p < 0.0001$). (**E**) H&E staining and corresponding representative fluorescence microscopy images of brain sections collected 24 h after a single intravenous injection of DiI-labelled liposomes at the identified peak post-resection accumulation timepoints. Scale bars = 1000 µm.

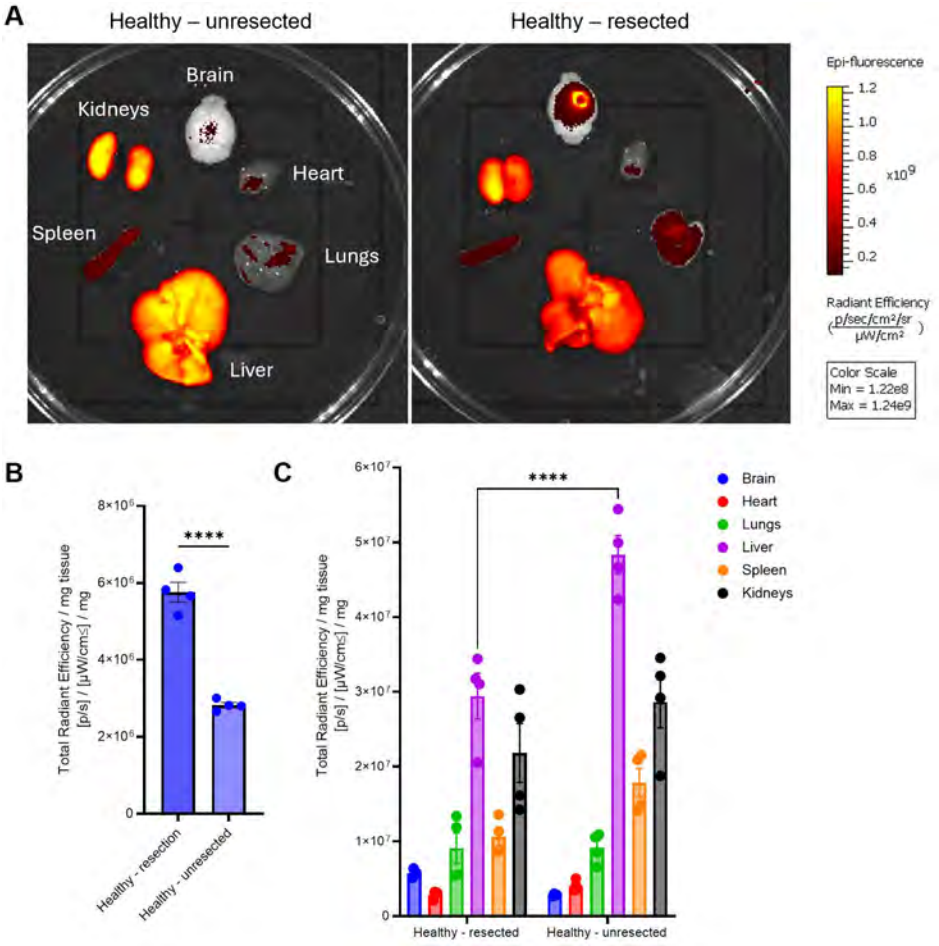


**Fig. S8. Surgical resection alters organ and brain liposome biodistribution in healthy, non–tumour-bearing animals.** (**A**) Representative *ex vivo* fluorescence images of perfused organs (spleen, kidneys, brain, heart, lungs and liver) acquired 24 h after intravenous liposome injection administered 48 h following resection of healthy (non–tumour-bearing) brain tissue, compared with unresected control animals. (**B**) Quantification of liposome fluorescence in brain tissue, expressed as total radiant efficiency per mg of tissue (n = 4 per group), showing increased brain accumulation following resection surgery. Data are presented as mean ± SEM. *P* values were determined using Student's t-test (****$p < 0.0001$). (**C**) Quantification of liposome fluorescence in peripheral organs, expressed as total radiant efficiency per mg of tissue (n = 4 per group), indicating a resection-driven shift in systemic biodistribution. Data are presented as mean ± SEM. *P* values were determined using two-way ANOVA followed by Tukey's multiple comparison test (****$p < 0.0001$).

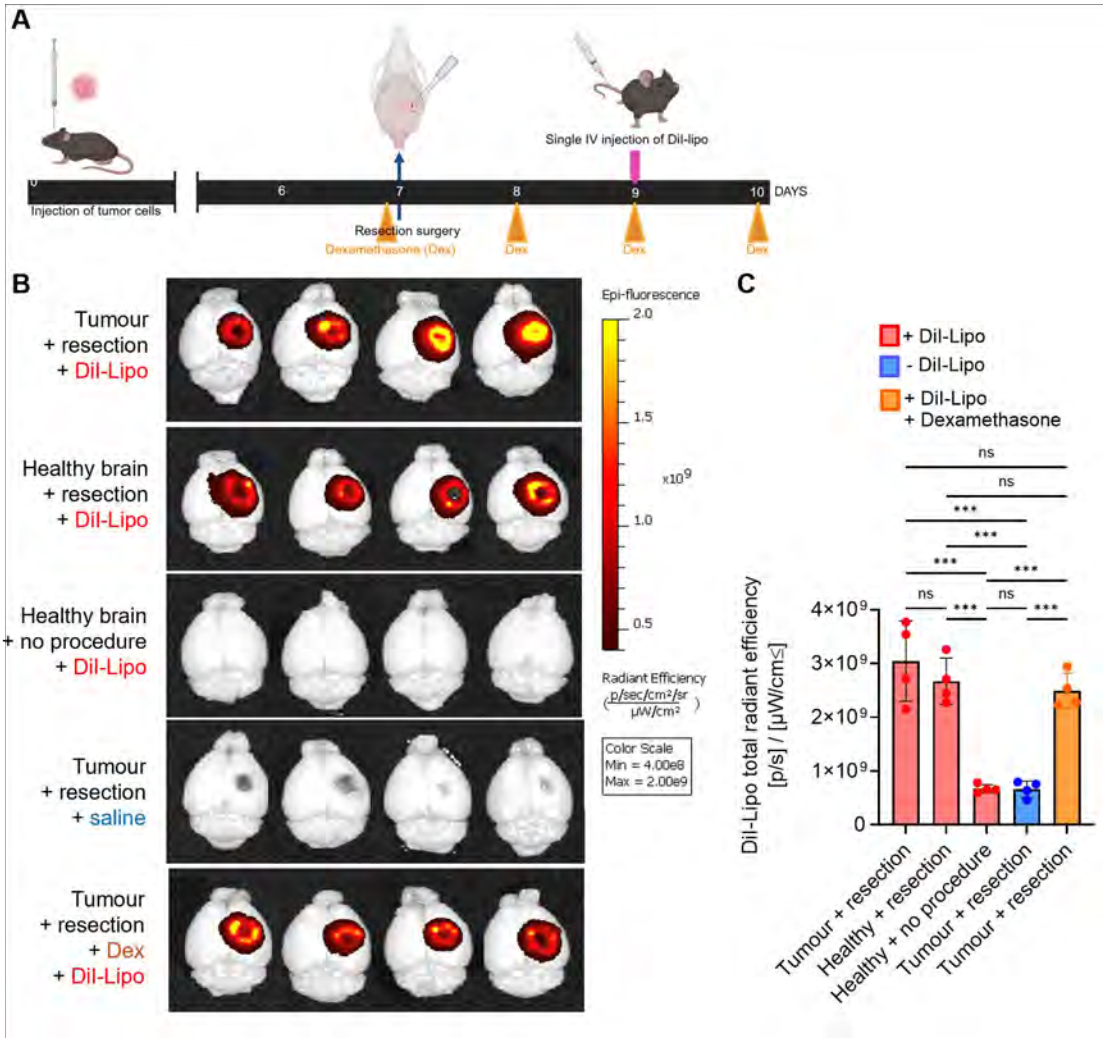


**Fig. S9. Steroid treatment does not alter resection-enabled liposome accumulation in the brain.** (**A**) Experimental schematic. Mice bearing GL261 tumours, or naïve control mice, underwent surgical resection 7 days after tumour inoculation (where applicable). Animals received a clinically aligned regimen of peri-, and postoperative dexamethasone (2.5 mg/kg) on days 7, 8, 9, and 10 post-inoculation. DiI-labelled liposome nanoparticles were administered intravenously on day 9 (48 h after resection), and animals were perfused with brains collected 24 h later for analysis. (**B**) *Ex vivo* fluorescence images of perfused brains showing DiI-liposome accumulation at the resection margin in surgically treated animals, irrespective of dexamethasone treatment (n = 4). (**C**) Quantification of brain DiI fluorescence expressed as total radiant efficiency (n = 4). Data are presented as mean ± SD. *P* values were determined using one-way ANOVA followed by Tukey's multiple comparison test (***$p < 0.001$; *ns*, not significant).

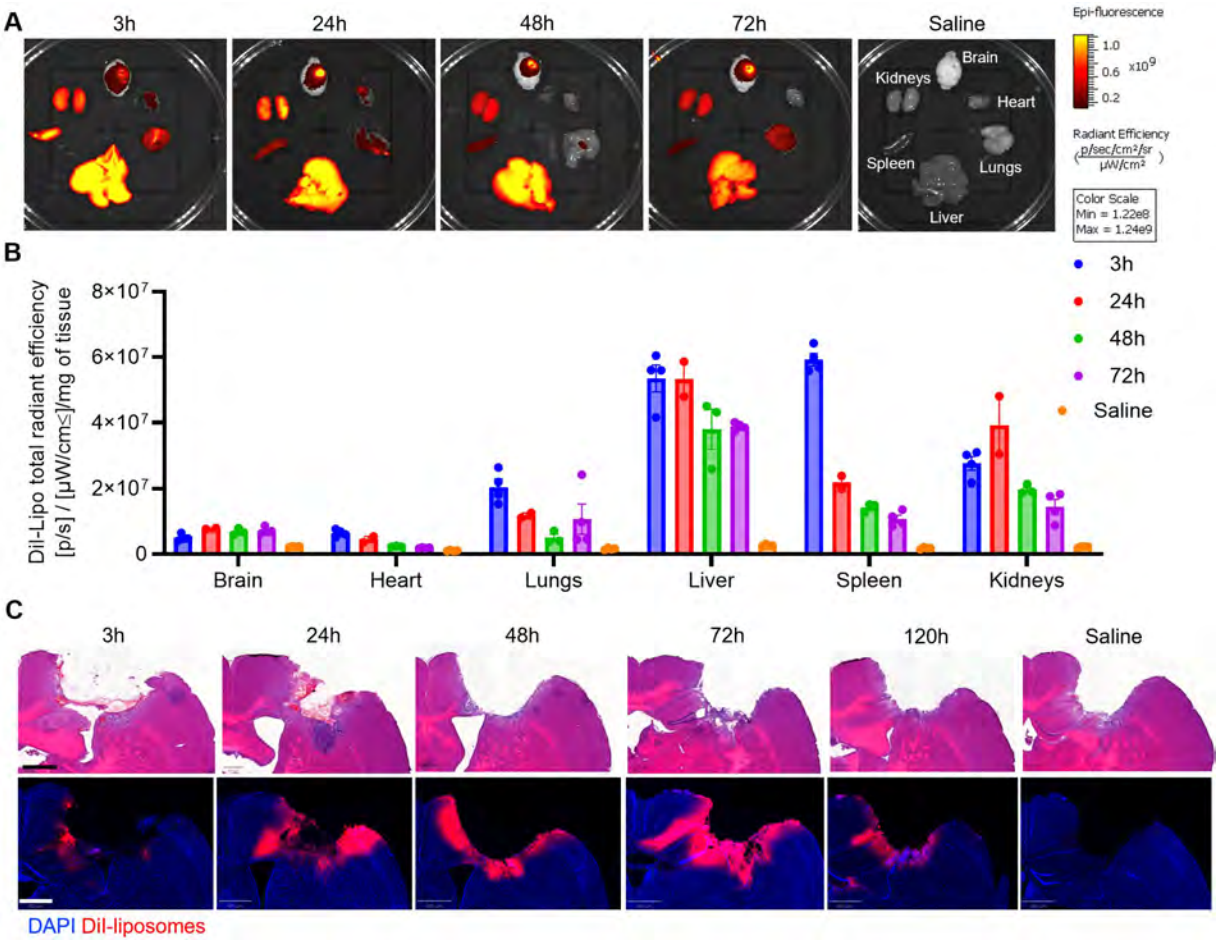


**Fig. S10. Prolonged accumulation of DiI-liposomes at the glioma resection margin.** (**A**) Representative *ex vivo* fluorescence images of perfused organs (spleen, kidneys, brain, heart, lungs, and liver) acquired 3 h, 24 h, 48 h, and 72 h after intravenous liposome injection administered 48 h following resection of GL261 orthotopic tumours. (**B**) Quantification of liposome fluorescence in peripheral organs at each timepoint, expressed as total radiant efficiency per mg of tissue (n = 3–4 per group). Data are presented as mean ± SEM. (**C**) H&E staining and corresponding representative fluorescence microscopy images of brain sections collected 3 h, 24 h, 48 h, 72 h, and 120 h after a single intravenous injection of DiI-labelled liposomes administered 48 h post-resection. Scale bars = 1000 µm.

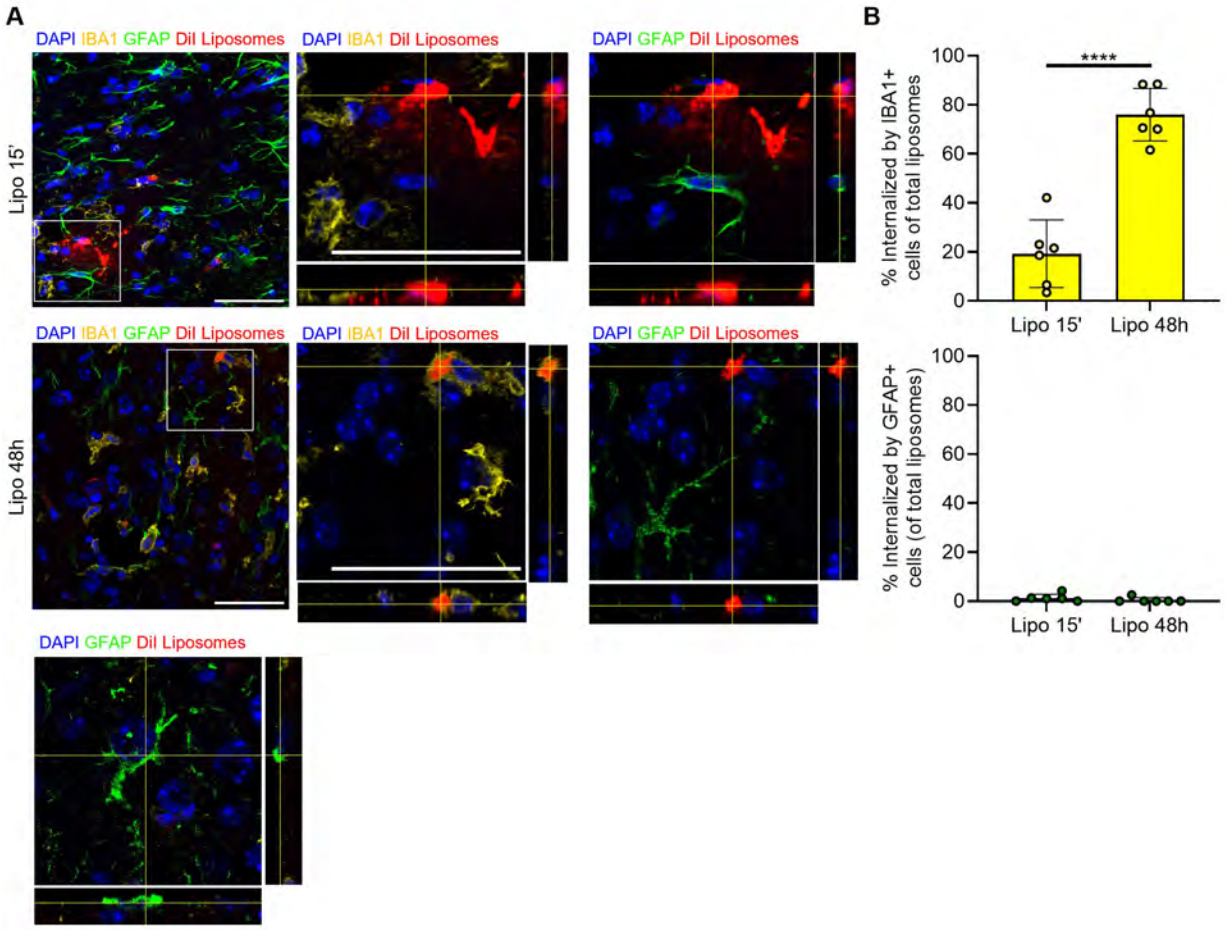


**Fig. S11. Preferential internalisation of liposomes by macrophages/microglia versus astrocytes in the resection margin.** (**A**) Representative confocal micrographs showing IBA1-positive macrophages/microglia, GFAP-positive astrocytes, and DiI-labelled liposomes in mice injected intravenously either 15 min or 48 h after GL261 tumour resection and analysed 24 h after injection. Scale bars = 50 µm. (**B**) Quantification of internalised DiI-liposomes within IBA1-positive or GFAP-positive cells, expressed as a percentage of total detected liposomes (four fields of view per mouse; n = 6 mice). Data are presented as mean ± SD. *P* values were determined using Student's t-test (****$p < 0.0001$).

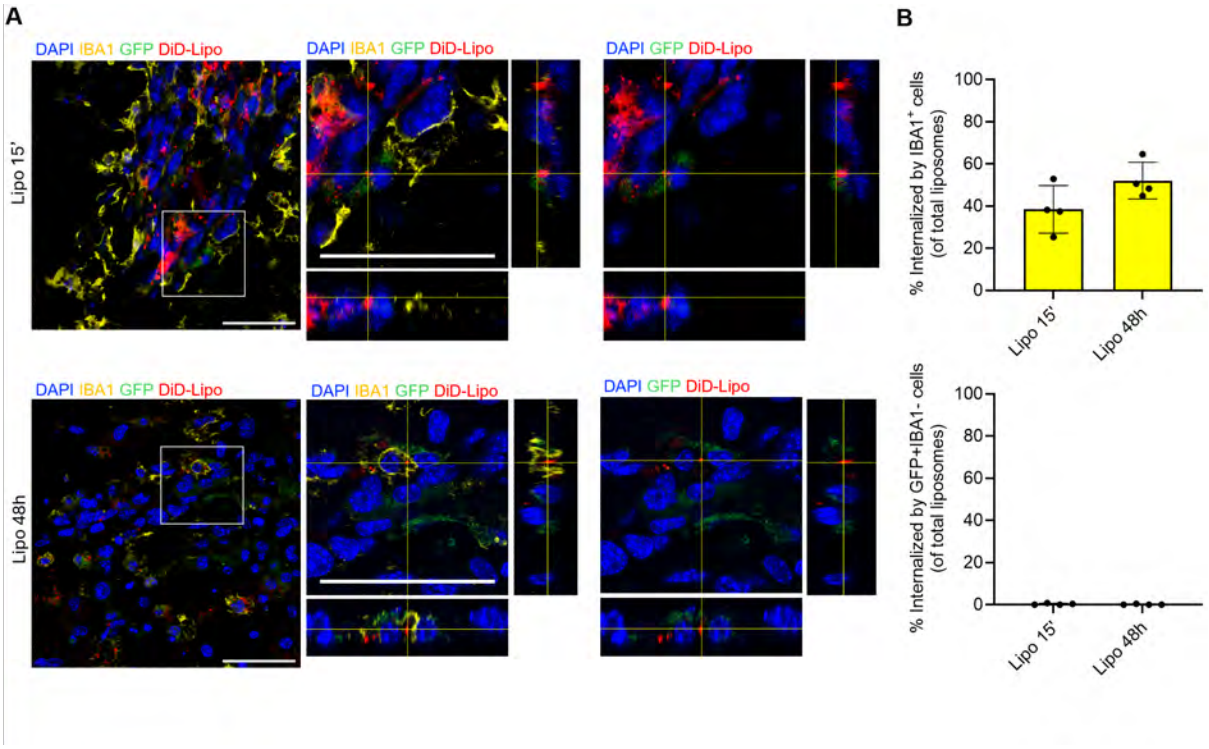


**Fig. S12. Preferential internalisation of liposomes by macrophages/microglia versus tumour cells in the resection margin in the more infiltrative mGNS model.** (**A**) Representative confocal micrographs showing IBA1-positive macrophages/microglia, GFP-labelled tumour cells (*mGNS;* NRAS$^{G12V}$;shTP53-GFP;shATRX;luciferase), and DiD-labelled liposomes in mice injected intravenously either 15 min or 48 h after mGNS tumour resection and analysed 24 h after injection. Scale bars = 50 µm. (**B**) Quantification of internalised DiD-liposomes within IBA1-positive or GFP-positive/IBA1-negative cells, expressed as a percentage of total detected liposomes (three fields of view per mouse; n = 4 mice). Data are presented as mean ± SD.

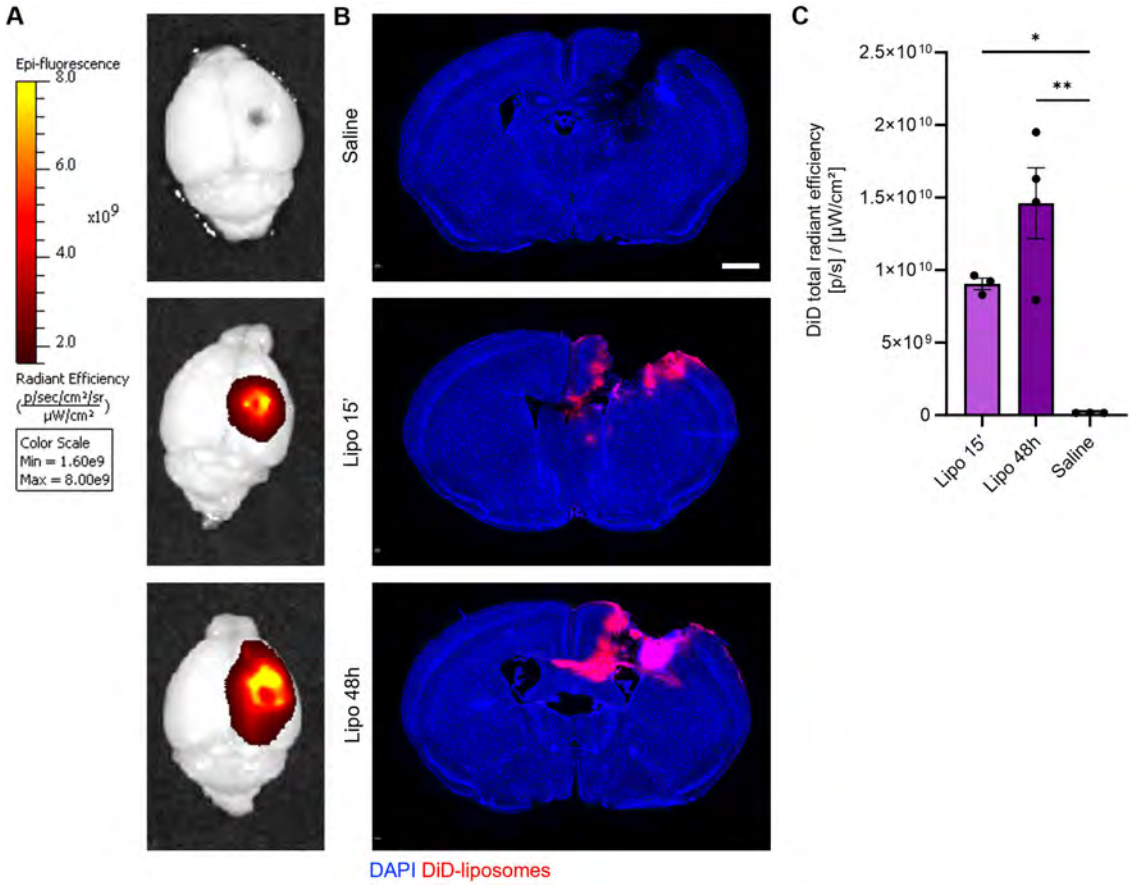


**Fig. S13. Resection margin accumulation of DiD labelled liposomes.** (**A**) Representative *ex vivo* fluorescence images of perfused brains acquired 24 h after liposome injection, showing DiD-liposome distribution around the surgical site at the indicated injection timepoints. (**B**) Representative fluorescence microscopy images of brain sections collected 24 h after intravenous DiI-liposome injection at the identified peak accumulation timepoints. Scale bar = 1000 µm. (**C**) Quantification of brain DiD-liposome fluorescence expressed as total radiant efficiency (n = 3-4 per group). Data are presented as mean ± SEM. *P* values were obtained using one-way ANOVA followed by Tukey's multiple comparison test (*$p$ < 0.05, **$p$ < 0.01).

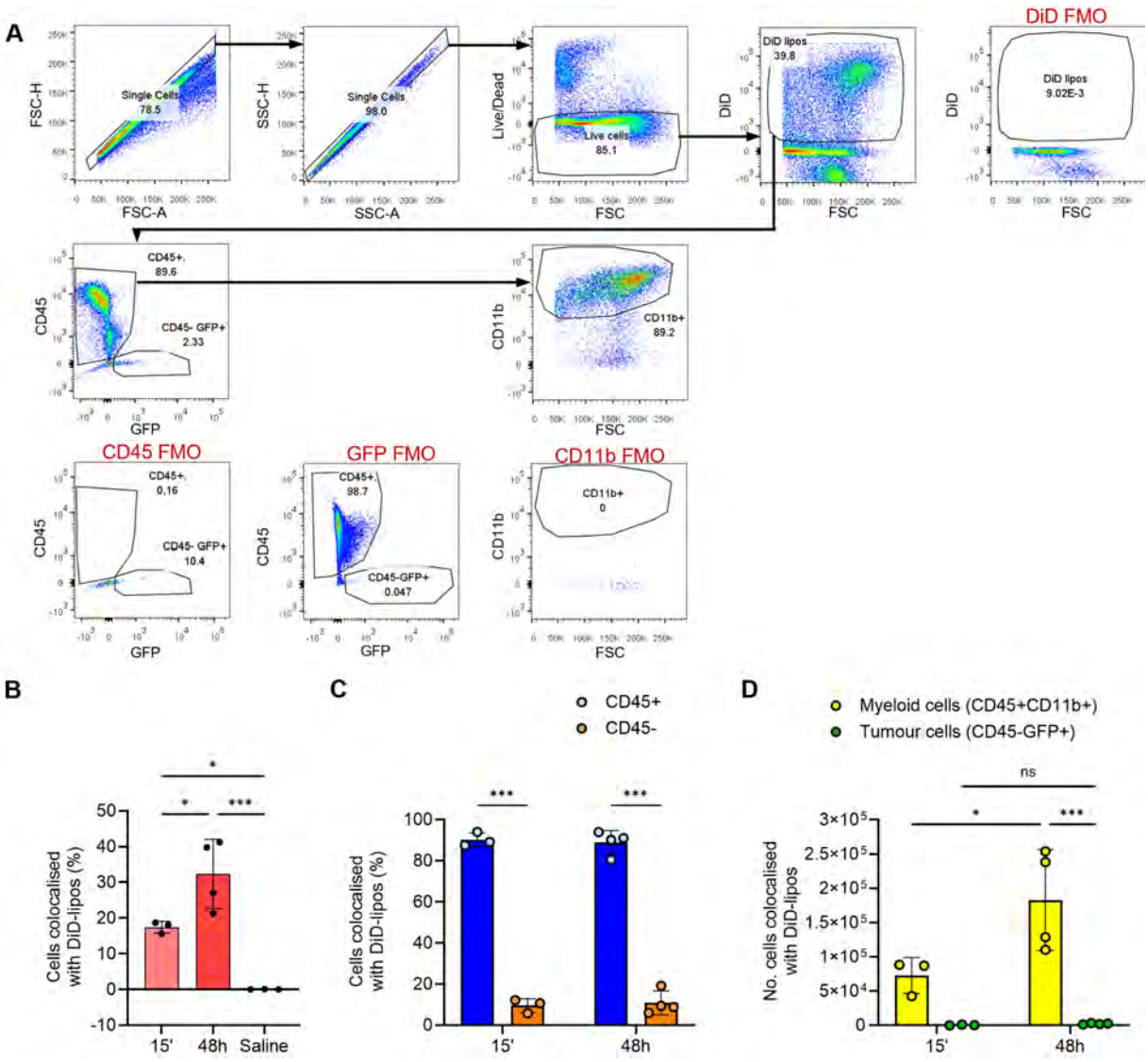


**Fig. S14. Flow cytometric analysis of liposome cellular interactions in the resection margin.** (**A**) Gating strategy for identification of DiD-positive live, single cells and determination of cell populations within the DiD-positive fraction, including fluorescence minus one (FMO) controls used for gate placement. Analysis was performed on the surgically treated hemisphere of mice receiving intravenous DiD-labelled liposomes either 15 min or 48 h after resection surgery. Brains were isolated and analysed 24 h after injection. (**B**) Percentage of DiD-positive live cells in the surgically treated hemisphere. Data are presented as mean ± SD. *P* values were determined using one-way ANOVA followed by Tukey's multiple comparison test (**p* < 0.05, ****p* < 0.001). (**C**) Proportion of $CD45^+$ or $CD45^-$ cells within the DiD-positive live cell population. Data are presented as mean ± SD. *P* values were determined using two-way ANOVA followed by Tukey's multiple comparison test (****p* < 0.001). (**D**) Absolute number of $CD45^+CD11b^+$ myeloid cells or $CD45^-GFP^+$ tumour cells within the DiD-positive live cell population. Data are presented as mean ± SD. *P* values were determined using two-way ANOVA followed by Tukey's multiple comparison test (**p* < 0.05, *****p* < 0.0001; *ns*, not significant).

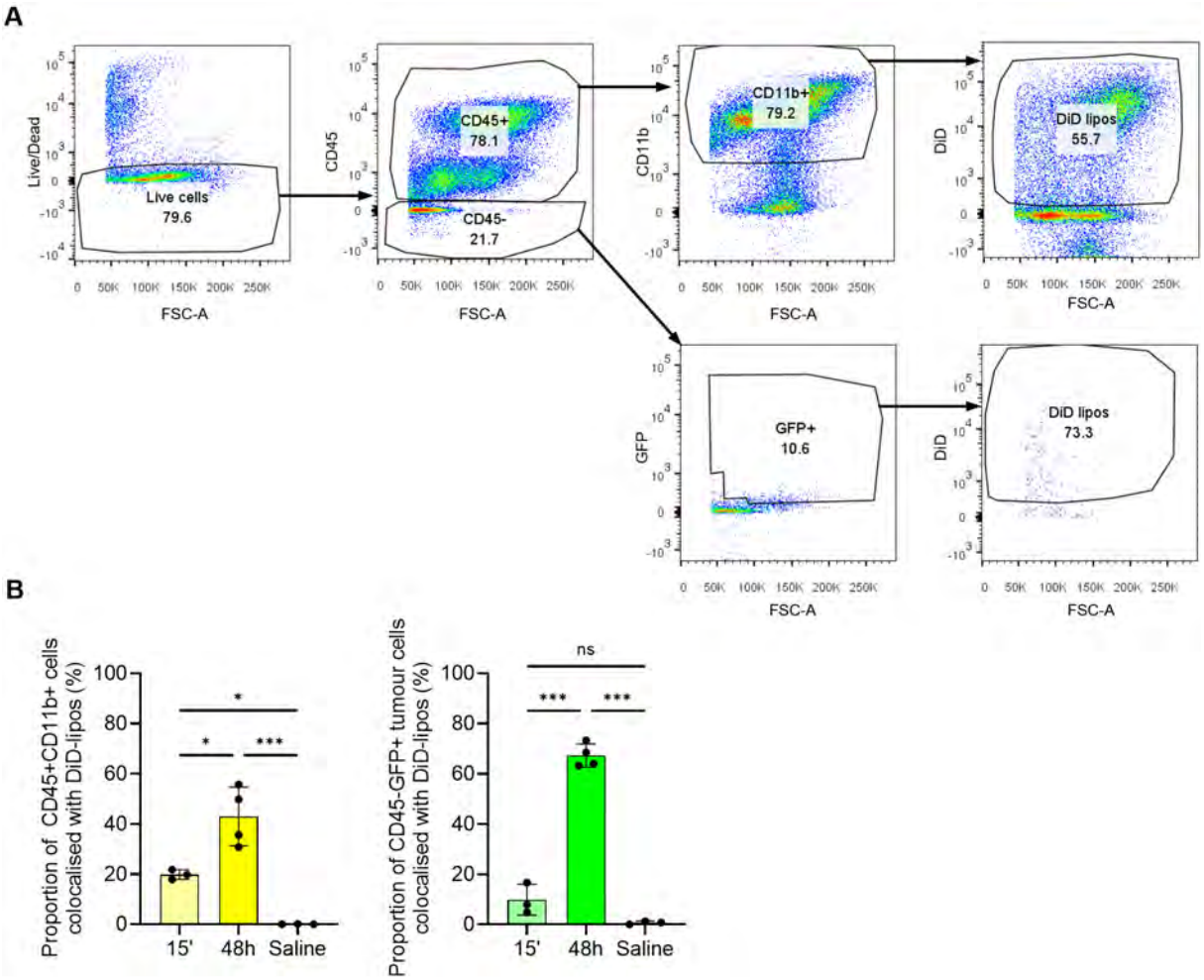


**Fig. S15. Flow cytometric analysis of liposome uptake efficiency within cells in the resection margin.** (**A**) Gating strategy for identification of distinct cell populations from live cells and identification of the DiD-positive fraction within each population. Analysis was performed on the surgically treated hemisphere of mice receiving intravenous DiD-labelled liposomes either 15 min or 48 h after resection surgery. Brains were isolated and analysed 24 h after injection. (**B**) Percentage of DiD-positive macrophages/microglia ($CD45^+CD11b^+$ cells within the total $CD45^+CD11b^+$ live cell population). Data are presented as mean ± SD. *P* values were determined using one-way ANOVA followed by Tukey's multiple comparison test (*$p < 0.05$, ***$p < 0.001$). (**C**) Percentage of DiD-positive tumour cells ($CD45^-GFP^+$ cells within the total $CD45^-GFP^+$ live cell population). Data are presented as mean ± SD. *P* values were determined using one-way ANOVA followed by Tukey's multiple comparison test (***$p < 0.001$; *ns*, not significant).

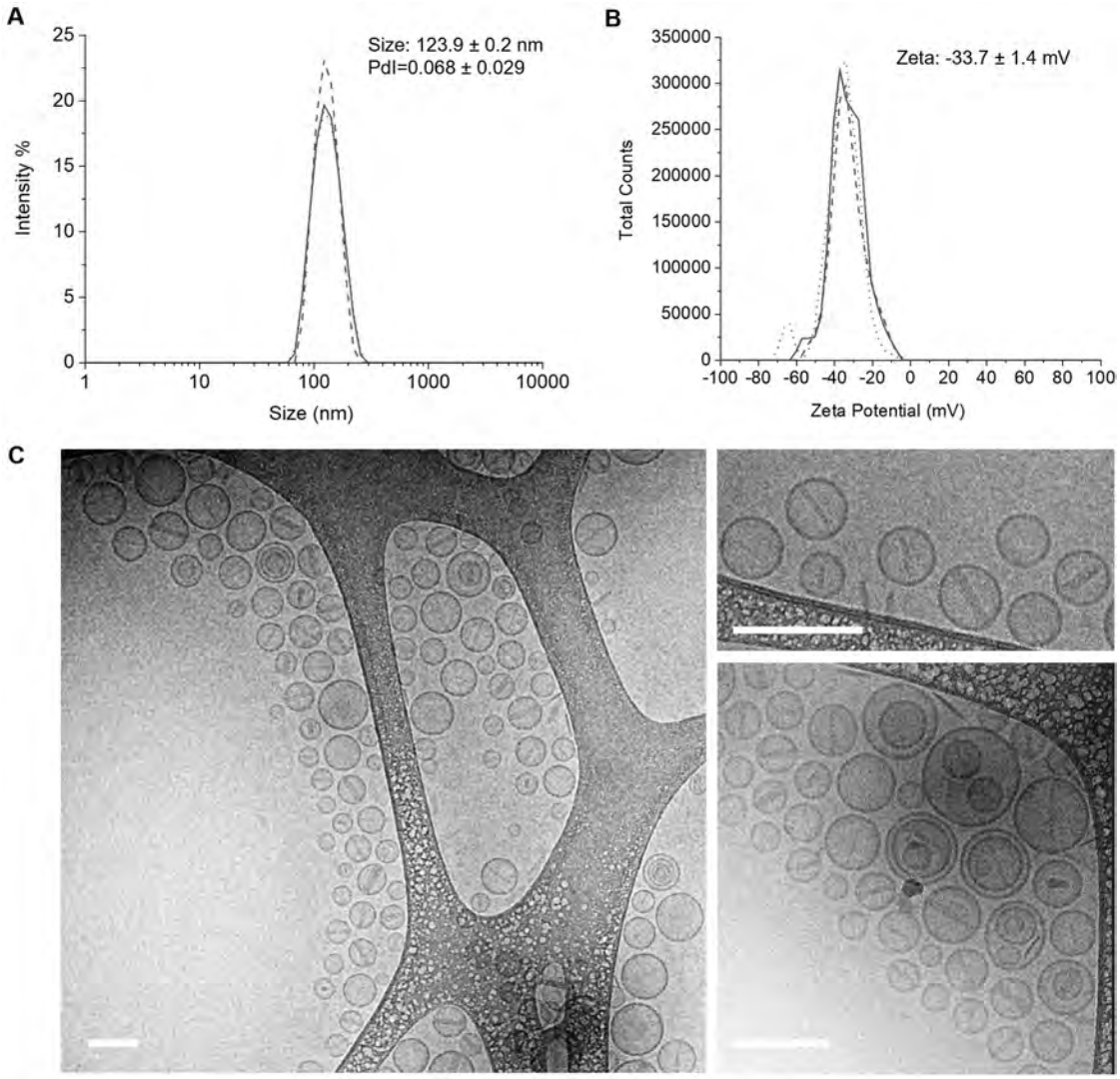


**Fig. S16. Doxorubicin-containing liposome (DOX-Lipo) characterization**. (**A**) Dynamic light scattering (DLS) analysis of liposome size distribution and (**B**) electrophoretic light scattering (ELS) measurements of zeta potential for doxorubicin loaded liposomes composed of HSPC:Chol:DSPE-PEG2000. Data are presented as mean ± SD from three independent measurements. (**C**) Structural and morphological characterisation of doxorubicin-containing liposomes in their native (aqueous) state by cryo-electron microscopy (cryo-EM). Scale bar = 200 nm.

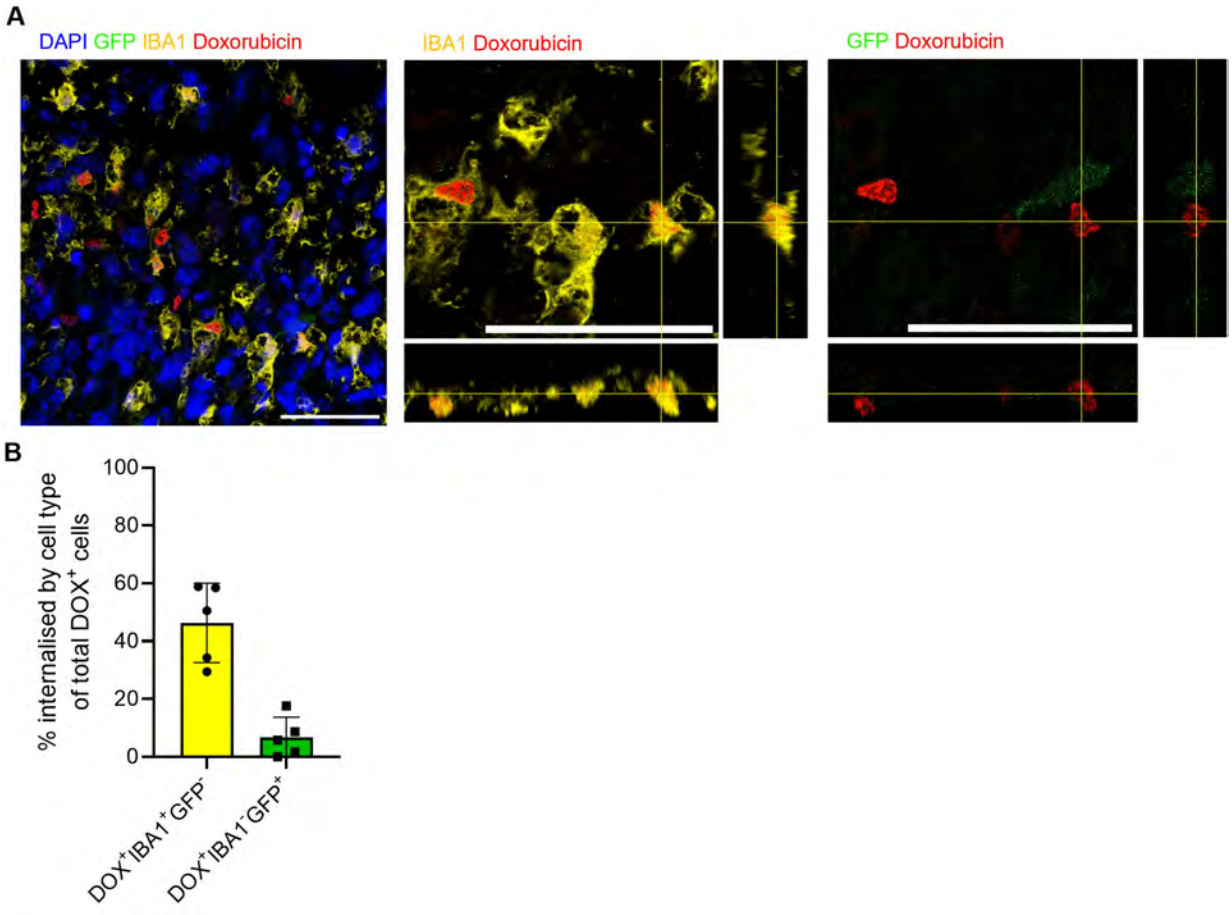


**Fig. S17. Preferential delivery of doxorubicin by DOX-liposomes into macrophages/microglia versus cancer cells in the resection margin.** (**A**) Representative confocal micrographs showing IBA1-positive macrophages/microglia, GFP-labelled tumour cells (mGNS; $NRAS^{G12V}$;shTP53-GFP;shATRX;luciferase), and doxorubicin in mice injected intravenously 48 h after mGNS tumour resection and analysed 24 h after injection. Scale bars = 50 μm. (**B**) Quantification of doxorubicin positive nuclei within IBA1-positive or GFP-positive cells, expressed as a percentage of total detected doxorubicin positive nuclei (three fields of view per mouse; n = 5 mice). Data are presented as mean ± SD.

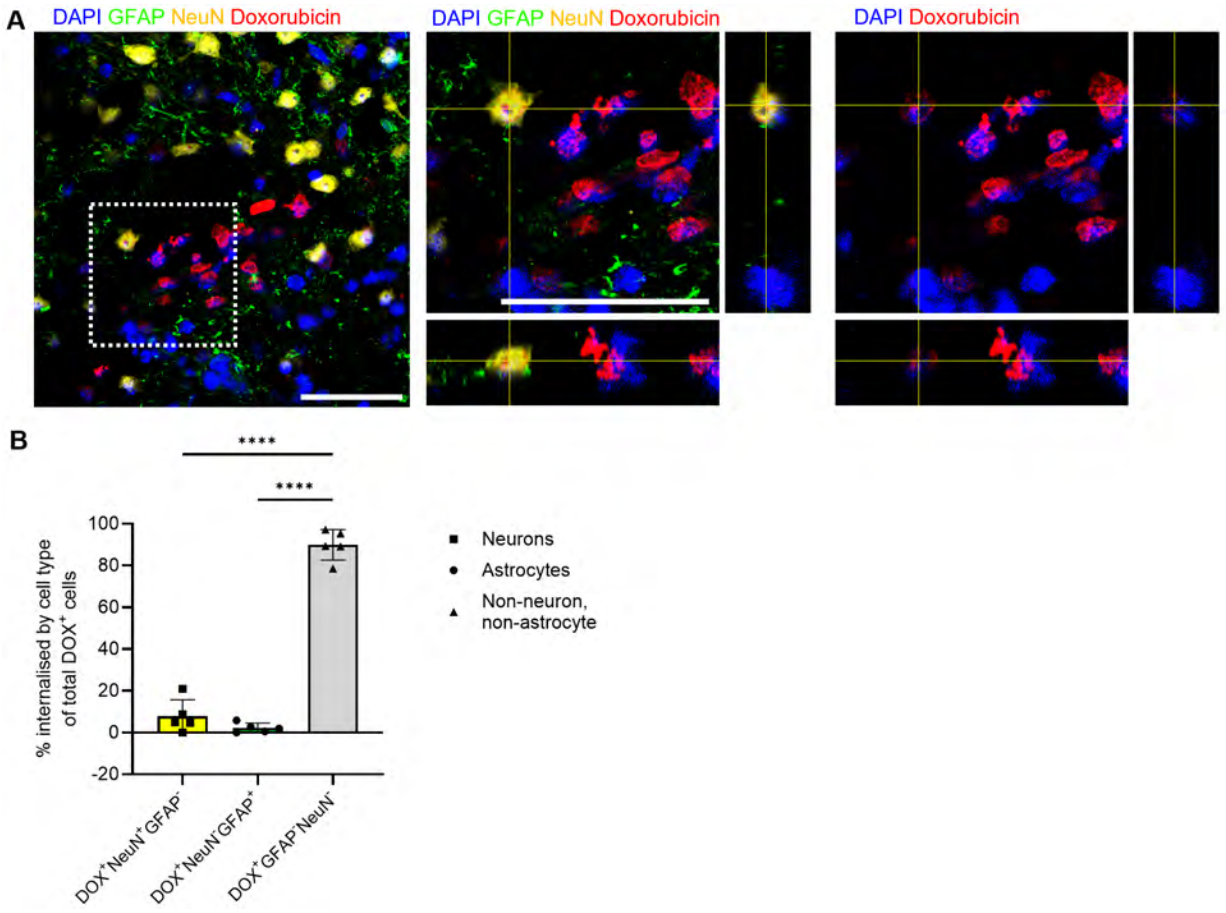


**Fig. S18. Minimal delivery of doxorubicin by DOX-liposomes into neurons or astrocytes at the resection margin.** (**A**) Representative confocal micrographs showing NeuN-positive neurons, GFAP-positive astrocytes, and doxorubicin in mice injected intravenously 48 h after mGNS tumour resection and analysed 24 h after injection. Scale bars = 50 µm. (**B**) Quantification of doxorubicin-positive nuclei within NeuN-positive or GFAP-positive cells, expressed as a percentage of total doxorubicin-positive nuclei (three fields of view per mouse; n = 5 mice). Data are presented as mean ± SD. *P* values determined by one-way ANOVA followed by Tukey's multiple comparison test. ****$p < 0.0001$.

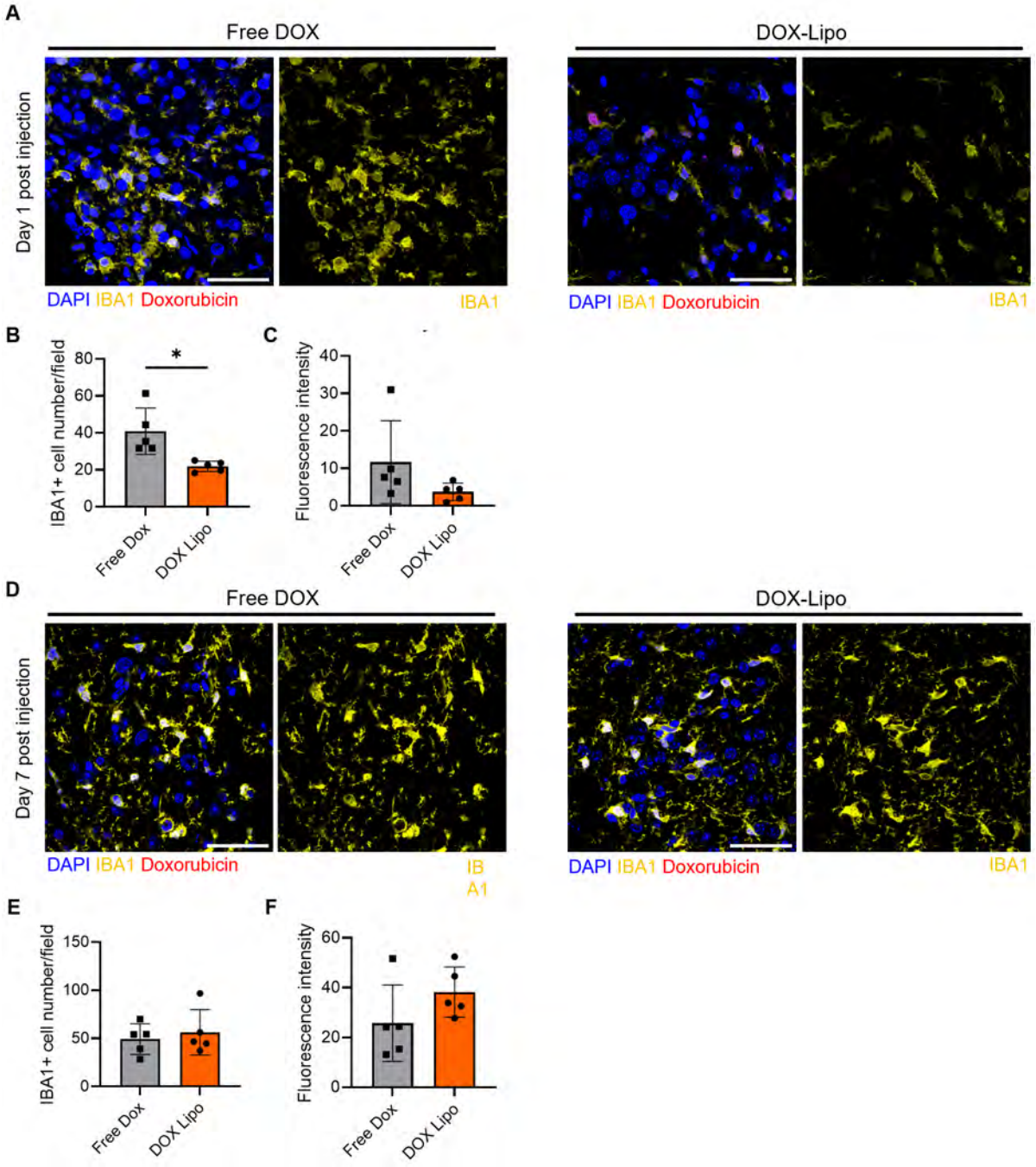


**Fig. S19. Effect of liposomal doxorubicin on macrophage/microglia populations at the resection margin.** Mice underwent resection of a GL261 tumour before receiving intravenous injection of DOX-Lipo (5 mg/kg doxorubicin) or free (non-liposomal) doxorubicin (5 mg/kg) 48 h after resection surgery. Brains were recovered either 24 h or 7 days after injection. (**A**) Representative confocal micrographs showing IBA1-positive macrophages/microglia 24 h after injection. Scale bars = 50 µm. (**B**) Quantification of the number of IBA1$^+$ cells per field of view (three fields of view per mouse; n = 5 mice). (**C**) Mean fluorescence intensity (mean gray value) of IBA1 signal per field (three fields of view per mouse; n = 5 mice). Data are presented as mean ± SD. *P* values were determined using Student's t-test (*$p < 0.05$). (**D**) Representative confocal micrographs showing IBA1-positive macrophages/microglia 7 days after injection. Scale bars = 50 µm. (**E**) Quantification of the number of IBA1$^+$ cells per field of view (three fields of view per mouse; n = 5 mice). (**F**) Mean fluorescence intensity (mean gray value) of IBA1 signal per field (three fields of view per mouse; n = 5 mice). Data are presented as mean ± SD. P values were determined using Student's t-test; no statistically significant differences were observed.

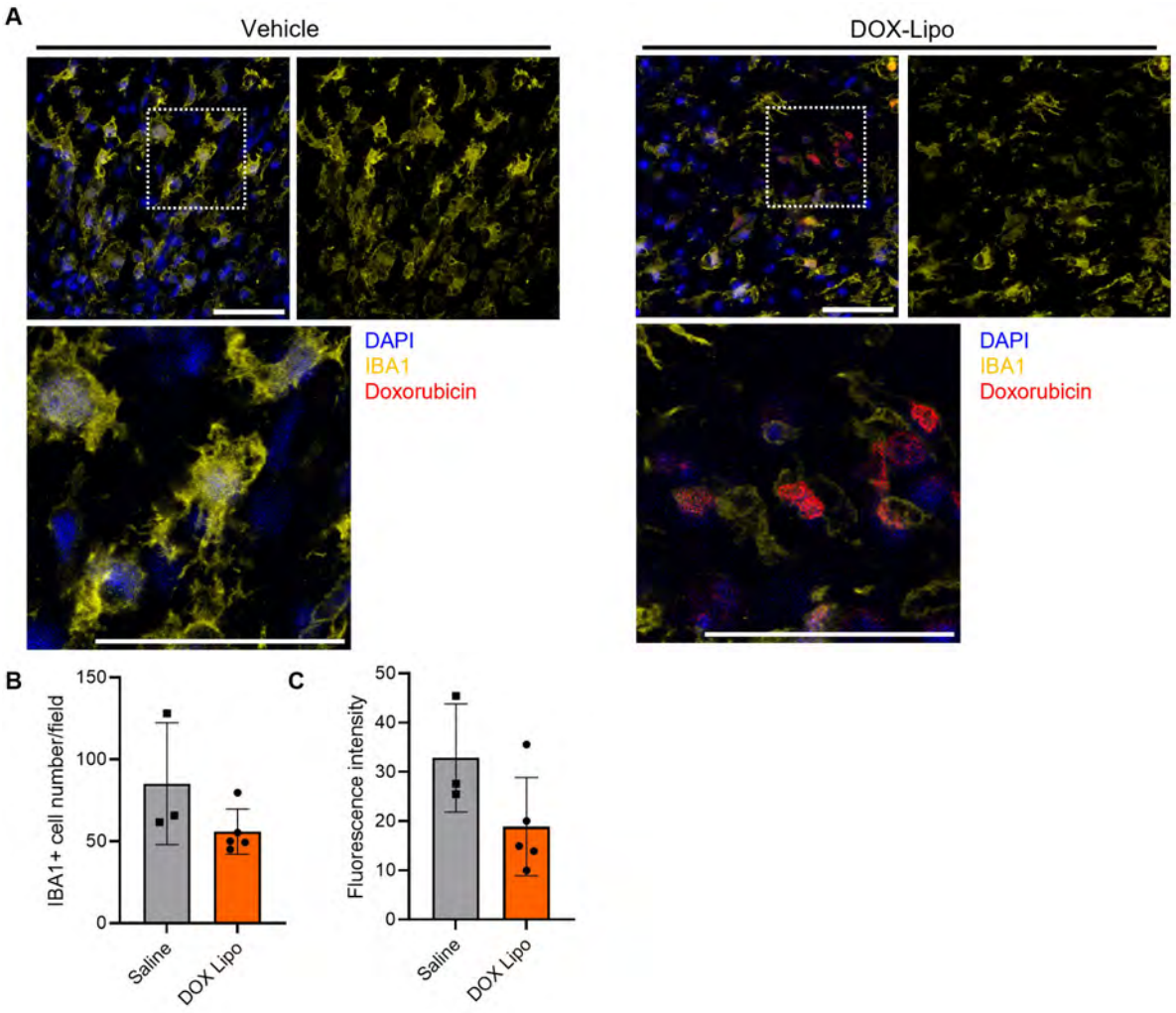


**Fig. S20. Effect of liposomal doxorubicin on macrophage/microglia populations at the resection margin in the more infiltrative mGNS model.** Mice underwent resection of a mGNS ($NRAS^{G12V}$;shTP53-GFP;shATRX;luciferase) tumour before receiving intravenous injection of DOX-Lipo (5 mg/kg doxorubicin) or saline vehicle control 48 h after resection surgery. Brains were recovered 24 h after injection. (**A**) Representative confocal micrographs showing IBA1-positive macrophages/microglia 24 h after injection. Scale bars = 50 µm. (**B**) Quantification of the number of $IBA1^+$ cells per field of view (three fields of view per mouse; n = 5 mice). (**C**) Mean fluorescence intensity (mean gray value) of IBA1 signal per field (three fields of view per mouse; n = 5 mice). Data are presented as mean ± SD. P values were determined using Student's t-test; no statistically significant differences were observed.

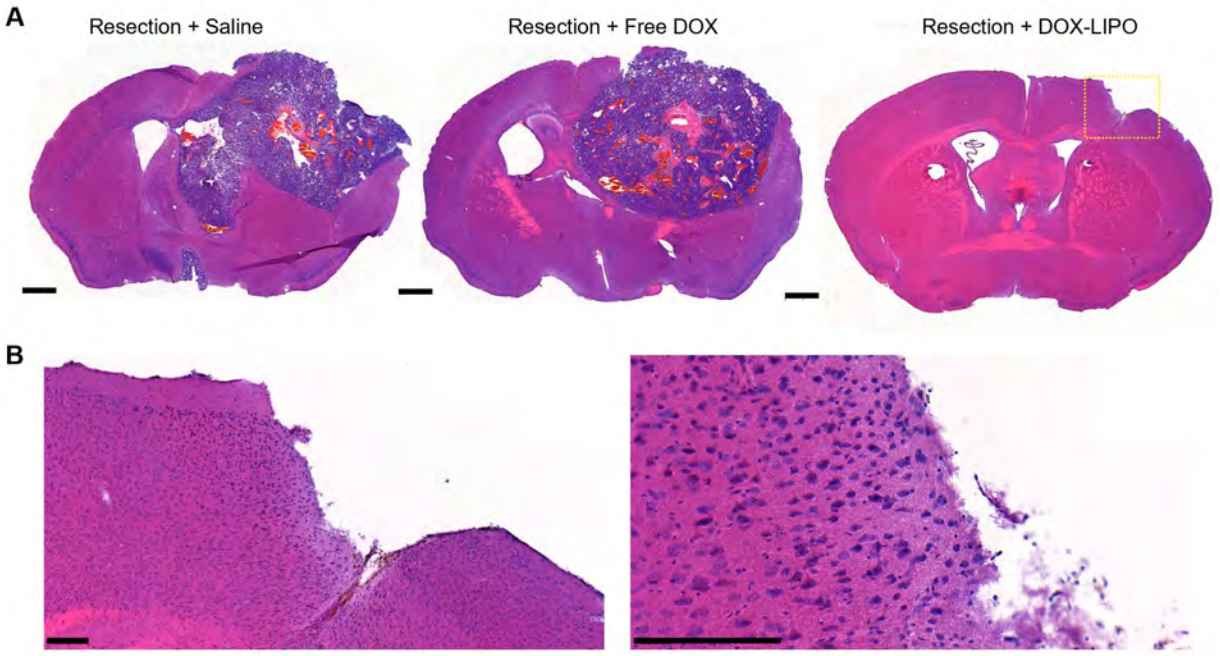


**Fig. S21. Histopathological assessment of tumour recurrence following postoperative doxorubicin treatment.** (**A**) Representative H&E-stained brain sections from GL261 tumour–bearing mice at study endpoint (humane survival endpoint) following surgical resection (day 7 post inoculation) and intravenous administration of DOX-Lipo (5 mg/kg doxorubicin), free doxorubicin (5 mg/kg), or vehicle control. Scale bar = 1 mm. (**B**) Representative higher-magnification H&E image of the resection margin from a DOX-Lipo–treated animal, showing no residual or recurrent tumour. Scale bar = 200 µm.

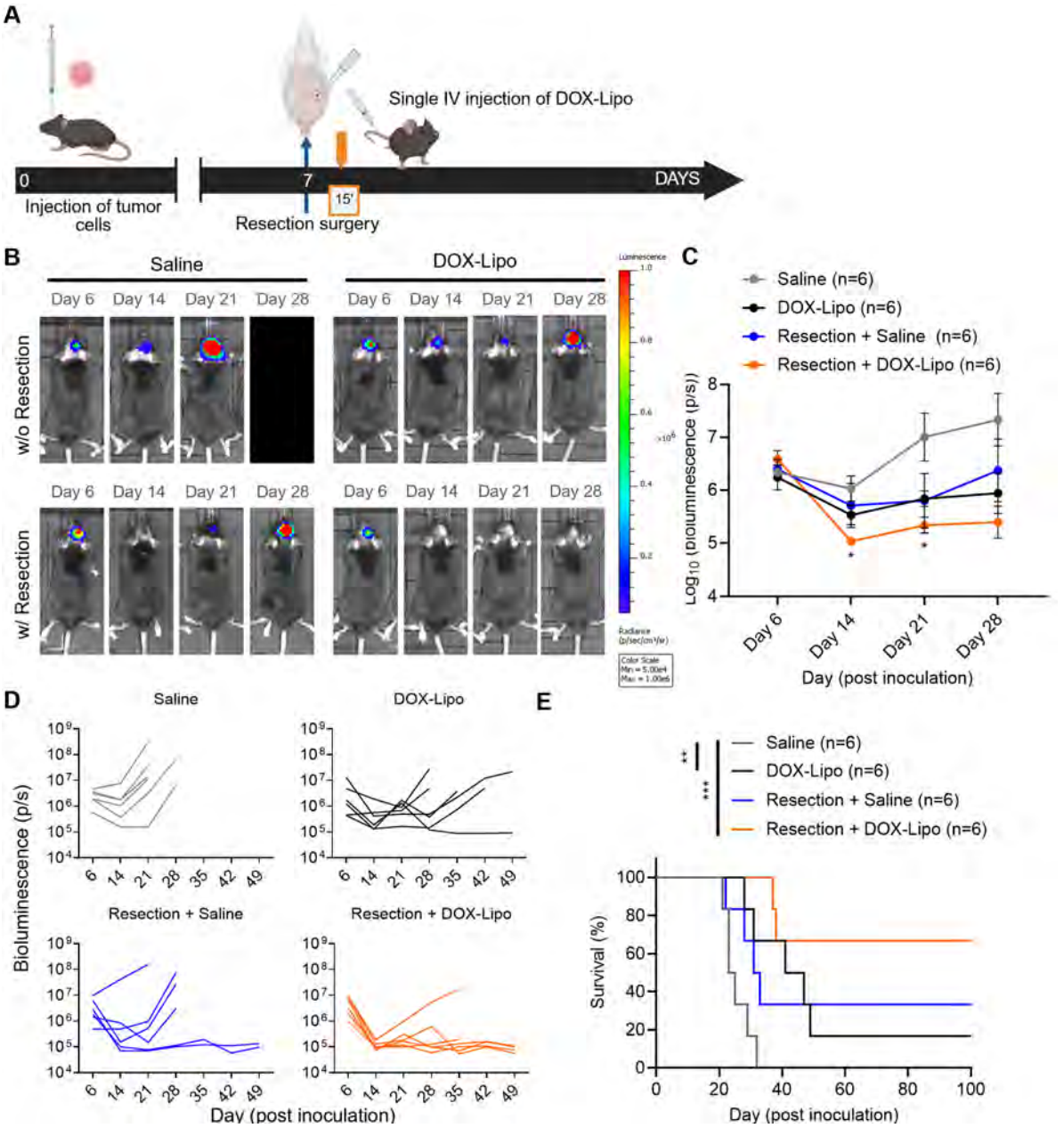


**Fig. S22. Liposomal doxorubicin administration immediately post-resection provides enhanced therapeutic efficacy.** (**A**) Experimental schematic. Following resection of established GL261 tumours, mice received intravenous administration of liposomal doxorubicin (DOX-Lipo) 15 min (15') after surgery**.** (**B**) Representative IVIS bioluminescence images acquired on days 6, 14, 21 and 28 post inoculation (corresponding to days −1, 7, 14 and 21 post resection). (**C**) Quantification of tumour bioluminescence (log10-transformed total flux, p/s) within each treatment group (n = 6). Data are presented as mean ± SEM. *P* values were obtained using two-way ANOVA followed by Tukey's multiple comparison test (**p* < 0.05 relative to saline control). **(D**) Quantification of tumour bioluminescence (total flux, p/s) for individual mice in each treatment group. (**E**) Kaplan–Meier survival curves for mice treated with DOX-Lipo or saline control, with or without glioma resection (n = 6). *P* values were determined using the log-rank (Mantel–Cox) test (***p* < 0.01, ****p* < 0.001).

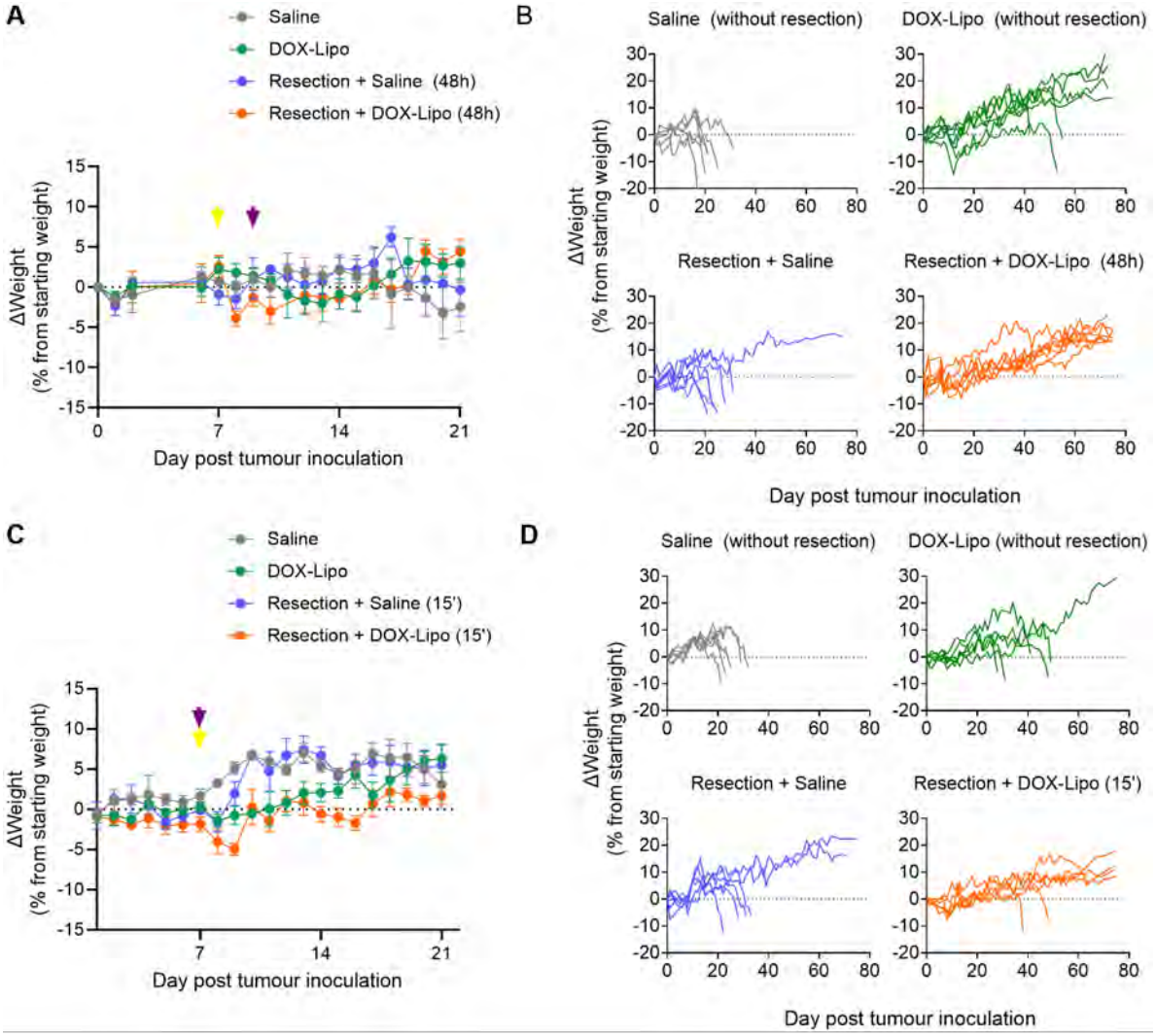


**Fig. S23. Animal health under early post-operative DOX-Lipo treatment.** (**A**) Change (Δ) in animal body weight expressed as a percentage of starting weight in mice treated intravenously with DOX-Lipo or vehicle 48 h after GL261 tumour resection surgery (or unresected control). Data are presented as mean ± SEM (n = 6–7) over the postoperative acute phase (21 days). Yellow and purple arrows indicate the time of resection surgery and DOX-Lipo administration, respectively. (**B**) Individual body weight trajectories for mice shown in (A), plotted up to day 80 post inoculation (n = 6–7). (**C**) Change (Δ) in animal body weight expressed as a percentage of starting weight in mice treated intravenously with DOX-Lipo or vehicle 15 min (15') after GL261 tumour resection surgery (or unresected control). Data are presented as mean ± SEM (n = 6) over the postoperative acute phase (21 days). Yellow and purple arrows indicate the time of resection surgery and DOX-Lipo administration, respectively. (**D**) Individual body weight trajectories for mice shown in (C), plotted up to day 80 post inoculation (n = 6).

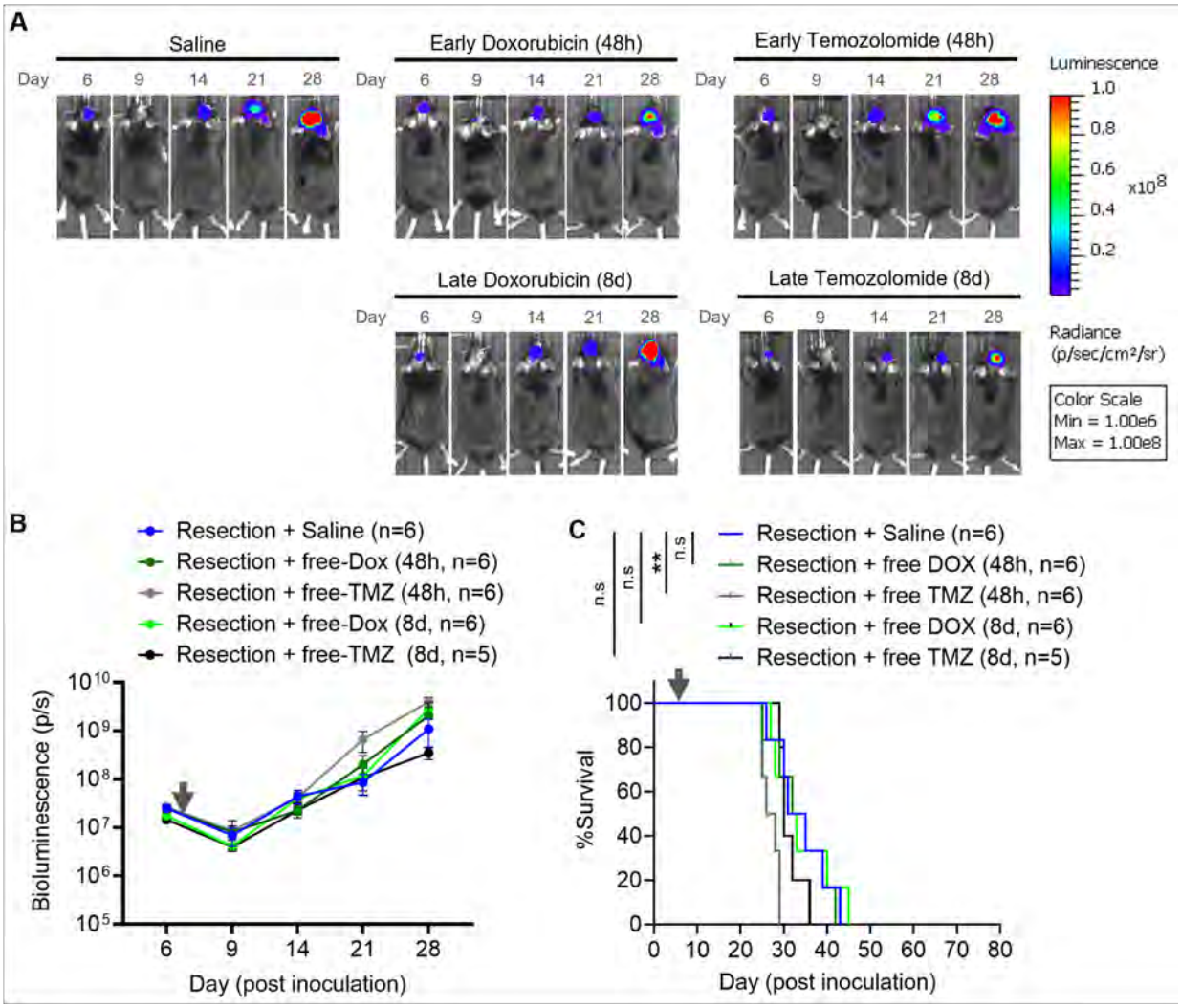


**Fig. S24. Liposome mediated drug delivery is critical for therapeutic efficacy in the postoperative window in the highly infiltrative mGNS model.** Following resection of mGNS (*NRAS$^{G12V}$;shTP53-GFP;shATRX;luciferase*) tumours, mice received intravenous administration of free (non-liposomal) doxorubicin (free-Dox; 5 mg/kg) or free (non-liposomal) temozolomide (free-TMZ; 25 mg/kg) either 48 h (early) or 8 days (delayed) after surgery. (**A**) Representative IVIS bioluminescence images acquired on days 6, 9, 14, 21 and 28 post inoculation (corresponding to days −1, 2, 7, 14 and 21 post resection). (**B**) Quantification of tumour bioluminescence (total flux, photons/s) within each treatment group (n = 5–6). Data are presented as mean ± SEM. Grey arrows denote day of surgical resection. (**C**) Kaplan–Meier survival curves for animals treated with early or delayed chemotherapy or saline vehicle control (n = 5–6). Grey arrows denote day of surgical resection. *P* values were determined using the log-rank (Mantel–Cox) test (**$p < 0.01$; *ns*, not significant).

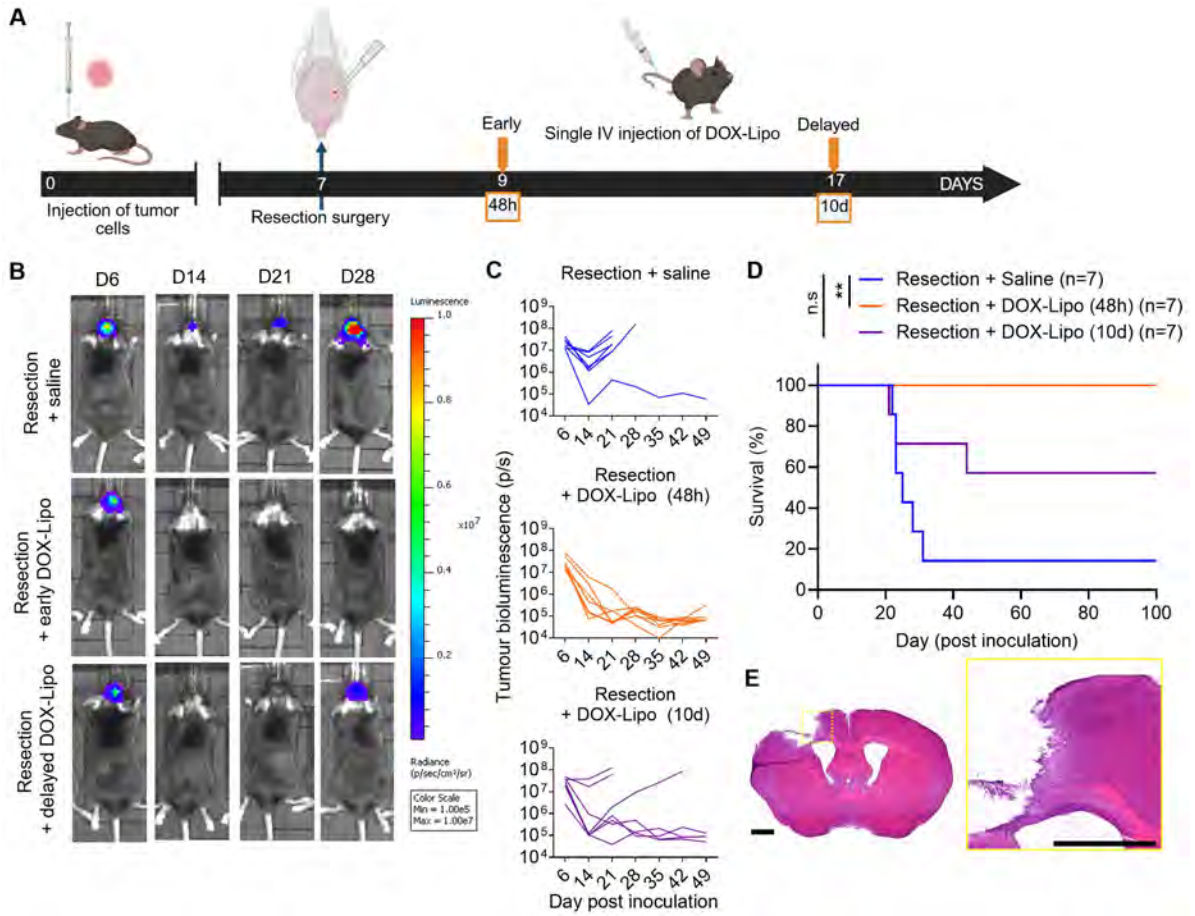


**Fig. S25. Early administration of liposomal doxorubicin within the window of BBB permeability is critical for therapeutic outcome.** (**A**) Experimental schematic. Following GL261 tumour resection, mice received intravenous administration of liposomal doxorubicin (DOX-Lipo) either 48 h (early) or 10 days (delayed) after surgery. (**B**) Representative IVIS bioluminescence images acquired on days 6, 14, 21 and 28 post inoculation (corresponding to days −1, 7, 14 and 21 post resection). (**C**) Quantification of tumour bioluminescence (total flux, p/s) for individual mice in each treatment group (n = 7). (**D**) Kaplan–Meier survival curves for animals treated with early or delayed DOX-Lipo or saline vehicle control (n = 7). *P* values were determined using the log-rank (Mantel–Cox) test (***p* < 0.01; *ns*, not significant). (**E**) Representative H&E-stained brain section from a surviving mouse at study endpoint (day 100; 93 days post resection), showing absence of tumour at the resection site (n = 7). Scale bars = 1000 µm.